Robust bandgaps for vibration control in periodic structures

Leandro Rodrigues Cunha

SPIM

Thèse de Doctorat

PÓS-GRADUAÇÃO
ENGENHARIA MECÂNICA | UFU

CONCEITO CAPES 2017-2020

UFC

école doctorale **sciences pour l'ingénieur et microtechniques**

UNIVERSITÉ DE FRANCHE-COMTÉ

In co-tutelle agrements for a double doctoral degree with

Federal University of Uberlandia (UFU)
School of Mechanical Engineering (FEMEC)

Robust bandgaps for vibration control in periodic structures

Leandro Rodrigues Cunha

CAPES

2017

CNPq
Conselho Nacional de Desenvolvimento Científico e Tecnológico

SPIM

Thèse de Doctorat

école doctorale **sciences pour l'ingénieur et microtechniques**

UNIVERSITÉ DE FRANCHE-COMTÉ

En accord de cotutelle pour obtenir double grade de docteur avec

L'Université Fédérale d'Uberlandia (UFU)
Faculté d'Ingénierie Mécanique (FEMEC)

NNT : 2017UBFCD060

Thèse présentée à

LA FACULTÉ D'INGÉNIERIE MÉCANIQUE (FEMEC)
DE L'UNIVERSITÉ FÉDÉRALE D'UBERLANDIA

par

Leandro Rodrigues Cunha

Pour obtenir le GRADE DE DOCTEUR

DE L'UNIVERSITÉ DE FRANCHE-COMTÉ
et
DE L'UNIVERSITÉ FÉDÉRALE D'UBERLANDIA

Specialité Mécanique

Thèse en cotutelle : Université de Franche-Comté – Université Fédérale d'Uberlandia

Bandgaps robustes pour contrôle de vibration dans les structures périodiques

Soutenue le 11 decembre 2017 devant le jury composé de:

Rapporteus:	J.R.F. Arruda	Professeur, UNICAMP (Campinas), Brésil
	M. Collet	Directeur de Recherche, LTDS, ECL, (Lyon), France
Examinateurs:	A. A. Cavalini Jr	Professeur, UFU (Uberlândia), Brésil
	J.-F. Deü	Professeur, LMSSC, CNAM (Paris), France
Directeurs:	D. A. Rade	Professeur, ITA (São José dos Campos), Brésil
	M. Ouisse	Professeur, FEMTO-ST, UBFC (Besançon), France

This page intentionally left blank

SPIM

Thèse de Doctorat

école doctorale **sciences pour l'ingénieur et microtechniques**

UNIVERSITÉ DE FRANCHE-COMTÉ

En accord de cotutelle pour obtenir double grade de docteur avec

L'Université Fédérale d'Uberlandia (UFU)
Faculté d'Ingénierie Mécanique (FEMEC)

NNT :
AAAAUBFCYXXX
(numéro à préciser lors du second dépôt)

Thèse présentée à

LA FACULTÉ D'INGÉNIERIE MÉCANIQUE (FEMEC)
DE L'UNIVERSITÉ FÉDÉRALE D'UBERLANDIA

par

Leandro Rodrigues Cunha

Pour obtenir le GRADE DE DOCTEUR

DE L'UNIVERSITÉ DE FRANCHE-COMTÉ
et
DE L'UNIVERSITÉ FÉDÉRALE D'UBERLANDIA

Specialité Mécanique

Thèse en cotutelle : Université de Franche-Comté – Université Fédérale d'Uberlandia

ROBUST BANDGAPS FOR VIBRATION CONTROL IN PERIODIC STRUCTURES

Soutenue le 11 decembre 2017 devant le jury composé de:

Rapporteus:	J.R.F. Arruda	Professeur, UNICAMP (Campinas), Brésil
	M. Collet	Directeur de Recherche, LTDS, ECL, (Lyon), France
Examinateurs:	A. A. Cavalini Jr	Professeur, UFU (Uberlândia), Brésil
	J.-F. Deü	Professeur, LMSSC, CNAM (Paris), France
Directeurs:	D. A. Rade	Professeur, ITA (São José dos Campos), Brésil
	M. Ouisse	Professeur, FEMTO-ST, UBFC (Besançon), France

This page intentionally left blank

To my beloved Parents, Brother and Sweetheart

This page intentionally left blank

Acknowledgements

Firstly, I would like to thank my Brazilian thesis advisor Dr. Domingos Alves Rade for proposing this enthralling subject and the unique opportunity to be advised in France by Dr. Morvan Ouisse from whom I learned so much. I would like to show my deep gratitude to both for accepting advise me and for being so patient during this cotutelle.

To the committee members of this jury for accepting be members Dr. Manuel Collet, Dr. José Roberto de França Arruda, Dr. Jean-François Deü and Dr. Aldemir A. Cavalini Jr.

To my laboratory collegues in Brazil Karina, Marcus Vinícius, Thiago, Polliana, Lucas, Edson, Marco Túlio, Leonardo, Arinan, Thales, Virgilio, Andressa, José Reis, Sigeo, Roney, Luiz Fernando, Adriano, Ulisses, Lorrane, Núbia, Diogo, …

To my laboratoty PhD collegues in France, Kévin Billon, Romeo, Emile, Huang (Nico), Maxime, Julien, Kendra, Cassidy, Ayrat, Paul Lépine, Olivier, Alexandre, Ludovic, Fabien, Gaël, Dyala, Frank, Paul Tourneroche, Titouan, Ahmed, Dario, Marc-Antoine, Remy, Dimitri, Mohamed, Justine, Saber, Romain, Alessandra, Pauline, Tomas, Kevin Jaboviste, …

To laboratory Workers and Professors who I had more contact and were always kind and helpful to me Luciene, Delphine, Nouredine, Fred Trivadey, Emiline, Gaël, Emmanuel, Sylvaine, Eric, Vincent, Xavier, Najib, …

To my long time friends Luís, Giordano, Lucas, Michel, Arthur, André, Tiago, …

To both universities, Federal University of Uberlandia and University of Bourgogne Franche-Comté, and their corresponding laboratories, LMEst and FEMTO-st with the Applied Mechanics Departement, for the opportunity.

And, finally, to CAPES and to CNPq for the scholarships.

Uberlandia, 11 December 2017.

This page intentionally left blank

CUNHA, L.R. Robust bandgaps for vibration control in periodic structures. 2017. 134 p. PhD Thesis, Federal University of Uberlandia, Uberlandia, Brazil and University of Bourgogne Franche-Comté, Besançon, France.

Abstract

In this thesis, a simple methodology to find robust bandgaps is presented. Four different periodic structures are used as numerical examples for infinite and finite models. The first two are related to attenuation zones created for longitudinal waves using spring-mass and stepped rod unit cells. The Transfer Matrix method is used to model the unit cell. With this method, it is possible to obtain the frequency responses, using a spectral method, and dispersion constants, solving an eigenvalue problem. The most influential physical and geometrical parameters are determined by performing partial derivative and finite difference sensitivity analysis through an infinite model. Therein, for the second example, the cross-section area of half-cell is considered as a stochastic variable represented by a probability density function with specific deviation properties for a probabilistic analysis. The third example concerns the bandgaps for flexural waves using stepped beams unit cells. For this case, the classical Transfer Matrix method cannot be used to obtain finite structures response in low frequency because of the presence of ill-conditioned matrices. Therefore, a recursive method termed Translation Matrix, which avoid matrix multiplication, is used and the corresponding probabilistic analysis is performed using the half-cell thickness as a random variable. An experimental analysis is also performed for this case, but considering half-cell length as uncertain. The last example is a periodic truss that is considered with and without smart components. The unit cell of this lattice structure can present passive and active members. As long as the type of unit cell is more complex, the finite element method is used. However, this kind of structure does not have impedance mismatches strong enough to open bandgaps although the presence of repetitive substructures. In virtue of this, eight scenarios are investigated considering the introduction of concentrated mass on joints and piezoelectric actuators in resonant shunt circuit which are considered as stochastic for specific cases. For each structure model, a Monte Carlo Simulation with Latin Hypercube sampling is carried out, the distinctions between the corresponding uncertain attenuation zones for finite and infinite models are exposed and the relation with localized modes is clarified. These results lead to conclude that the finite models present a larger stop zone considering stochastic parameters than infinite models. In other words, the uncertainties between neighbors' cells compensate each other and the finite structures is naturally more robust. Finally, the effect of increasing the uncertainty level, by varying a stochastic coefficient, is analyzed and the concept of robust band gap is presented.

Keywords

Periodic Structures, Vibration Control, Probabilistic Analysis, Uncertainty Propagation, Localization Phenomena, Wave Propagation

This page intentionally left blank

CUNHA, L.R. Bandgaps robustes pour controle de vibration dans les structures périodiques. 2017. 134 p. Thése de Doctorat, Université Fédéral d'Uberlandia, Uberlandia, Brésil et Université de Bourgogne Franche-Comté, Besançon, France.

Résumé

Dans cette thèse, une méthodologie simple pour trouver des bandes interdites robustes est présentée. Quatre structures différentes sont utilisées comme exemples numériques pour des modèles infinis et finis. Les deux premières possèdent des zones d'atténuation créées pour les ondes longitudinales en utilisant des cellules unitaires de masses/ressorts et de barres. La méthode des Matrices de Transfert est utilisée pour modéliser la cellule unitaire. Avec cette méthode, il est possible d'obtenir les réponses en fréquence, en utilisant une méthode spectrale, et les constantes de dispersion, en résolvant un problème aux valeurs propres. Les paramètres physiques et géométriques les plus influents sont déterminés en effectuant une analyse de sensibilité aux dérivées partielles et aux différences finies à travers un modèle infini. Dans ce cas, pour le deuxième exemple, la section de la demi-cellule est considérée comme une variable stochastique, représentée par une fonction densité de probabilité pour une analyse probabiliste. Le troisième exemple concerne les bandes interdites pour les ondes de flexion utilisant des cellules unitaires de poutres. Dans ce cas, la méthode classique des Matrices de Transfert ne peut pas être utilisée pour obtenir une réponse de structure finie en basses fréquences en raison de la présence de matrices mal conditionnées. Par conséquent, une méthode récursive est utilisée. Une analyse expérimentale est également réalisée pour ce cas, mais considérant la longueur de la moitié des cellules unitaire comme incertaine. Le dernier exemple est un treillis périodique considéré avec et sans dispositifs intelligents. La cellule unitaire de cette structure en treillis peut présenter des éléments passifs et actifs. En raison de la complexité de ce type de cellule, la méthode des éléments finis est utilisée. Cependant, ce type de structure ne présente pas de ruptures d'impédance suffisamment fortes pour ouvrir des bandes interdites même en présence de sous-structures répétitives. En vertu de cela, huit scénarios sont étudiés en considérant l'introduction de masses concentrées dans les articulations, et les actionneurs piézoélectriques dans les circuits shunt résonants qui sont considérés comme stochastiques pour des cas spécifiques. Pour chaque modèle de structure, une simulation de Monte Carlo avec Latin Hypercube est effectuée, les distinctions entre les zones d'atténuation incertaines correspondantes pour les modèles finis et infinis sont exposées et la relation avec les modes localisés est clarifiée. Ces résultats suggèrent que les modèles finis ont une bande interdite plus large que les modèles infinis en considérant les incertitudes. En d'autres termes, les incertitudes entre les cellules voisines se compensent et les structures finies sont naturellement plus robustes. Enfin, l'effet de l'augmentation du niveau d'incertitude, en faisant varier un coefficient stochastique, est analysé et le concept de bande interdite robuste est présenté.

Mots-clés

Structures Périodiques, Contrôle de vibration, Analyse Probabiliste, Propagation d'incertitudes, Phénomène de localization, Propagation des ondes

This page intentionally left blank

CUNHA, L.R. Bandas de atenuação robustas para controle de vibração em estruturas periódicas. 2017. 134 p. Tese de Doutorado, Universidade Federal de Uberlândia, Uberlândia, Brasil e Universidade de Bourgogne Franche-Comté, Besançon, França.

Resumo

Nesta tese, uma metodologia simples para encontrar bandas de atenuação robustas é apresentada. Quatro estruturas periódicas diferentes são usadas como exemplos numéricos para modelos infinitos e finitos. As duas primeiras estão relacionadas à zonas de atenuação criadas para ondas longitudinais utilizando sistemas massa-mola e barras como células unitátias. O método da Matrix de Transferência é usado para modelar a célula unitária. Com este método, é possível obter respostas em freqüência, usando um método espectral, e constantes de dispersão, resolvendo um problema de autovalor. Os parâmetros físicos e geométricos mais influentes são determinados pela realização de análises des sensibilidade através de derivadas parciais e diferenças finitas usando um modelo infinito. Para o segundo exemplo, a área de seção transversal de meia célula é considerada como uma variável estocástica representada por uma função densidade de probabilidade com propriedades de desvios específicas para uma análise probabilística. O terceiro exemplo diz respeito às bandas proibidas para ondas de flexão usando células unitárias compostas de vigas. Para este caso, o método clássico de Matriz de Transferência não pode ser usado para obter as respostas de estruturas finitas em baixa freqüência devido à presença de matrizes mal condicionadas. Portanto, um método recursivo denominado Matriz de Translação, que evita a multiplicação de matrizes, é usado e a análise probabilística correspondente é realizada usando a espessura de meia célula como variável aleatória. Uma análise experimental também é realizada para este caso, mas considerando o comprimento de meia célula como incerto. O último exemplo é uma treliça periódica considerada com e sem componentes inteligentes. A célula unitária desta estrutura pode apresentar membros passivos e ativos. Enquanto o tipo de célula unitária for mais complexo, o método de elementos finitos é usado. No entanto, esse tipo de estrutura não possui rupturas de impedância fortes o suficiente para abrir bandas de atenuação, embora haja a presença de subestruturas repetitivas. Em virtude disto, oito cenários são investigados considerando a introdução de massa concentrada em articulações e atuadores piezoelétricos em circuito shunt ressonante que são considerados estocásticos para casos específicos. Para cada modelo estrutural, uma Simulação de Monte Carlo com amostragem de Hypercube latino é realizada, as diferenças entre as zonas de atenuação incertas correspondentes aos modelos finitos e infinitos são expostas e a relação com modos localizados é esclarecida. Esses resultados levam a concluir que os modelos finitos possuem uma região de atenuação maior do as de modelos infinitos considerando parâmetros estocásticos. Em outras palavras, as incertezas entre células vizinhas se compensam e as estruturas finitas são naturalmente mais robustas. Finalmente, o efeito do aumento do nível de incerteza, variando um coeficiente estocástico, é analisado e o conceito de banda de atenuação robusta é apresentado.

Palavras-chave

Estruturas Periódicas, Controle de Vibração, Análise Probabilística, Propagação de Incertezas, Fenômenos de Localização, Propagação de ondas

This page intentionally left blank

Contents

Acknowledgements i

Abstract iii

Keywords iii

Résumé v

Mots-clés v

Resumo vii

Palavras-chave vii

List of Figures xiii

Chapter 1 Introduction 1

1.1 Context 1

1.2 Objectives 4

1.3 Literature Review 4

1.3.1 Metamaterials and Periodic Structures 7

1.3.2 Smart materials and structures 10

1.4 Research context 14

1.5 Organization of the thesis 16

Chapter 2 Longitudinal waves 17

2.1 Introduction 17

2.2 Longitudinal waves in rods 19

2.2.1 Discrete systems 19

2.2.2 Continuous systems 25

2.3 Parametric and Sensitivity Analysis 29

2.3.1 Spring-mass models 29

2.3.2 Continuous models 31

2.4 Uncertainty propagation using Monte Carlo Simulation 33

2.4.1 Uncertainty propagation for a two-segment continuous rod 34

2.4.2 Robust Bandgap and Localization phenomena 37

2.5 Partial conclusion 40

Chapter 3 Flexural waves 43

3.1 Introduction 43

3.2 Flexural waves in Euler-Bernoulli beams 45

3.2.1 Periodic models 46
3.3 Transfer Matrix method and stability problems 48
3.4 Numerical examples 54
3.4.1 Two continuous part beam parametric study 54
3.4.2 Probabilistic analysis and robust bandgap 56
3.4.3 Localization phenomena in stepped beam unit cell 59
3.4.3.1 Introduction of damping *60*
3.5 Partial conclusion 62
Chapter 4 Experimental analysis of flexural beams 63
4.1 Introduction 63
4.2 Modeling of stepped beam unit cell with six *dofs* 64
4.2.1 Translation Matrix with six *dofs* verification 66
4.3 Experimental bench and setup 67
4.4 Numerical and experimental results 68
4.4.1 Non localized modes inside the attenuation zone 70
4.4.1.1 Considering variation on excitation and measument parameters *71*
4.4.2 Robust bandgap and experimental FRFs 72
4.5 Partial conclusion 73
Chapter 5 Truss structures 75
5.1 Introduction 75
5.2 Methodology for truss structures 78
5.2.1 Discrete systems comparison 78
5.3 First structure: smart rod finite element truss 80
5.3.1 Smart cell: Constitutive equations of linear piezoelectricity 80
5.3.1.1 Smart unit cell with shunt circuit *80*
5.3.1.2 Tuning a resonant RLC circuit *82*
5.3.2 Frequency response function and dispersion diagrams 83
5.3.3 Monte Carlo Simulation and localization phenomena 85
5.3.4 Probabilistic Analysis 86
5.3.5 Numerical results 87
5.4 Second structure: beam finite element truss 91
5.4.1 Dispersion constants 93
5.5 Partial conclusion 94
Chapter 6 Conclusion and Perspectives 95

6.1 Conclusions 95
6.2 Contributions 97
6.3 Perspectives 99
6.4 List of publications and presentations 100
References **101**

This page intentionally left blank

List of Figures

Figure 1.1 Wave propagating in a string with two density mismatches, in normalized positions 0.333 and 0.666, and fixed-fixed boundary contitions. 5
Figure 1.2 Examples of periodic structures in nature: (a) bamboo, (b) honeycomb and (c) spider web. 7
Figure 1.3 Examples of Smart Materials: (a) Piezoelectric and (b) Shape memory polymers (reproduced from Butaud et al. (2016)). 10
Figure 1.4 Evolution from spring-mass systems, rods and beams to smart trusses. 14
Figure 1.5 Proposed solutions. 15
Figure 2.1 Example of spring-mass unit cell. 19
Figure 2.2 Dispersion diagrams for different unit cells: (a) case 1, (b) case 2 and (c) case 3, and FRF amplitudes computed for 1 and 10 cells: (d) case 1; (e) case 2; (f) case 3. 22
Figure 2.3 Dispersion diagrams for different unit cells: (a) case 4, (b) case 5, (c) case 6 and FRF amplitudes computed for 1 and 10 cells: (d) case 4; (e) case 5; (f) case 6. 23
Figure 2.4 Rod unit cell with two continuous dissimilar parts. 25
Figure 2.5 Dispersion diagram for a contrinuous rod and for a stepped rod. 27
Figure 2.6 Frequency response functions for a free-free periodic stepped rod finite structure with 10 cells, one cell and its exact natural frequencies for symmetric and antisymmetric modes. 27
Figure 2.7 Frequency response functions for finite strucutres with various cell number. 29
Figure 2.8 (a) Parametric variation of unit cell parameters on abscissa and frequency on ordinate for band gap envelopes ( ), natural frequency inside attenuation zone ( ), band gap borders 1 ( ), 2 ( ) and 3 ( ) and (b) their corresponding analytical derivatives for case 2. 30
Figure 2.9 (a) Parametric variation of unit cell parameters on abscissa and frequency on ordinate for band gap envelopes ( ), anti-resonance inside attenuation zone ( ) and natural frequency ( ); band gap borders 1 ( ), 2 ( ) and 3 ( ) and (b) their corresponding analytical derivatives for case 5. 31
Figure 2.10 (a) Bandgap envelopes, (b) bandgap borders and width; (c) their respective numerical derivatives. 32
Figure 2.11 Bandgap borders for: (a) finite model and (b) infinite model. 35
Figure 2.12 (a) Bandgap borders' and (b) width's mean and confidence intervals for infinite structure (IS) with 1 random variable (RV) and for finite structures (FS) with 1 and 10 random variables. 36
Figure 2.13 Robust bandgaps for rod example considering (a) finite structure and (b) infinite structure. 36
Figure 2.14 Comparison between (a) symmetrical and antisymmetrical structures, their (b) FRFs and (c) the shape of localized mode L1 for antisymmetrical one. 38
Figure 2.15 (a) 14 different structures cases and their corresponding FRFs for (b) cases 0, 1, 2, 3 and 4; (c) 0, 5, 6, 7 and 8; (d) 1, 9, 10 and 11; (e) 0, 12, 13 and 14; and (f) the shape of localized modes L2, L3 and L4. 38
Figure 3.1 Representation of two continuous parts unit cell for a periodic beam structure. 45
Figure 3.2 Dispersion constants considering flexural waves for (a) continuous beam and (b) stepped periodic beam. 48

Figure 3.3 FRF Transfer Matrix method stability problem for: (a) continuous beam and (b) stepped periodic beam. 49
Figure 3.4 FRF convergence of finite element mesh to Translation Matrix model for a periodic beam with 10 cells. 53
Figure 3.5 Comparison of Translation Matrix method FRF for a continuous beam composed of 10 continuous parts with analytical FRF. 53
Figure 3.6 (a) Asymmetric beam unit cell and (b) its finite structure with 10 cells. 54
Figure 3.7 FRFs of stepped beam for several values of beam (a) thickness h_2 and (b) width b_2. 55
Figure 3.8 FRFs of stepped beam for several values of (a) discontinuity location and (b) cell length l. 55
Figure 3.9 Number of cells for a stepped unit cell finite structure for an observable attenuation zone. 56
Figure 3.10 Bandgaps borders and width for (a) finite model and (b) infinite model. 57
Figure 3.11 Confidence intervals for (a) LB, UB and (b) W for infinite structure (IS) with a stepped beam unit cell and for a finite structure (FS) with 10 stepped beam unit cells. 58
Figure 3.12 Robust bandgap for a stepped beam example considering (a) finite and (b) infinite structure. 58
Figure 3.13 Symmetric unit cells (a) 1 and (b) 2 for flexural beams. 59
Figure 3.14 FRFs of a finite structure with one and ten cells for symmetric cell (a) 1 and (b) 2. 60
Figure 3.15 FRFs for convergence of cell number for: symmetric cases (a) and (b) and asymmetric case (c). 60
Figure 3.16 Periodic beam with 10 cells and localization phenomenon on cell 6 ($h_1 = h_2$). 61
Figure 3.17 FRF of a beam periodic structure with localization phenomena and damping on cell 6. 61
Figure 4.1 (a) Real and (b) imaginary parts of dispersion constants for continuous beam unit cell and (c) real and (d) imaginary parts for stepped beam unit cell. 65
Figure 4.2 FRF convergence of F.E. model for a periodic beam with 10 cells to Translation Matrix model with six *dofs*. 66
Figure 4.3 Experimental set up for a periodic free-free beam. 67
Figure 4.4 Frequency response function obtained experimentally for a free-free continuous beam. 69
Figure 4.5 Frequency response function obtained experimentally for a free-free periodic beam with 10 stepped unit cells. 69
Figure 4.6 FRF with non-predicted resonance frequencies inside the attenuation zone. 70
Figure 4.7 FRF with variation on exciting force angle and direction of measured displacement. 71
Figure 4.8 FRF with envelope confidence interval, experimental results and robust bandgap for calculated standard deviation. 72
Figure 5.1 (a) 3D truss unit cell and (b) its finite model. 78
Figure 5.2 (b) Attenuation and (c) phase constants of truss unit cell (a) without concentrated mass on nodes. 79
Figure 5.3 (b) Attenuation and (c) phase constants of truss unit cell (a) with concentrated mass on nodes. 79
Figure 5.4 (a) Smart unit cell and (b) its piezoelectric stack actuator described as a finite element model. 81
Figure 5.5 Considered unit cells (a), (b), (c), (d), (e), (f), (g) and (h) with their respective dispersion diagrams. 83
Figure 5.6 (a), (b) and (c) frequency responses of 8 scenarios periodic finite structures with 10 cells by exciting the firt node on direction x, y and z and observeing the corresponding dofs on the last unit cell. 84
Figure 5.7 (a) FRFs with localization phenomena L1, L2, L3 and L4 and (b) their corresponding mode shape. 86

Figure 5.8 Bandgap bounds envelopes relatives to scenarios on Figures 5.3(c), 5.3(f) and 5.3(h), with: (a) mass as RV, (b) and (c) inductance as RV considering an infinite model (1 RV) with their corresponding (d), (e) and (f) for finite results with 10 RV. 88
Figure 5.9 Robust band gaps for finite structures composed of 10 unit cells (a) and (c) and their respective dispersions diagramas for infinite structures (b) and (d). 89
Figure 5.10 Band gap for (a) finite and (b) infinite structures considering the local resonance effect. 90
Figure 5.11 Example of truss unit cell with concentrated mass in the middle of (a) vertical and (b) horizontal bars to reduce frequency of inner resonances. 91
Figure 5.12 (a) Truss unit cell modeled with Euler-Bernoulli beams with concentrated mass on yellow circles dofs and (b) corresponding finite structure. 91
Figure 5.13 Resonant beam with concentrated mass and its (a) first longitudinal mode, (b) first three flexural modes and (c) a zoom of (b) in low frequency. 92
Figure 5.14 Dispersion constants for unit cell (a) without concentrated mass and (b) with mass on position 5....93

This page intentionally left blank

Chapter 1 Introduction

1.1 Context

In this thesis, attention is devoted to periodic structures. These structural arrangements have some particularities such as the way they are modeled as infinite assemblies of identical cells. Nonetheless, the situation of perfectness is unachievable in reality and a lack of information can be noticed in the literature. Besides, these repetitive structures are an extremely exciting area of current research, which aims to improve the vibration attenuation in some frequency bands by creating or exploring periodicity already present in some kind of structures. Many examples can be mentioned like bridges, towers, antennas, satellites, space stations and shuttles, aircraft structures, among others.

These structures can operate as “mechanical filters” achieving high levels of attenuation and overcoming the limitations of traditional active, passive and semi-passive vibration controls. Beyond that, they are interesting because of their specific strength. They do not add considerable weight, being able even to reduce this characteristic, and they can resist important solicitations providing an extremely lightweight, resistant and compact solution. Concisely, this is a way to optimally guide energy inside the structure. However, the efficiency of the vibration reduction is limited in terms of frequency bandwidth, hence deep understanding of underlying physics and efficient modelling tools are required for the design of periodic structures.

Concerning vibration control, an important aspect is the spectrum location of resonance frequencies. Some other interesting aspects that designers usually do not take into account are the positions of anti-resonances. With periodic structures, for example, the superposition of dynamic vibration absorbers anti-resonances can create large frequency bands of intense attenuation.

Another concept that has been largely investigated over the last years is smart structures. This concept, allied to some specific materials that can exchange energy from different physical domains, defines the capacity of self-adapting to overcome unpredicted situations. These structures are composed by materials that can sense and actuate simultaneously. This ability transforms this kind of material in an interesting solution as it can be tuned to work in a specific mode. Moreover, this structure can have its health monitored continuously due to the presence of sensors.

Periodic and Smart Structures are promising concepts for the future of engineering. They can be complementary to each other and this allows exploring further the limits of each of them. Before prospecting these improvements, it is important to create a trustworthy model to represent their behaviors. Then, it is necessary to exhaustively simulate, execute parametric studies and validate experimentally. Nevertheless,

these analytical or numerical models are most of the time deterministic and they are not able to represent every structure behavior. For example, a model for longitudinal waves in a rod does not to consider transverse displacement. However, in reality, the excitation force can be able to excite motion in more than one direction.

One limitation of simulating periodic structures is the high computational cost. Normally, it is possible to represent a phenomenon by knowing its fundamentals and assuming some hypotheses. Firstly, an analytical solution may be searched. A numerical solution is always a second option because it is more expensive and less accurate than analytical solutions. For example, a finite element model with a fine mesh can be highly expensive. Despite of that, if an analytical model cannot be used, model reduction techniques can be employed in numerical models to reduce computation time. Moreover, during the resolution, numerical issues can appear increasing errors in results. For example, an ill-conditioned matrix can produce erroneous results by creating divergent data while using transfer matrix methods. It occurs due to the presence of insignificant errors in previous steps due to matrix inversion that cumulate during the multiplication process. These matrices problems can appear even in semi-analytical models and they are present in the majority of numerical models.

Therefore, the choice of suitable methods can increase the efficiency and reduce the computational cost. In addition, for some complex structures and situations, there is an obligation to employ some specific software. Automatic scripts are mandatory in engineering nowadays to simulate and design optimized structures considering the best performance without weakening, approaching to a failure situation, or reducing the robustness of them.

With the progress of technology, brute force methods are becoming interesting to execute using parallel computing. Computers with multiple cores can split repeated and independent tasks and the Monte Carlo Simulation and some optimization algorithms can be used. Some problems can be found when each core needs a software license to launch a batch simulation. In this case, some dependency to software can become a problem. They are easy to use but the designer can be blocked in some circumstances. For example, in some cases of parallel computing, each core needs a software license or a special one to run scripts in parallel and, consequently, gain time. In this case, the ubiquity of Matlab® and programing languages, as C or C++, can be interesting in these situations and homemade scripts are considerably appreciated. For example, a Matlab® loop for parallel computing can be easily implemented using a homemade function with no dependency of another software.

Uncertainty is a terminology used to describe situations involving unknown information or imperfection.

In engineering, all kinds of manufactured structures are not perfect, have no exact dimension and this desired exactitude is not possible to be obtained, even if some tolerances are acceptable. They can present no observable defects and even a skilled worker cannot construct the same structure twice. In addition, these structures can face unanticipated situations for which they were not designed to withstand.

Every model is based on assumptions, and geometrical and physical properties are supposed to be deterministic except if the considered model is stochastic. For example, some parameters like temperature and pre-stresses may be seen as random variables as long as these components cannot be controlled or imposed in some occasions in vibration. Consequently, it becomes important to investigate uncertainties in all kind of structures.

From a probabilistic analysis context, input variables can be considered as stochastic and they can be represented by probability density functions (pdf). Depending on the nature of these variables, specific pdfs are more suitable to represent the randomness of them. Generally, a normal distribution is used, but other types can be more suitable for specific situations as Uniform distribution for the same probability in a range, Lognormal or Gamma for non-negative values, and Beta distribution for strict border values.

In reliability, the limit state function represents the threshold from a safe to a failure state. This state can be a performance requirement that has to be attainted. For periodic structures in vibration control, since a stop band is where there is no wave propagation, a predefined band can be used as condition and trespassing its borders can be a failure state.

These outputs can be more sensitive to the variation of specific input variables. For this reason, before launching an expensive simulation without knowing these parameters, time can be saved by performing a sensitivity analyses. There are several methods to execute the local and global sensitivity analysis. The local one is performed varying one variable and keeping other inputs constants. Consequently, no interaction between input variables can be observed. In global sensitivity, the variation of all considered input parameters is essential to define the importance of each one and the interaction between them. Both sensitivity analyses have to be investigated for satisfactory results. For periodic structures, input variables can have their sensitivity calculated using infinite or finite models using unit cell parameters. Differently, the probabilistic analysis may present distinct results since unit cells are assumed to be perfectly placed side by side in the infinite model and it is not the reality for a finite structure.

After constructing a trustworthy model, it is necessary to know if the model is robust enough to unpredicted situations. Increasing the input variable uncertainty can be a manner to investigate if more robust structures can be constructed and their bandgap regions are not excessively sensitive to input parameters deviations.

1.2 Objectives

In the context described above, the general objective of the research work reported herein is to contribute with new ideas about parametric studies, sensitivity, probabilistic and reliability analysis involving periodic structures in vibration control.

The general objectives established are the following:

- Search for analytical solutions for bandgap borders (Bragg's and local resonance);
- Sensitivity analysis of periodic structure;
- Evaluate numerically the effects of uncertainties on periodic structures;
- Evaluate experimentally the effects of uncertainties on periodic structures;
- Uncertainty propagation on periodic structures.

1.3 Literature Review

Some authors like Newton (1687) and Rayleigh (1887) were important scientists who contributed a lot to the development of the fundamentals of wave propagation. In order to understand in a simple way the wave propagation phenomenon, the governing equation behind the physics and the solutions to this equation, a simple string model is used in the following.

In solid mechanics, a general tridimensional governing equation for wave propagation with no damping can be expressed as (Graff, 1975):

$$\rho\ddot{\mathbf{u}} = \mathbf{f} + (\lambda + 2\mu)\nabla(\nabla.\mathbf{u}) - \mu\nabla\times(\nabla\times\mathbf{u}), \tag{1.1}$$

where λ and μ (G) are the Lamé parameters, ρ is the density, $\mathbf{f}$ is the force vector and $\mathbf{u}$ the displacement vector. There are different ways to solve this differential equation and several types of waves can propagate in this model depending on boundary conditions.

In the right side of equation (1.1), the first term multiplying the Laplacian ($\lambda + 2\mu$) is known as P-wave modulus. The P letter can have two meanings according to literature: Pressure (Dilatational) or Primary. The second term, restricted to shear modulus (G), describes the well-known S-waves. This S can also be interpreted for Shear or Secondary. In geology and earthquake science, these are known as body waves. Normally, waves can be classified in body and surface waves. P (Pressure or Primary) and S (Shear or Secondary) waves represent the first type. Rayleigh, Love and Lamb waves (Graff, 1975; Doyle, 1997) are examples of the second kind. They are equivalent to body waves with specific boundary conditions.

Equation (1.1) can be simplified and a simple example of unidirectional shear wave propagating in a string can be represented by

$$\ddot{\mathbf{u}} = c^2 \nabla^2 \mathbf{u} . \tag{1.2}$$

If the wave is propagating in a string, the wave speed can be calculated using $c = \sqrt{f/\rho}$ where f is the tension and ρ is the linear mass density of the string. This is the simplest governing equation for a propagating wave. The same equation can represent the longitudinal vibration in rods ($c = \sqrt{E/\rho}$, where E is the Young's modulus), torsion waves in beams ($c = \sqrt{G/\rho}$, where G is the shear modulus) or acoustic pressure in ducts ($c = \sqrt{\gamma p/\rho}$ where γ is the adiabatic index and p the pressure).

Figure 1.1 shows a propagating wave in time domain for a fixed-fixed string with two density mismatches in the middle, *i.e.*, a connection from different string densities on positions 0,333 and 0,666. An explicit method using finite differences was used to solve equation (1.2).

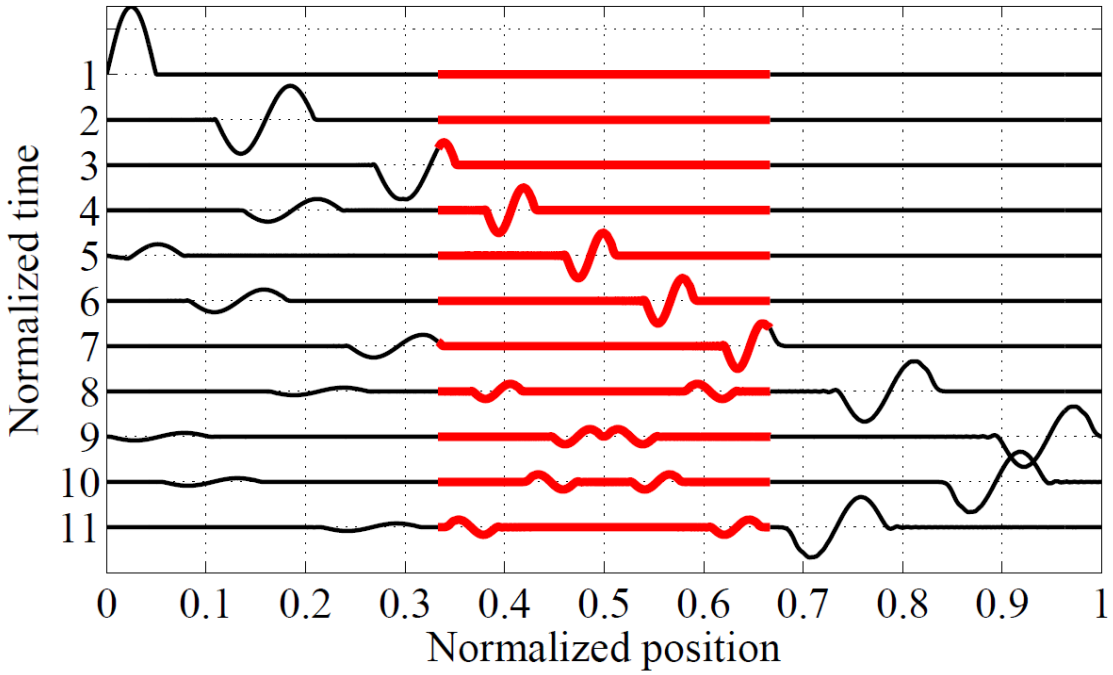

Figure 1.1 Wave propagating in a string with two density mismatches, in normalized positions 0.333 and 0.666, and fixed-fixed boundary contitions.

It is possible to observe the wave interaction with three distinct impedance mismatches, different densities from higher to lower, the inverse and fixed boundary condition, and each one causes a different transmission or reflection of the one-cycle sinusoidal wave. The tension f is the same along this string but the red segment has 4 times the density value of black segments. Consequently, the wave speed in the middle

part is 2 times lower than in the other parts. Even in the absence of damping, the wave amplitude decreases in transmission during the passage of a discontinuity from a black to red part. In the opposite direction, it increases. The reflection on fixed boundary conditions causes the inversion of wave sense but the amplitude remains the same. It is analogous to a reflection from low to high-density part, but with change in amplitude because a part of energy is transmitted. Oppositely, when there is reflection from high to low density part, the speed and amplitude are inverted, the reflected wave has a lower amplitude and part of the energy is transmitted. It is similar for a sliding boundary condition with no transmission and full energy reflection at the end.

The exactitude of input parameters such as same length segments, perfect wave interaction in discontinuities and values for tension and density enable the formation of a moustache picture in the middle of this string when normalized time is 9 in Figure 1.1. Shortly thereafter, these waves interacted destructively. Some questions may appear when all these input parameters are not deterministic and this kind of waves has to be mitigated.

Steady wave or standing waves can be understood as vibration modes (Graff, 1975; Doyle, 1997). Considering harmonic excitation, there is a plenty of methods to control or mitigate the vibration of these modes. They can be mainly classified in two types: active and passive control.

In the first one, it is necessary to inject energy to the system to oppositely suppress or dissipate the undesirable energy. In the second one, no external energy is needed and passive ways of dissipation are used. Reusing the Figure 1.1 with some analogies, introducing a similar motion with same phase but opposite magnitude can create a destructive interference. In active control, generally, a force performed by actuators can be used to compensate for the motion measured by sensors. For passive control, for example, viscoelastic tapes can be glued to the structure adding damping and thermally dissipating energy.

In addition, dynamic vibration absorbers (DVA) can be employed to reduce the vibration level for a determined frequency. The first idea of this mechanism was proposed by Frahm (1907). Den Hartog (1956) presents a complete tuning guide for this.

In optimization of engineering structures, removing or replacing material can produce a more resistant and lighter assemble. However, it is necessary to respect design constraints and safety requirements.

Nowadays, periodic structures have being intensively explored. The repetitive impedance mismatch created by boundary conditions can induce wave interactions that may be beneficial for wave attenuation. A well-chosen material and specially designed geometries can maximize some effects inside these structures.

1.3.1 Metamaterials and Periodic Structures

Metamaterials are artificial materials that present atypical characteristics that cannot be found in naturally occurring materials.

Periodic structures are a particular type of metamaterial and their analysis in scientific literature can be traced back to Newton (1687), when he described the propagation of sound in air, as mentioned by Brillouin (1946). Recently, it was discovered that even spider webs can present periodic properties (Schneider *et al*, 2016). These characteristics can cause waves interferences and energy can be trapped or guided. Bragg (1915) discovered dispersion bandgaps that are frequency bands in which only evanescent waves can occur, rendering any propagation impossible. This finding granted him and his son the physics Nobel prize of 1915 (Bragg, 1922).

In the last few years, the study of these periodic structures has been a very active research in the field of wave propagation and vibroacoustics (Banerjee, 2011). A recent article published in Nature about periodicity in spider webs (Schneider *el al*, 2016) exemplifies the potential of this kind of structures and other examples present in nature are showed in Figure 1.2.

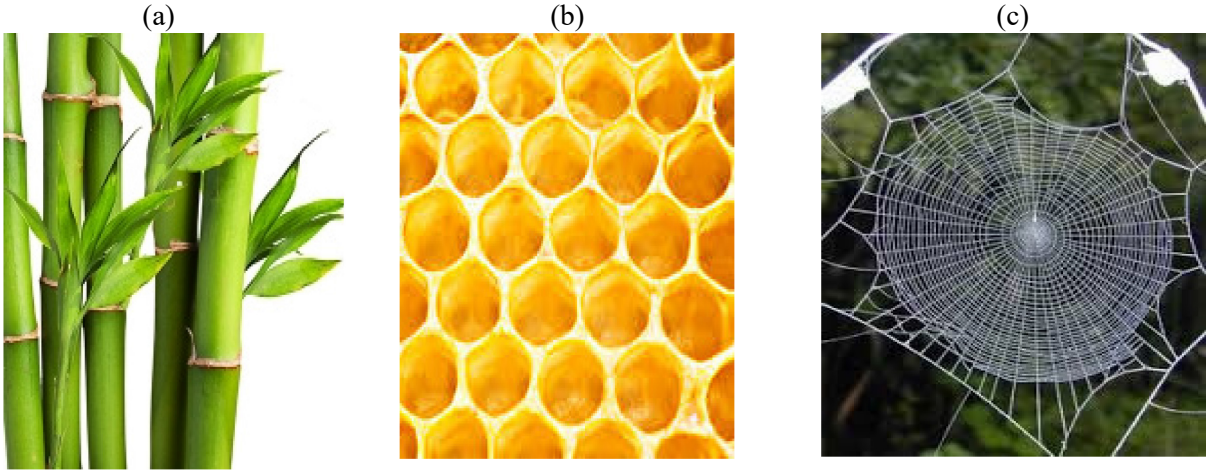

Figure 1.2 Examples of periodic structures in nature: (a) bamboo, (b) honeycomb and (c) spider web.

Many concepts originally developed in physics have been considered in the quest for solutions to different kinds of engineering problems. However, their capacity has not been explored at the same level.

The manifested interest in periodic structures is explained by the unusual phenomena related to wave propagation in periodic systems, which can be found in various physical domains, such as dispersion of sound waves (Hussein *et al.*, 2014), vibrations in solid media (Hussein *et al.*, 2014), propagation of magnetic waves (Sigalas *et al.*, 1996) or light waves and even electron motion (Anderson, 1958). In particular, some studies have demonstrated the great potential of the use of periodic structures for noise and vibration attenua-

tion (Hussein *et al.*, 2014), the protection of buildings against seism motion (Banerjee, 2011) and even the possibility of producing light cloaking and, consequently, artificial invisibility (Banerjee, 2011).

Impedance mismatches, also referred to as discontinuities, can be created by periodically changing physical or geometrical equivalent properties as inertia and stiffness in acoustical and electromagnetic domains. These materials can be classified as phononic and photonic metamaterials, respectively. This periodicity induces wave interactions that can create constructive or destructive interferences. In solid mechanics, repetitive concentrations or even the absence of mass or stiffness can create "mechanical filters" which allows or not the passage of waves in certain frequency bands. These bands are called frequency stop-bands or band gaps.

Several researchers have made significant contributions (Mead, 1996; Hussein *et al.*, 2014; Mester and Benaroya, 1995). Hussein *et al.* (2014) presents an important historic review about the past, present day and future of periodic structures. As mentioned by the authors, there is a great potential. However, different and numerous models considering infinite and finite structures are used. Some of them are discussed in the following.

Briefly, a unit cell is a structure that is repeated side by side to assemble a complete structure. As long as these cells are identical, appropriate periodic boundary conditions (Floquet, 1883; Bloch, 1929) can be taken into account and an infinite model can be created. Considering one dimension, equation (1.3) presents the Floquet-Bloch theorem:

$$X(x+l) = \lambda X(x), \tag{1.3}$$

where $X(x) = \{u(x); f(x)\}$ can be the state vector, with u the displacement and f the force, x the position, l the cell length, or spatial period, and λ is the Floquet multiplier for a unidirectional wave propagation. According to equation (1.3), for $\lambda = e^{\mu}$, equations (1.4a) and (1.4b) are, respectively, the conditions of continuity and equilibrium to the left ($_L$) and right ($_R$) of the unit cells n and $n+1$.

$$u_R^{(n)} = u_L^{(n+1)} = e^{\mu} u_L^{(n)}, \tag{1.4.a}$$

$$f_R^{(n)} = -f_L^{(n+1)} = -e^{\mu} f_L^{(n)}. \tag{1.4.b}$$

These are the boundary conditions of the unit cell. The resolution of the system with these boundary conditions provides $\mu \in \mathbb{C}$ as a function of ω. This variable μ is called propagation constant. It has a real part (δ) and an imaginary part (ε) that are known as attenuation and phase constants, respectively (Mead, 1996; Hussein *et al.*, 2014). For a purely imaginary μ, the waves propagate and the frequency zone is a pass band. For a real μ, the waves are attenuated and this zone is a stop band, also known as a band gap.

Orris and Petyt (1964) used the finite element technique to evaluate periodic structures. They show that this method is simple to apply and very complex structures can be analyzed. Nonetheless, its convergence has to be always checked and the higher the number of finite elements, the higher the computational cost.

Using an exact wave-based method, Leamy (2012) shows a procedure that is more faithfull to reality while modeling the finite nature of 2D lattice connections. This characteristic makes this method attractive for uncertainty analysis. If the finite element models are ready to use, it is possible to investigate physical properties of complex systems.

Bragg's band gaps are created according to cell length and discontinuity position while local resonance bandgaps are created as consequence of superimposing the effect of multiple resonators in same frequency.

Clayes *et al.* (2013) show that resonance band gaps can provide stop-bands in lower frequencies with more attenuation than Bragg's band gaps (Bragg, 1915), although, the first type of attenuation zone has a narrower band comparing to second one.

The influence of damping and damping localization is addressed by Jensen (2003) and Bouzit and Pierre (1995a). The last authors analyze the influence of damping in periodic structures and compare the energy confinement or dispersion and energy dissipation created by periodic and damped structures, respectively. Collet *et al.* (2012) also analyzes a periodic damped structure.

The presence of defects in 2D periodic structures is explained by Movchan (2006) and new kinds of repetitive structures are also investigated. For example, cyclic periodic structures are presented by Xie and Ariatanam (1996a, 1996b). Jensen and Pedersen (2006) presented an interesting work about topological optimization and Xie (1997) about disordered large planar lattice trusses.

New kinds of structures inspired by Fibonacci series and fractals were also studied by many researches (Poddubny and Ivchenko, 2010). Chen and Wang (2007) analyzed quasi-periodic structures and investigate other kind of periodicity imposed by Fibonacci aperiodic structures compared to periodic disordered structures. This type of structure can be interesting due to its capacity of superimposing attenuation zones. The same property is presented by Trainiti *et al.* (2016) with graded undulated structural lattices.

Periodic structures with auxetic properties (negative Poisson coefficient) can redirect the energy as presented by Billon *et al.* (2016) using hierarchic structures and by Ruzzene and Scarpa (2005) with honeycombs with different geometries.

Moreover, these structures can be tuned and this subject is expected to continue attracting interest in the future, as discussed by Hussein *et al.* (2014). A powerful and wise solution can be the use of smart materials and structures with periodic structures.

1.3.2 Smart materials and structures

One important step before describing the smart structures is to describe the smart materials. In this work, their use is focused on vibration control by actuating and sensing vibration.

According to Leo (2007), smart materials exhibit coupling between multiple physical domains. In other words, they have the capacity to convert energy from one domain to another.

The most important characteristic of smart materials is their capacity of self-sensing and self-changing to adapt to new conditions according to design requirements. Some fundamental aspects of these intriguing materials can be found in (Leo, 2007).

Figure 1.3 Examples of Smart Materials: (a) Piezoelectric and (b) Shape memory polymers (reproduced from Butaud et al. (2016)).

Figure 1.3 shows two types of these materials: piezoelectric and shape memory polymers (Butaud *et al*, 2016). The first set consists in ceramic materials that convert energy between mechanical and electrical domains. The second one is thermomechanical material that deforms when heated and cooled.

Ruzzene and Baz (2000) shows a periodic rod with shape memory inserts that are placed periodically along a rod to act as a source of controllable impedance mismatch by changing the temperature and, consequently, the elastic modulus. Similarly, but for a plate structure with steel cylinders, Billon (2016) uses the temperature change as a switch effect. A shape memory polymer is placed between the plate and the cylinder and, for high temperatures, the structure loses the periodicity effect.

Giving a special attention to piezoelectric materials, a seminal work about PZT patches with shunt circuits was done by Hagood and Von Flotow (1991). They developed the idea of a dynamic vibration absorber, as presented by Den Hartog (1956) or Frahm (1907), using electric resonator instead of classical mechanical one.

For example, if a piezoelectric actuator is linked in series with a resonant shunt circuit, it will dynamically behave as adding a Dynamic Vibration Absorber (DVA) (Leo, 2007; Hagood and Von Flotow, 1991; Preumont, 2004). This kind of mechanism creates resonant bandgaps if placed periodically in a structure. More information about DVAs can be found in (Den Hartog, 1956; Korenev and Reznikov, 1993; Rade and Steffen, 2000). The principle behind this strategy is that the vibrational energy is transformed into electric energy through the direct piezoelectric effect and is transferred to the circuit where it is partially dissipated and/or dispersed. Among the types of used electric circuit, RL, known as resonant circuits, are considered as some of the most efficient (Hagood and Von Flotow, 2013; dell'Isola *et al.*, 2004). Such circuits comprise an inductor and a resistor that are connected to the piezoelectric transducer that is assimilated to a capacitor, thus forming an RLC circuit. When coupled to a dynamic system, this device operates similarly to a dynamic vibration absorber (DVA). For example, Thorp *et al.* (2001) uses shunted piezoelectric patches along rods to control longitudinal vibration. Distributing these devices may lead to multimodal control (dell'Isola *et al.*, 2004). As adding damping for DVAs, adding electrical resistance adds damping for energy dissipation in a same way. For example, using a periodic array of piezoelectric patches, Lossouarn *et al.* (2015a, 2015b) shows a multimodal vibration damping of a rod and a beam and Tateo *et al.* (2014b) in a plate and Collet *et al.* (2012) defines the optimal electric impedance of the shunt circuit.

Claeys *et al.* (2013) describes the difference between placing a localized mass and a DVA in a periodic structure. Normally, increasing the mass density in one specific degree of freedom (*dof*) in a unit cell may create a large band gap but with weak attenuation. Oppositely, by adding a spring-mass dof, it is possible to create resonant band gaps whose attenuation zones are narrower but with strong dispersion thanks to lower frequency response amplitudes. Collet *et al.* (2012) and Tateo *et al*. (2014a) show that it is possible to synthetize negative resistance or capacitance with operational amplifiers, but it needs inserting energy in the system and it is a semi-passive method. The main advantage of using piezoelectric actuators, rather than DVAs, is the characteristic of no addition of significant mass to the main structure and the convenience of electronically tuning without changing geometric properties. Moreover, these circuits can be redesigned and unusual behaviors can be included. One example of this is the negative capacitance shunting (Park and Baz, 2005), which aims at removing the intrinsic capacitive effect of the piezoelectric patch (Marneffe and Preumont, 2008). This may be combined with resonant circuits (Casadei *et al*, 2012), opening the way to new strategies with wideband efficiency (Lossouarn *et al.*, 2015, Tateo *et al.*, 2014a; Tateo *et al.*, 2014b).

Signorelli and Von Flotow (1987, 1988) show the wave propagation behavior in 2D truss structures by using beam finite element and the Transfer Matrix method. This sort of structure also has the weightlessness as its major characteristic. In virtue of this, the use of piezoelectric actuator in these lattices structures seems to be a good compromise because it favors the lightness design requirements. Nevertheless, uncertainty and robustness analysis are rare in literature. Near-periodic structures, defects, impurities in periodic structures and the localization phenomena are well detailed in (Li and Benaroya, 1992; Li and Benaroya, 1994a, 1994b; Mester and Benaroya, 1995), but robustness analyses are scarce.

The robustness of these repetitive structures whose attenuation zones are created and passively controlled by using piezoelectric stack actuators is associated with electrical shunt circuits (Leo, 2007; Hagood and Von Flotow, 1991). Just like DVAs, shunt circuits must be tuned, which means that the values of their electric parameters must be precisely chosen for vibration attenuation in a narrow frequency band. However, the characteristic values of electronic components are prone to variability, due to manufacturing process and temperature, which can lead to mistuning and, consequently, decreasing of the control performance.

In this scenario, it becomes essential to evaluate the probability that the system will comply with the design requirements, given the probability density functions ascribed to the uncertain variables considered. Periodic nature for dispersion and damping nature for dissipation can be used together to improve the attenuation. The capacity of tuning incorporated to periodic structures can be a solution, adding robustness to the system and, for example, compensate any structural uncertainty.

Truss structures are versatile by themselves because of their properties as high resistance and low weight compared to solid profiles. To exemplify this polyvalence, their configuration can be optimized according to the local of high solicitations to increase their resistance. In addition, this kind of structure presents repetitive substructures, but, normally, this characteristic is still uninvestigated despite its potential for passively controlling vibration. Furthermore, this structure can be combined with smart bars or beams to explore the tunability of periodic materials and increase its robustness.

More information about periodic and smart structures is shown in (Thorp *et al.*, 2001) and (Spadoni *et al.*, 2009). Another advantage of incorporating smart structures to periodic structures is the possibility of managing non-perfect periodicity while tuning semi-passive shunt circuits. It is possible either to compensate manufacturing defects or voluntarily breaking the periodicity. From a more academic point of view, it opens the way to the control of uncertainties for experimental validation of stochastic methods. In addition, some aspects like localization phenomena can be deeply investigated in both cases: Bragg scattering and local resonances.

There are several methods to model periodic structures. However, the same methodology cannot be used for all mentioned structures because, as the structure becomes more complex, closed form exact analytical solutions are not available anymore.

The Transfer Matrix method, generally used in acoustics or elastic waves (Thompson, 1950), can be a good choice for 1D waves. However, it can present instability problems. Dazel *et al.* (2013) proposes a recursive method to avoid matrix multiplication. Other alternatives like wave method (Leamy, 2012); receptance method (Mead, 1996) can be used to obtain exact analytical solutions. For more complex unit cells, the use of numerical methods like Plane Wave Expansion (PWE), Semi-Analytical Finite Element (SAFE) (Gravic, 1995), Finite-Difference Time- Domain (FDTM) and Wave Finite Element (WFE) (Mencik, 2014; Silva *et al.*, 2016). However, some of these numerical methods can present excessive computational cost for complex unit cells and it becomes impracticable.

Signorelli and Von Flotow (1988) showed that a truss presents some complex modes while modelling a truss with beam finite elements. These modes are not easy to interpret. There is a possibility that these

modes are related to the resonance of internal components. Chesnais *et al.* (2012) described these inner resonances using an analytical method to represent a truss with equivalent beam models. Noor *et al.* (1978) also investigated the periodicity of truss structures. Trainiti *et al.* (2015, 2016) considered undulated frames, which seems to be motivated by symmetric and antisymmetric Lamé modes, presented the coupling effect of different types of waves.

These references illustrate the great potential of these structures. However, probabilistic analysis of these structures is a scarce subject in literature. In practical applications, all parameters used in these works present uncertainties and this can jeopardize their envisaged effect.

Several researchers have already made significant contributions (Mead, 1996; Hussein *et al.*, 2014; Mester and Benaroya, 1995) according to periodic structures. However, from a probabilistic point of view, there is a very low number of contributions about the influence of uncertainties in these structures and their robustness. Like any type of structure, these systems are inevitably subjected to the presence of uncertainties in the physical and geometrical parameters (Haldar and Mahadevan, 2000; Lemaire, 2009; Melchers, 1987). Stochastic approaches are widely used in various engineering fields to estimate the impact of parametric or even non-parametric uncertainties (Ichchou *et al.*, 2011) on the features of interest. As far as periodic structures are concerned, some very early works suggested that considering uncertainties in the analyses might be of importance. For example, Montroll and Potts (1955) explained the effect of defects on lattice vibrations, a few years before Anderson's discovery (1958): he suggested the Localization Phenomena in his paper about "Absence of Diffusion in Certain Random Lattices" which granted him the physics Nobel prize of 1977 (Anderson, 1977). After him, many researchers followed the same domain investigating deeply this interesting revelation (Bogdanoff and Chenea, 1961; Soong and Bogdanoff, 1963; Bliven and Soong, 1969).

Some interesting aspects about disorder (Bansal, 1978; Lin and Yang, 1974; Lin, 1996), impurities, irregularities (Hodges, 1982) or defects and imperfections (Luongo, 1992) have been investigated. To our best knowledge, many articles about the localization phenomena in disordered periodic structures have been published, but no study about their robustness and/or reliability was carried-out.

Li and Benaroya (1994) present in a simple way how localization phenomena happens in rod structures with longitudinal displacement. In their review, Mester and Benaroya (1995) show the most important contributions considering uncertainties in periodic and near-periodic (disordered) structures and some important concepts as quasiperiodic, aperiodic or near-periodic structures, which are used by many authors to describe the disordered structures. Bansal (1997) states that, in reality, due to manufacturing limitations, engineering structures are not ideally periodic and they are disordered in the sense that the cells are not identical. They can have random imperfections.

Lin (1996) makes an important view about uncertainties saying that the ignorance and the lack of capacity to control all parameters in a simulation forces the need of considering uncertainties.

Hodges (1982) has shown that confinement of vibration by irregularity is another way to refer to localization phenomena. Kissel (1988; 1991) also explains this phenomenon in his doctorate thesis. Some exper-

imental results are presented by Bouzit and Pierre (1995); Junyi and Balint (2015) and Junyi et al. (2016) who found it experimentally because of boundary conditions.

1.4 Research context

The main purpose of this work is to describe how uncertainties affect the performance of a smart periodic truss designed for vibration control. Indeed, longitudinal, shear and flexural waves can all propagate at a same time on the structure depending on the excitation type. These periodicities can create bandgaps in different frequency bands for each type of wave. Moreover, Bragg's, resonance and coupling modes bandgaps can appear as described in literature. There is a huge new horizon to explore.

For the sake of clarity, in the present work, there is a progressive development of the uncertainty subject from simple structures as spring-mass systems, continuous bars and beams to smart trusses. The schematic idea is represented in Figure 1.4.

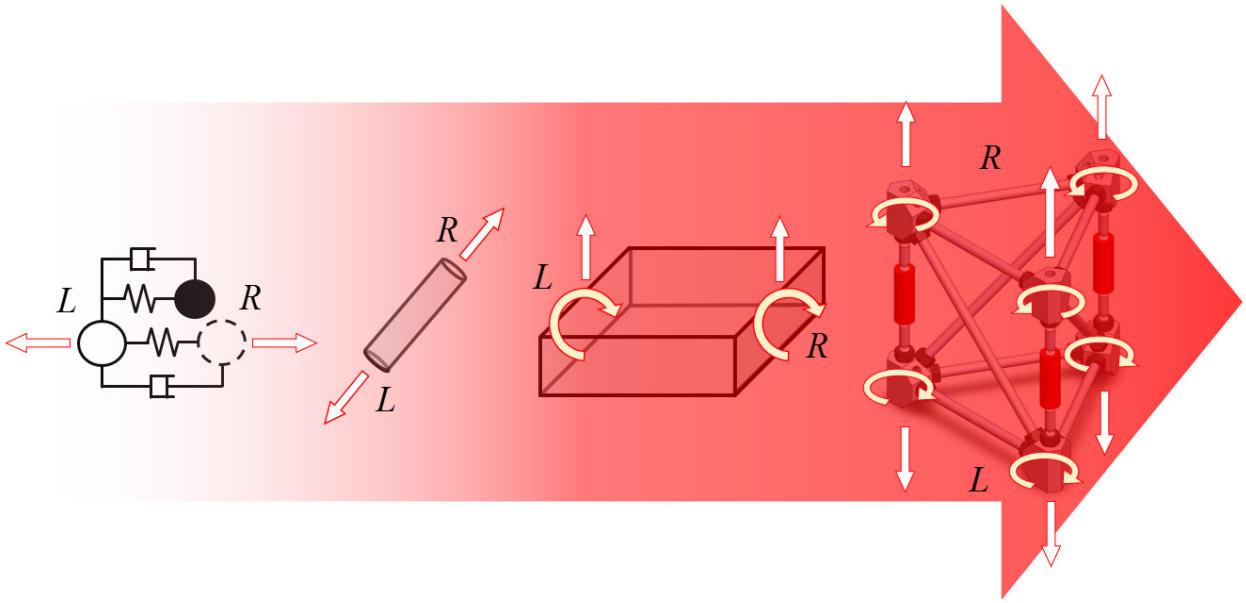

Figure 1.4 Evolution from spring-mass systems, rods and beams to smart trusses.

Firstly, before engaging probabilistic analysis, an accurate and efficient program is necessary. Therefore, some methods were considered as showed in Figure 1.5. The criteria for choosing these methods were, firstly, the presence of analytical solution to avoid numerical errors and, secondly, the fastest semi-analytical and numerical solutions to the best of our knowledge.

Model	Solution Type	Movement equation	Proposed solutions for periodic structures	Proposed examples
Infinite (Dispersion diagrams)	Analytical **(Partial derivatives)**	Unit cell differential equation (UCDE)	Transfer Matrix	Spring-mass, Rod, Beam
		General solution of UCDE	Transfer Matrix	Rod, Beam
(Sensitivity and/or parametric study)	Numerical **(Finite differences)**	Unit cell complete model (CU)	Finite Element Method	Rod, Beam, Truss
Finite (Frequency Response Functions)	Analytical or semi-analytical	Differential equation (DE)	Transfer Matrix **(Instable)**	Spring-mass, Rod
			Translation Matrix	Beam
		General solution of DE	Transfer Matrix **(Instable)**	Rod
			Translation Matrix	Beam
(Robustness)	Numerical	Complete model	Finite Element Method **Numerically expensive (mesh convergence)**	Truss

Figure 1.5 Proposed solutions.

In the context outlined above, the specific objectives of the research work reported herein are:

- Analyze longitudinal waves using Transfer Matrix method on:
  - spring-mass systems considering Bragg's and local resonance bandgaps for
    - Analytical local sensitivity analysis using partial derivatives;
  - stepped rod unit cell considering Bragg's bandgaps for
    - Numerical local sensitivity analysis using finite differences;
    - Probabilistic analysis using infinite and finite models;
- Analyze flexural waves using Translation Matrix method to:
  - perform a parametric study on geometrical properties;
  - perform a probabilistic analysis using infinite and finite models;
- Experimental evaluation on random dimensions of periodic structures;
- Probabilistic analysis of classical and smart periodic trusses using finite and infinite models.

1.5 Organization of the thesis

This thesis is organized in six chapters, including this first, devoted to contextualization of the research work and statement of the objectives. All of them describe 1D wave propagation but involving one to several sorts of waves. For the sake of easy understanding, there is a progression of ideas from simple structures to complex ones.

In the second chapter, simple models of continuous bar and spring-mass systems are considered. The basic concepts necessary to comprehend infinite models are enlighten. The Transfer Matrix method is used and the exact solution for these periodic structures is presented. There is an inspection of Bragg's and local resonance stop bands. Local sensitivity analyses are performed. A probabilistic analysis is carried out using Monte Carlo Simulation combined with Latin Hypercube sampling.

In the third chapter, flexural waves in periodic structures are investigated. Simple models using continuous Euler-Bernoulli beams are analyzed. The Translation Matrix method is presented using a recursive method. A probabilistic analysis is carried out using the same idea as the previous chapter.

The fourth chapter presents an experimental survey of previous structures. A complete model presenting longitudinal, flexural and shear waves is used. The experiments aimed to verify what was proposed numerically in the previous chapters.

The fifth chapter addresses truss structures with periodic assumptions. A probabilistic analysis is performed with a bar finite element tridimensional truss composed by passive and active members. A beam finite element tridimensional truss is used to investigate the inner resonance effects.

Finally, the sixth chapter presents the final conclusion and perspectives.

Chapter 2 Longitudinal waves

2.1 Introduction

A beam-like truss will always present 1D waves. This type of wave can be represented by a discrete model using a simple spring-mass system or by a continuous model using a uniform rod. For the first model, two kinds of stop bands can be created. They are known as Bragg's and local resonance bandgaps. The second model can present just Bragg's scattering as long as discrete mass-springs are not attached to the rod.

For both cases, considering just scattering and no resonance, the relation between wavelength and cell length (spatial periodicity), and the distance between positions of wave reflection, determine the frequency around which this attenuation zone can be created. However, intensity and type of impedance mismatch also define the frequency borders of this zone because they change wave reflection and transmission behaviors. The presence of discontinuities caused by inertia or stiffness change can shift the stop band position.

The Transfer Matrix method is a powerful technique to deal with periodic arrangements of unit cells, in which analytical description of the movement of the cells can be used. This method, also known as Thompson-Haskell Method (Dazel *et al.*, 2013; apud Thompson, 1950; Haskell, 1953), is widely used in acoustics for sound wave propagation through multilayers. For multi-coupled models, this method can present instability problems as the number of degrees of freedom increases. However, it provides accurate results for mono-coupled systems in low frequency band.

In this chapter, a general spring-mass unit cell is generated based on the formulation presented by Brillouin (1946) and Hussein *et al.* (2014). The goal is to find the analytical equations for the frequency value on attenuation zones borders and to enlighten the procedure to extend the same methodology to more complex structures. The principal advantage of these analytical equations is that their partial derivatives in function of any input parameter can be easily obtained. This measure can represent the local sensitivity of a function and an explicit implementation reduces the computational cost. The calculation is faster and the results are more accurate as compared to numerical analysis. It is also convenient for a probabilistic analysis that normally needs a high number of samples.

Following this line of reasoning and considering a continuous rod, this chapter also proposes a method to determine a robust bandgap according to considered uncertainty levels. After knowing the advantages of each methodology, the following work is also based on Transfer Matrix method for a simple rod model

(Ruzzene and Baz, 2000; Ruzzene and Scarpa, 2003; Lin, 1996) and its mode shapes are used to better explain the localization phenomena.

Initially, a simple non-periodic rod model is proposed and its exact solution is presented. In a second step, this rod is divided into two segments and its exact solution is also achieved considering the same material and different cross section areas. This two segments rod is used as unit cell and the transfer matrix is used to find the exact solution for finite and infinite structure models. The frequency response function is obtained by using a spectral method (Doyle, 1997) and the dispersion constants are found by solving an eigenvalue problem.

A local sensitivity analysis is performed using an infinite model to discover the most influential input variables in band gaps frequency characteristics. It is important to mention that this analysis is performed with one cell repeated infinitely. Therefore, the effect of only one cell in a finite structure is not observed for this analysis. After, a brute force Monte Carlo Simulation (Haldar and Mahadevan, 2000; Lemaire, 2009; Melchers, 1987) is used to model the stochastic behavior of this structure to compare the effect of uncertainties considering an infinite and a finite structure.

For finite periodic structures, the number of cells increases the wave attenuation inside band gaps. However, the finite structures studied in this chapter can present natural frequencies inside the attenuation zones. These modes cannot be found by calculating the dispersion constants. This peculiarity is known as localization phenomena (Anderson, 1958) and it is well detailed by Mester and Benaroya (1995). For specific situations, this mode can be found by considering a single cell eigenvalue problem (Mead, 1975a; Mead, 1975b; Hvatov and Sorokin, 2015), but this is not deeply investigated here. However, some other effects due to random localized modes contribute to intensify the natural robustness of this kind of structure.

Finally, a probabilistic numerical example is used to explain this special characteristic and the notion of robust bandgaps is established considering infinite and finite models.

The main contributions are the novelties related to the robustness of periodic structures, while comparing infinite and finite models, and investigations about localization phenomena corresponding to one cell free-free spectral analysis and strong impedance mismatch for a specific cell. This fact can create localized modes and cause the misinterpretation of bandgap borders. As long as these localized modes are inside the attenuation but they do not change the band gap border value, *i.e.*, for a finite structure composed by numerous unit cells, these characteristics add robustness to this kind of structure. However, if the number of cells it low, this natural frequency can change the bandgap border.

2.2 Longitudinal waves in rods

2.2.1 Discrete systems

Spring-mass chains can be used to represent a dispersive-media for longitudinal vibration. The purpose of using this model is to investigate the differences between Bragg and local resonance bandgaps. Similar to the model proposed by Hussein *et al.* (2014), the unit cell presented on Figure 2.1 is used to obtain a general spring-mass model using Transfer Matrix method.

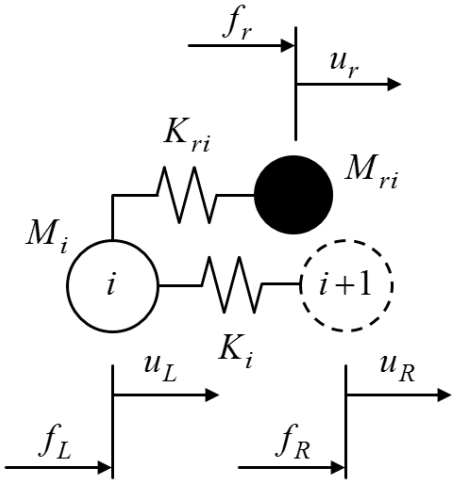

Figure 2.1 Example of spring-mass unit cell.

A spring-mass system with two masses, M_i and M_{ri}, and two springs, K_i and K_{ri}, is presented in Figure 2.1. The mass and the spring with subscript *r* indicate that they are connected as an internal resonator- to the first mass. As long as there is no internal force in this case, f_r is equal to zero. In the whole chapter, no damping is considered and the governing equation of this unit cell is represented by:

$$\mathbf{M}\ddot{\mathbf{U}}(t) + \mathbf{K}\mathbf{U}(t) = \mathbf{F}(t), \tag{2.1}$$

where $\mathbf{M}$ is the mass matrix, $\mathbf{K}$ is the stiffness matrix, $\mathbf{U}$ is the vector with displacements and $\mathbf{F}$ is the force vector in function of time *t*. The equation (2.2) shows the matrices and vectors elements of equation (2.1).

$$\begin{bmatrix} M_i & 0 & 0 \\ 0 & M_{ri} & 0 \\ 0 & 0 & 0 \end{bmatrix} \begin{Bmatrix} \ddot{u}_L \\ \ddot{u}_r \\ \ddot{u}_R \end{Bmatrix} + \begin{bmatrix} K_i + K_{ri} & -K_{ri} & -K_i \\ -K_{ri} & K_{ri} & 0 \\ -K_i & 0 & K_i \end{bmatrix} \begin{Bmatrix} u_L \\ u_r \\ u_R \end{Bmatrix} = \begin{Bmatrix} f_L \\ 0 \\ f_R \end{Bmatrix}, \tag{2.2}$$

Considering a harmonic solution, $u_L = \hat{u}_L e^{j\omega t}$, $u_R = \hat{u}_R e^{j\omega t}$, $f_L = \hat{f}_L e^{j\omega t}$ and $f_R = \hat{f}_R e^{j\omega t}$, the following equation can be found

$$\begin{bmatrix} -M_i\omega^2 + K_i + K_{ri} & -K_{ri} & -K_i \\ -K_{ri} & -M_{ri}\omega^2 + K_{ri} & 0 \\ -K_i & 0 & K_i \end{bmatrix} \begin{Bmatrix} \hat{u}_L \\ \hat{u}_r \\ \hat{u}_R \end{Bmatrix} = \begin{Bmatrix} \hat{f}_L \\ 0 \\ \hat{f}_R \end{Bmatrix}. \tag{2.3}$$

The absence of force on internal resonator allows the condensation of this degree of freedom and the equation (2.4) is obtained,

$$\begin{bmatrix} K_i\left(1-\Omega^2\right) - K_{ri}\left(\dfrac{\Omega_{ri}^2}{1-\Omega_{ri}^2}\right) & -K_i \\ -K_i & K_i \end{bmatrix} \begin{Bmatrix} \hat{u}_L \\ \hat{u}_R \end{Bmatrix} = \begin{Bmatrix} \hat{f}_L \\ \hat{f}_R \end{Bmatrix}, \tag{2.4}$$

where the dimensionless frequency is $\Omega = \omega/\omega_0$ with $\omega_0 = \sqrt{K_i/M_i}$ and the dimensionless tuned frequency is $\Omega_{ri} = \omega/\omega_{ri}$ with $\omega_{ri} = \sqrt{K_{ri}/M_{ri}}$. Using equation (2.4), the Transfer Matrix method can be used to model infinite and finite arrangements of spring-mass systems.

Rearranging the equation (2.4), the corresponding degrees of freedom on the right (*R*) and on the left (*L*) can be disposed as

$$\begin{bmatrix} \left(1-\Omega^2\right) - \dfrac{K_{ri}}{K_i}\left(\dfrac{\Omega_{ri}^2}{1-\Omega_{ri}^2}\right) & -\dfrac{1}{K_i} \\ -K_i\Omega^2 - K_{ri}\left(\dfrac{\Omega_{ri}^2}{1-\Omega_{ri}^2}\right) & -1 \end{bmatrix} \begin{Bmatrix} \hat{u}_L \\ \hat{f}_L \end{Bmatrix} = \begin{Bmatrix} \hat{u}_R \\ \hat{f}_R \end{Bmatrix}, \tag{2.5}$$

which writes $\mathbf{y}_i(x_i + l_i, \omega) = \mathbf{T}_i(\omega)\mathbf{y}_i(x_i, \omega)$ with $\mathbf{y}(x_i, \omega) = \begin{bmatrix} \hat{u}_i & \hat{f}_i \end{bmatrix}^T$. Considering the *dofs* on the right and on the left of cell i, one has

$$\begin{Bmatrix} u_R \\ -f_R \end{Bmatrix}^{(i)} = \mathbf{T}_i(\omega) \begin{Bmatrix} u_L \\ f_L \end{Bmatrix}^{(i)}. \tag{2.6}$$

Assuming different cells, *i* and *i*+1, maintaining continuity $u_R^i = u_L^{i+1}$ and equilibrium $f_R^i = -f_L^{i+1}$, the left side *dofs* can be represented by

$$\begin{Bmatrix} u_L \\ f_L \end{Bmatrix}^{(i+1)} = \mathbf{T}_i(\omega) \begin{Bmatrix} u_L \\ f_L \end{Bmatrix}^{(i)}, \tag{2.7}$$

To assemble a finite structure, these Transfer Matrices can be sequentially multiplied and the relation between state vectors from first cell to the *n*-th cell is

$$\begin{Bmatrix} u_L \\ f_L \end{Bmatrix}^{(n)} = \prod_i^{n-1} \mathbf{T}_{n-i}(\omega) \begin{Bmatrix} u_L \\ f_L \end{Bmatrix}^{(1)} . \tag{2.8}$$

This equation can be rearranged back as

$$\begin{Bmatrix} u_L \\ u_R \end{Bmatrix} = \mathbf{D}(\omega) \begin{Bmatrix} f_L \\ f_R \end{Bmatrix}, \tag{2.9}$$

where the dynamic flexibility matrix is

$$\mathbf{D}(\omega) = \begin{bmatrix} -\mathbf{T}_{12}{}^{-1}\mathbf{T}_{11} & \mathbf{T}_{12}{}^{-1} \\ \mathbf{T}_{21} - \mathbf{T}_{22}\mathbf{T}_{12}{}^{-1}\mathbf{T}_{11} & \mathbf{T}_{22}\mathbf{T}_{12}{}^{-1} \end{bmatrix}^{-1} = \begin{bmatrix} -\mathbf{T}_{21}{}^{-1}\mathbf{T}_{22} & \mathbf{T}_{21}{}^{-1} \\ \mathbf{T}_{12} - \mathbf{T}_{11}\mathbf{T}_{21}{}^{-1}\mathbf{T}_{22} & \mathbf{T}_{11}\mathbf{T}_{21}{}^{-1} \end{bmatrix}, \tag{2.10}$$

with $\mathbf{T}_{12}$, $\mathbf{T}_{21}$, $\mathbf{T}_{22}$ and $\mathbf{T}_{11}$ the line and column components of multiplied transfer matrix. Using $\mathbf{T}(\omega)$ and $\mathbf{D}(\omega)$, infinite and finite models can be implemented. Dispersion constants can be obtained by calculating the eigenvalues of $\mathbf{T}(\omega)$ and the frequency response functions can be obtained by choosing the corresponding *dofs* of excitation and response in $\mathbf{D}(\omega)$.

Figures 2.2(a), 2.2(b) and 2.2(c) show the dispersion diagrams calculated using the resultant transfer matrix for three different cases. They consider a unit cell with one, two and three spring-mass subsystems, whose properties are listed in Table 2.1. In these simulations, no internal resonators are considered ($M_{ri} = 0$).

The propagation constants are $\mu = \delta + i\varepsilon$, being δ the attenuation constant (for evanescent waves) and ε the phase constant (for propagating waves).

The magnitudes of their respective frequency response functions, computed by considering one and ten cells, are depicted in Figures 2.2(d), 2.2(e) and 2.2(f).

Table 2.1 Spring and mass values for three types of unit cells (without internal resonators).

Cases	**unit cell**	M_1	K_1	M_2	K_2	M_3	K_3
1	1 Mass + 1 Spring	1	1	-	-	-	-
2	2 Masses + 2 Springs	1	1	2	1	-	-
3	3 Masses + 3 Springs	1	1	2	1	1	1

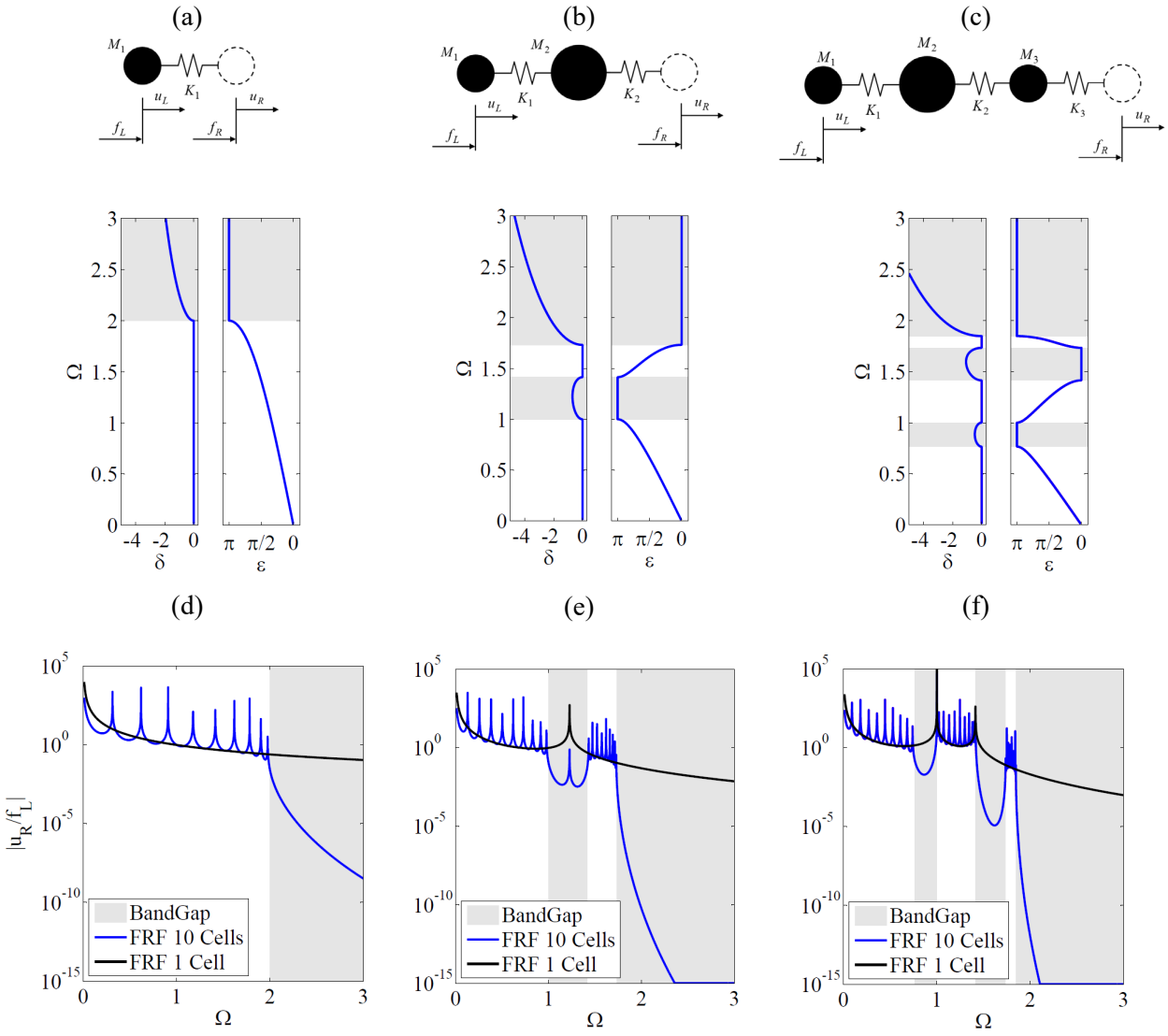

Figure 2.2 Dispersion diagrams for different unit cells: (a) case 1, (b) case 2 and (c) case 3, and FRF amplitudes computed for 1 and 10 cells: (d) case 1; (e) case 2; (f) case 3.

The frequency responses for one cell shown in Figures 2.2(d), 2.2(e) and 2.2(f) show that if there are natural frequencies inside the bandgap region (grey areas identified in the dispersion diagrams), these peaks are also present inside this attenuation zone for a finite structure with ten cells (see Figure 2.2(e)). It is important to notice that if these frequencies are near to bandgap borders, they can overlay the borders calculated using dispersion constants on Figures 2.2(a), 2.2(b) and 2.2(c) and it creates different border values for finite structures analysis. If the number of cells is increased, the contribution of these natural frequencies decreases and can be neglected.

Other three different types of unit cells are presented in Table 2.2 considering an internal resonator attached to the first mass. It is known that the goal of a resonator-type DVA is incorporate a resonant structure with no more than 5% of main structure mass to reduce the vibration amplitude at a specific forcing frequen-

cy. However, with the purpose of obtaining larger local resonance bandgaps, the values of attached mass and spring have the same magnitude of the main spring-mass.

Table 2.2 Spring and mass values for three types of unit cell with a resonator attached to mass 1.

Cases	Spring-Mass unit cell	M_1	K_1	M_2	K_2	M_{r1}	K_{r1}
4	1 Mass + 1 Spring + 1 resonator	1	1	-	-	1	1
5	2 Masses + 2 Springs + 1 resonator	1	1	1	1	1	1
6	2 Masses + 2 Springs + 1 resonator	1	1	2	1	1	1

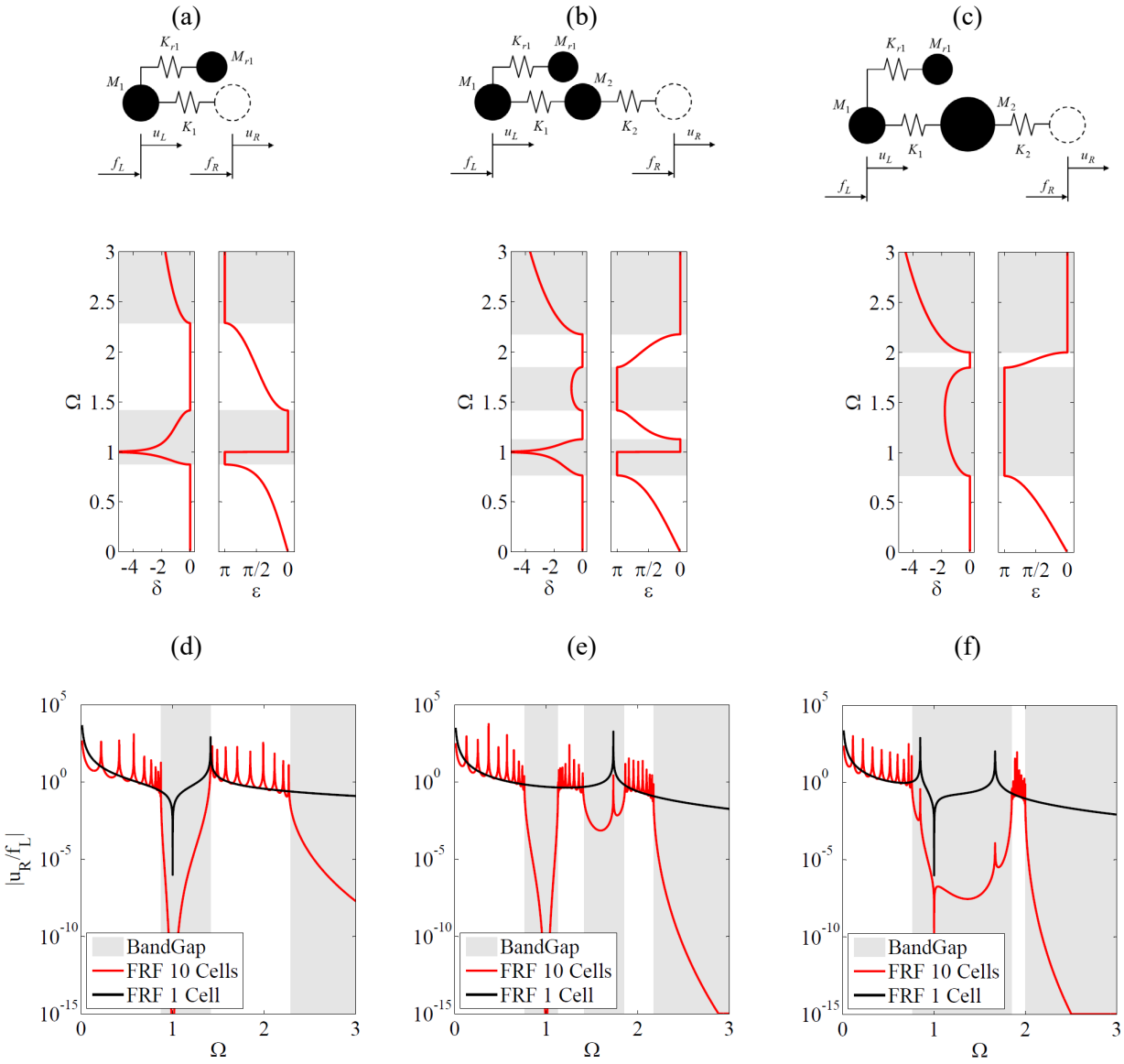

Figure 2.3 Dispersion diagrams for different unit cells: (a) case 4, (b) case 5, (c) case 6 and FRF amplitudes computed for 1 and 10 cells: (d) case 4; (e) case 5; (f) case 6.

It is possible to observe in Figures 2.3(a) and 2.3(d) that the local resonance bandgap has a stronger attenuation than Bragg's bandgap presented in Figures 2.2(b) and 2.2(e). Figures 2.3(b) and 2.3(e) present these two kinds of stop-bands. Differently, the dispersion constants of Figure 2.3(c) seem to present just a Bragg's band-gap, while the frequency response functions of Figure 2.3(f) show the presence of two resonance peaks and an anti-resonance inside the attenuation zone. In fact, the model should have these two typical kinds of stop bands, because the presence of a second mass with different value from first mass and a resonator attached to the first one. Nonetheless, there is the appearance of a unique attenuation zone.

All lower and upper borders of the grey regions in Figures 2.2 and 2.3 were obtained with analytical equations, as explained in the following.

Bragg and local resonance bandgaps are created by different physical mechanisms. The first one depends mainly on the cell length and the position of impedance mismatch, while the second one depends on the frequency the resonant mass is tuned with. In spite of having different origins, their band-gap borders can be found using the same formulation. The analytical expressions of these borders can be found by solving a quadratic equation while calculating the eigenvalue of the transfer matrix ($\det(\mathbf{T}(\Omega)-\lambda I)=0$). For example, if a unit cell with one spring-mass system and no resonator is considered, the quadratic equation $\lambda^2+(\Omega^2-2)\lambda+1=0$ is obtained. Its two solutions are given by:

$$\lambda_{1,2}=\left(\frac{2-\Omega^2}{2}\right)\pm\sqrt{\left(\frac{2-\Omega^2}{2}\right)^2-1}\,. \tag{2.11}$$

Considering the point where real and imaginary solutions of $\lambda_{1,2}$ intersect, *i.e.*, the value inside the square root is zero, the values for dimensionless frequencies are $\Omega_1=0$ (*i.e.* $\omega_1=0$) and $\Omega_2=2$ (*i.e.* $\omega_2=2\sqrt{K/M}$). The first non-null border value for the case with one spring-mass is defined as $\omega_{11}=\omega_2$. The same methodology can be applied to any system with more spring-masses and bandgaps borders can be found analytically by calculating the transfer matrix as defined by equation (2.8). For a system with two spring-mass unit cells the analytical border values are given by equations (2.12), (2.13) and (2.14). For the sake of brevity, the corresponding equation development is omitted here.

$$\Omega_{21}=\sqrt{\frac{(K_1+K_2)(M_1+M_2)}{M_1M_2}}\,, \tag{2.12}$$

$$\Omega_{22}=\sqrt{\frac{(K_1+K_2)(M_1+M_2)}{2M_1M_2}-\sqrt{\left(-\frac{(K_1+K_2)(M_1+M_2)}{2M_1M_2}\right)^2-4\frac{K_1K_2}{M_1M_2}}}\,, \tag{2.13}$$

$$\Omega_{23}=\sqrt{\frac{(K_1+K_2)(M_1+M_2)}{2M_1M_2}+\sqrt{\left(-\frac{(K_1+K_2)(M_1+M_2)}{2M_1M_2}\right)^2-4\frac{K_1K_2}{M_1M_2}}}\,. \tag{2.14}$$

Similarly, equations (2.15), (2.16) and (2.17) are the analytical bandgap borders found for a unit cell with one spring-mass and one resonator.

$$\Omega_{r11} = \sqrt{\frac{M_r K_r + M K_r}{M M_r}}\,, \tag{2.15}$$

$$\Omega_{r12} = \sqrt{\frac{4KM_r + K_r M_r + K_r M}{2MM_r} - \sqrt{\left(-\frac{4KM_r + K_r M_r + K_r M}{2MM_r}\right)^2 - 4\frac{KK_r}{MM_r}}}\,, \tag{2.16}$$

$$\Omega_{r13} = \sqrt{\frac{4KM_r + K_r M_r + K_r M}{2MM_r} + \sqrt{\left(-\frac{4KM_r + K_r M_r + K_r M}{2MM_r}\right)^2 - 4\frac{KK_r}{MM_r}}}\,, \tag{2.17}$$

2.2.2 Continuous systems

For continuous rods, non-dispersive longitudinal waves propagate in the structure. A way to create dispersive waves consists in introducing an impedance mismatch by changing geometrical or physical properties. Figure 2.4 shows a stepped rod composed of two different continuous segments with different values of cross section area A_i, Young modulus E_i, density ρ_i and length l_i (i indicating the segment number).

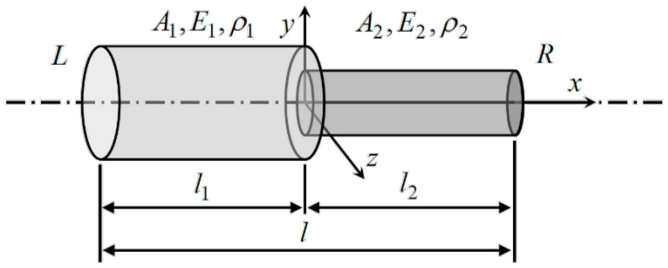

Figure 2.4 Rod unit cell with two continuous dissimilar parts.

Transfer matrix and spectral method approaches (Doyle, 1997; Ruzzene and Scarpa, 2003) are used in this subtopic. Assuming harmonic steady state condition, the classical equation of motion (wave equation) can be written as:

$$E_i A_i \frac{\partial^2 u_i(x_i)}{\partial x_i^2} + \omega^2 \rho_i A_i u(x_i) = 0\,. \tag{2.18}$$

According to (Ruzzene and Scarpa, 2005), equation (2.18) can be rewritten in the form $\frac{\partial \mathbf{y}(x)}{\partial x} = \mathbf{A}(x,\omega)\mathbf{y}(x)$, where $\mathbf{y}(x)$ is the state vector $\mathbf{y}(x) = [u(x) \quad f(x)]^T$ with the normal force $f(x) = EA(x)\partial u(x)/\partial x$ and $\mathbf{A}(x,\omega)$ is given by

$$\mathbf{A}_i(x_i,\omega)=\begin{bmatrix} 0 & \dfrac{1}{E_iA_i} \\ \omega^2\rho_iA_i & 0 \end{bmatrix}. \tag{2.19}$$

It should be noticed that this matrix can be periodic in space $(\mathbf{A}(x+l,\omega)=\mathbf{A}(x,\omega))$ if a periodic infinite structure is considered. Therefore, these differential equations can be solved using the transition matrix, where the boundary condition can be written as $\mathbf{y}(0)=e^{-\mathbf{A}l}\mathbf{y}(l)$. This is equivalent to the solution conducted by using the Floquet-Bloch theorem $(\mathbf{y}(x+l)=\lambda\mathbf{y}(x))$ for $x=0$, and a Transfer Matrix can be deduced as $\mathbf{T}(x,\omega)=e^{\mathbf{A}(x,\omega)l}$.

For a stepped rod, under the hypotheses considered herein, enforcing displacement continuity $u_L^{(i+1)}=u_R^{(i)}$ and force equilibrium $f_L^{(i+1)}=-f_R^{(i)}$ to each interface between adjacent segments, the transfer matrix for each segment can be obtained as $\mathbf{T}_i(\omega)=e^{\mathbf{A}_il_i}$ with $i=1,2$ for two different segments. The relation between the state vectors on the right and on the left can be expressed as $\mathbf{y}_i(x+l_i)=\mathbf{T}_i(\omega)\mathbf{y}_i(x)$ and the eigensolutions of $\mathbf{T}_i(\omega)$ give the propagation constants as mentioned before.

Another methodology to obtain the transfer matrix consists is considering the general solution of the equation of motion $u(k_ix_i)=A\cos(k_ix_i)+B\sin(k_ix_i)$ and its derivative, using the expression of the normal force $f(x)=EA(x)\partial u(x)/\partial x$ to obtain the state vectors on the right $(x_i=l_i)$ and on the left $(x_i=0)$ as expressed by:

$$\begin{Bmatrix} A\cos(k_il_i)+B\sin(k_il_i) \\ -AZ_i\sin(k_il_i)+BZ_i\cos(k_il_i) \end{Bmatrix}^{(x_i=l_i)}=\mathbf{T}_i(\omega)\begin{Bmatrix} A \\ BZ_i \end{Bmatrix}^{(x_i=0)} \tag{2.20}$$

where the Transfer Matrix is

$$\mathbf{T}_i(\omega)=\begin{bmatrix} \cos(k_il_i) & \dfrac{1}{Z_i}\sin(k_il_i) \\ -Z_i\sin(k_il_i) & \cos(k_il_i) \end{bmatrix} \tag{2.21}$$

with wavenumber $k_i=\omega/c_i$, wave speed $c_i=\sqrt{E_i/\rho_i}$ and impedance $Z_i=\omega A_i\sqrt{E_i\rho_i}$.

Compared to the first approach, this approach has the advantage that it facilitates obtaining the analytical values of bandgap borders for unit cells. For example, considering two different segments with different geometrical and physical properties, the Transfer Matrix will be $\mathbf{T}_{12}=\mathbf{T}_1\mathbf{T}_2$ and the following exact solution of a free-free beam can be derived as presented by Graff (1975):

$$\frac{E_2A_2k_2}{E_1A_1k_1}\cos k_1l_1\sin k_2l_2+\cos k_2l_2\sin k_1l_1=0\,. \tag{2.22}$$

Figure 2.5 shows the dispersion constants and frequency response functions obtained by calculating the eigenvalues of $\mathbf{T}_{12}(\omega)$ and using the equation (2.10) to find the correspondent dynamic flexibility matrix $\mathbf{D}(\omega)$, for a rod unit cell comprising two segments with the same material ($E_1 = E_2$ and $\rho_1 = \rho_2$), same segment length ($l_1 = l_2$) and different cross-section areas ($A_1 = 3A_2$). The same results are obtained using both approaches.

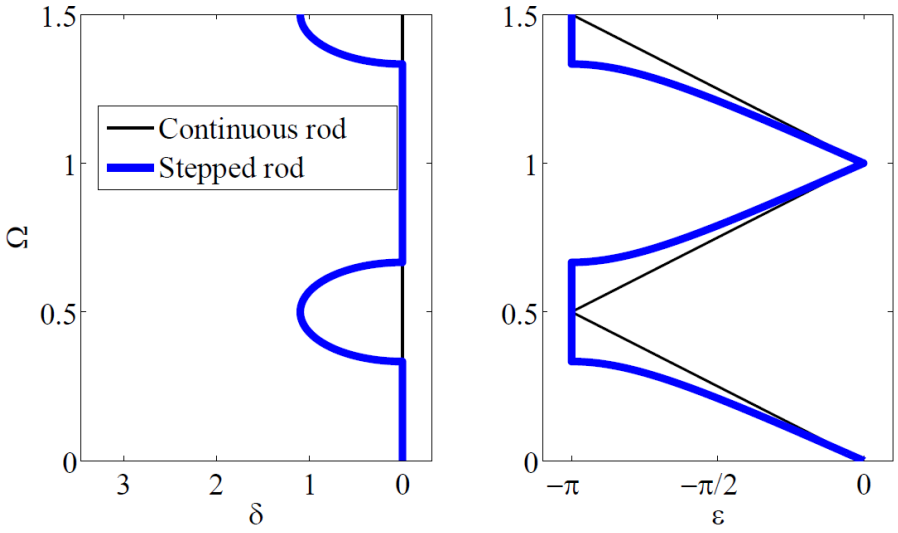

Figure 2.5 Dispersion diagram for a contrinuous rod and for a stepped rod.

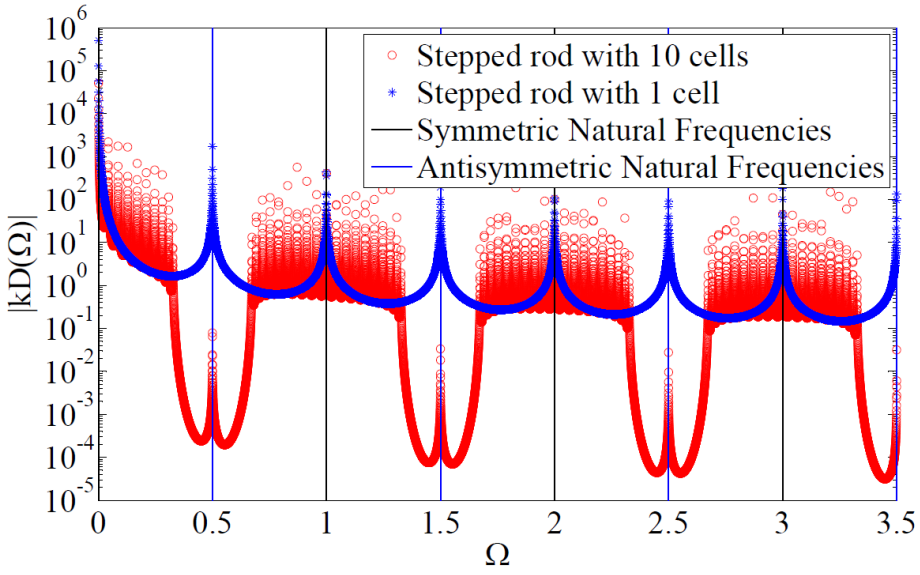

Figure 2.6 Frequency response functions for a free-free periodic stepped rod finite structure with 10 cells, one cell and its exact natural frequencies for symmetric and antisymmetric modes.

The frequency response function in Figure 2.6 is represented in terms of dimensionless units $\Omega = \omega/\omega_2$ and $|kD(\Omega)| = |kD_{21}(\Omega)|$ with $k = EA_1/l$ and subscripts representing excitation on the left (1) and

response on the rigth (2). The value ω_2 is calculated using equation (2.22) and it is the first nonzero symmetric natural frequency of the free-free unit cell.

The circles and the asterisks in Figure 2.6 represent, respectively, the frequency response functions of a finite structure composed of 10 cells and 1 cell. The blue and black lines represent the symmetric and anti-symmetric modes of the free-free unit cell found using equation (2.22) and described by Graff (1975). As they perfectly coincide with specific frequency response peaks, the method is validated as an exact solution for this case. In addition, Figure 2.6 shows some interesting aspects related to symmetric and anti-symmetric modes. Firstly, there is a concentration and absence of energy around the cell symmetric and anti-symmetric modes, respectively. It is possible to observe on these *FRFs* that as the number of cells increases, the number of natural frequencies inside the propagation zone also increases. The response magnitude inside bandgaps reduces while it increases in the propagation zones. Succinctly, there is an energy redistribution along the spectrum.

Another interesting point is that there is also a natural frequency inside the attenuation zone and it disappears as the number of cells is increased. This phenomenon is explained in the following topics.

Analytical expression of bandgap borders can be found with the same methodology presented previously. Equation (2.23) gives all bandgap frequency borders for a periodic arrangement of two continuous rod segments having a same material and different cross-section areas.

$$\omega = \frac{1}{L}\sqrt{\frac{E}{\rho}}\left(\pm a\sin\left(\frac{2\sqrt{A_1 A_2}}{A_1 + A_2}\right) + \pi(k-1)\right) \tag{2.23}$$

where, k is the $k-th$ propagation zone. For different materials, with different wave speeds and different segment lengths, a transcendental equation is found.

As observed in the presented results, the attenuation zone needs a minimum quantity of unit cells to be effective. It is proposed here to analyze the effect of the number of cells in finite structures on the depth of the band gap.

Figure 2.7 shows the frequency response functions of a periodic structure modeled by using the Transfer Matrix method with 4, 10 and 16 cells. It shows that 10 cells are sufficient to detect the attenuation zone with well-defined borders in the frequency response. Besides, for the finite structure with 4 cells, the fifth natural frequency is located inside the first bandgap. Similarly, for 10 and 16 cells, as the number of cells *n* increases, the $m-th$ natural frequency is found inside the $i-th$, with $m = 1 + n(2i-1)$.

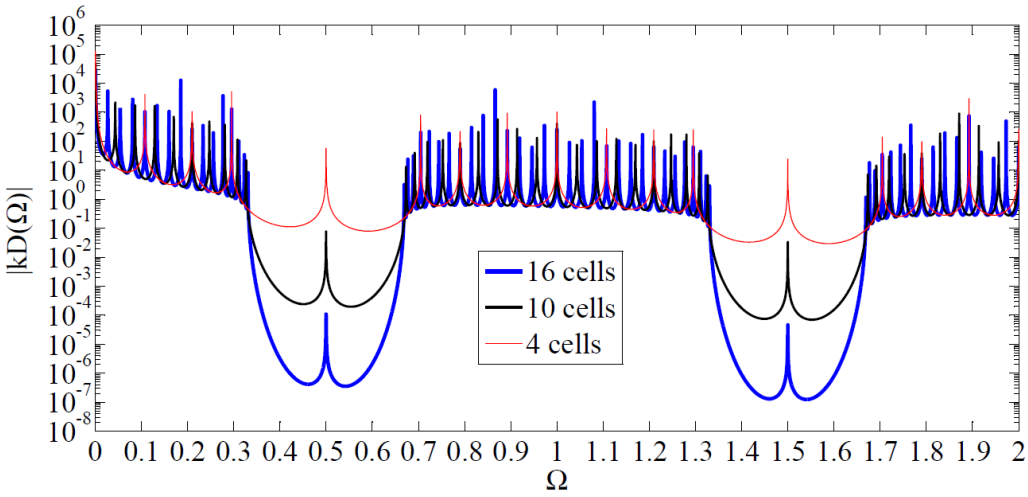

Figure 2.7 Frequency response functions for finite strucutres with various cell number.

2.3 Parametric and Sensitivity Analysis

A sensitivity analysis is performed with partial derivatives for spring-mass unit cell and with finite differences for stepped rod unit cell using an infinite model and its parametric study involving dispersion constants. This analysis can be employed to determine the influence of input parameters in the selected output responses.

2.3.1 Spring-mass models

Cases 2 and 4 of tables 2.1 and 2.2 are used in this section. The partial derivatives of equations (2.12) to (2.17) can be obtained analytically using the following definition

$$\frac{\partial \omega(X_i)}{\partial X_i} = \lim_{\Delta \to 0} \frac{\omega(X_i + \Delta) - \omega(X_i)}{\Delta} \tag{2.24}$$

The development of these derivatives is a cumbersome operation. Therefore, a symbolic calculation was performed to facilitate this task. However, these steps are omitted here.

Using equations (2.12), (2.13) and (2.14) and their derivatives, a parametric variation of variables K_1, M_1, K_2 and M_2 is performed. The bandgap envelopes and the analytical derivative of borders for case 2 of Table 2.1 are presented in Figure 2.8. The natural frequency inside the attenuation zone can be calculated according to

$$\omega_R = \sqrt{\frac{K_1(M_1+M_2)}{M_1 M_2}}\,. \tag{2.25}$$

This equation is obtained by calculating $det\left(\mathbf{D}^{-1}(\omega)\right)=0$. This frequency is important to know because it can change the value of bandgap border for a finite structure if its value is inside the bandgap region and near to stop band bound. This fact can be observed in Figure 2.8, in which it can also be noticed that increasing mass and stiffness values shift the bandgap region to lower and higher frequencies, respectively. When the mass values are the same, the bandgap in lower frequencies disappear.

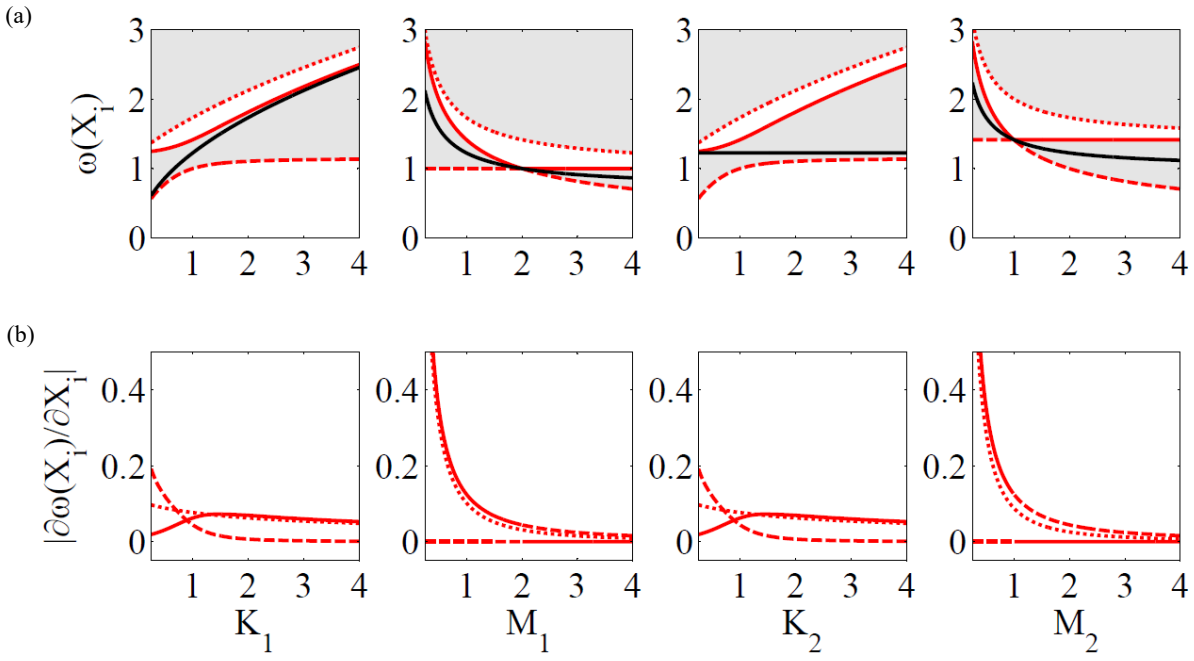

Figure 2.8 (a) Parametric variation of unit cell parameters on abscissa and frequency on ordinate for band gap envelopes ( ), natural frequency inside attenuation zone ( ), band gap borders 1 ( ), 2 ( ) and 3 ( ) and (b) their corresponding analytical derivatives for case 2.

Derivatives of analytical equations with closed form solutions of equations (2.15), (2.16) and (2.17) can also be calculated. Figure 2.9 shows the parametric variation of variables K_l, M_l, K_r and M_r for case 4 of Table 2.2.

It possible to observe in Figure 2.9 that the natural frequency calculated for one cell is the upper bound of first bandgap in this situation. It can be calculated using equation (2.15). The position of anti-resonances can also change the value of a bandgap border in a finite model. Its value is the resonance of the attached internal resonator.

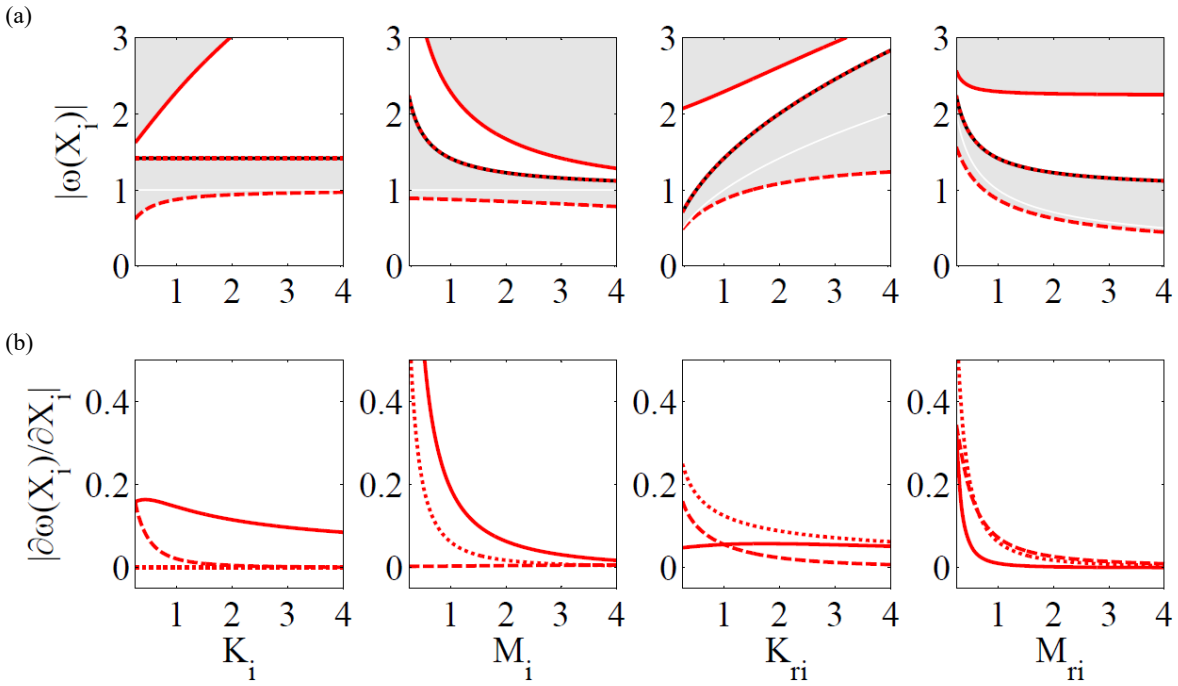

Figure 2.9 (a) Parametric variation of unit cell parameters on abscissa and frequency on ordinate for band gap envelopes ( ), anti-resonance inside attenuation zone ( ) and natural frequency ( ); band gap borders 1 ( ), 2 ( ) and 3 ( ) and (b) their corresponding analytical derivatives for case 5.

2.3.2 Continuous models

Using the example consisting of two continuous rod segments made of a same material and having different cross section areas, the derivative of equation (2.23) can be expressed analytically as follows

$$\left|\frac{\partial\omega(A_i,A_j)}{\partial A_i}\right| = \frac{1}{L}\sqrt{\frac{E}{\rho}}\left(\frac{\sqrt{A_iA_j}}{A_i(A_i+A_j)}\right). \tag{2.26}$$

It should be mentioned that if different material were considered for the segments, only transcendental equations could be obtained. In this case, numerical methods would have to be used to obtain the local sensitivity of bandgap borders.

In this section, the influence of unit cell properties as cross-sectional area, Young's modulus and density are taken into account to analyze the bandgap lower bound ($_{LB}$), bandgap upper bound ($_{UB}$) and bandgap width ($_{W}$). The following variables are defined as outputs:

$$q_1(x_j) = \Omega_{UB}(x_j), \tag{2.27}$$

$$q_2(x_j) = \Omega_{LB}(x_j), \tag{2.28}$$

$$q_3(x_j) = \Omega_W(x_j) = \Omega_{UB}(x_j) - \Omega_{LB}(x_j), \tag{2.29}$$

where $\Omega(x_j)$ means the normalized output to the corresponding input x_j. For example, if x_j is the density, ω_1 varies for each value of ρ and it must be normalized at each increment of input variable. In these circumstances, the local sensitivity for each border *i* according to the finite difference method is expressed as:

$$\Phi_i(\bar{x}_j) = \frac{q_i(\bar{x}_j) - q_i(\bar{x}_j - \Delta\bar{x}_j)}{\Delta\bar{x}_j} = \frac{\Omega_{UB}(\bar{x}_j) - \Omega_{UB}(\bar{x}_j - \Delta\bar{x}_j)}{\Delta\bar{x}_j} \text{ for i = 1,} \tag{2.30}$$

with Φ_i the requested output sensitivity and $\Delta\bar{x}_j$ the spacing parameter normalized with respect to ω_1. In this study, only the local sensitivity is calculated. In other words, only one variable change is considered, the two other variables are kept constant. This approach does not consider dependency between input variables, but there are some sensitivity techniques that deal with it. Saltelli *et al.* (2000), Ouisse *et al.* (2012) and Christen *et al.* (2016) show more details about these procedures.

In Figure 2.10, the input parameters A_1, E_1 and ρ_1, denoted by x_j, are the properties of first half of the unit cell. They are varied from 30% to 300% and the regions filled with solid colors represent the first stop band. When the input variable is equal to 100%, the structure is not periodic and, therefore, the upper and lower limits have the same values and the frequency bandgap width is zero.

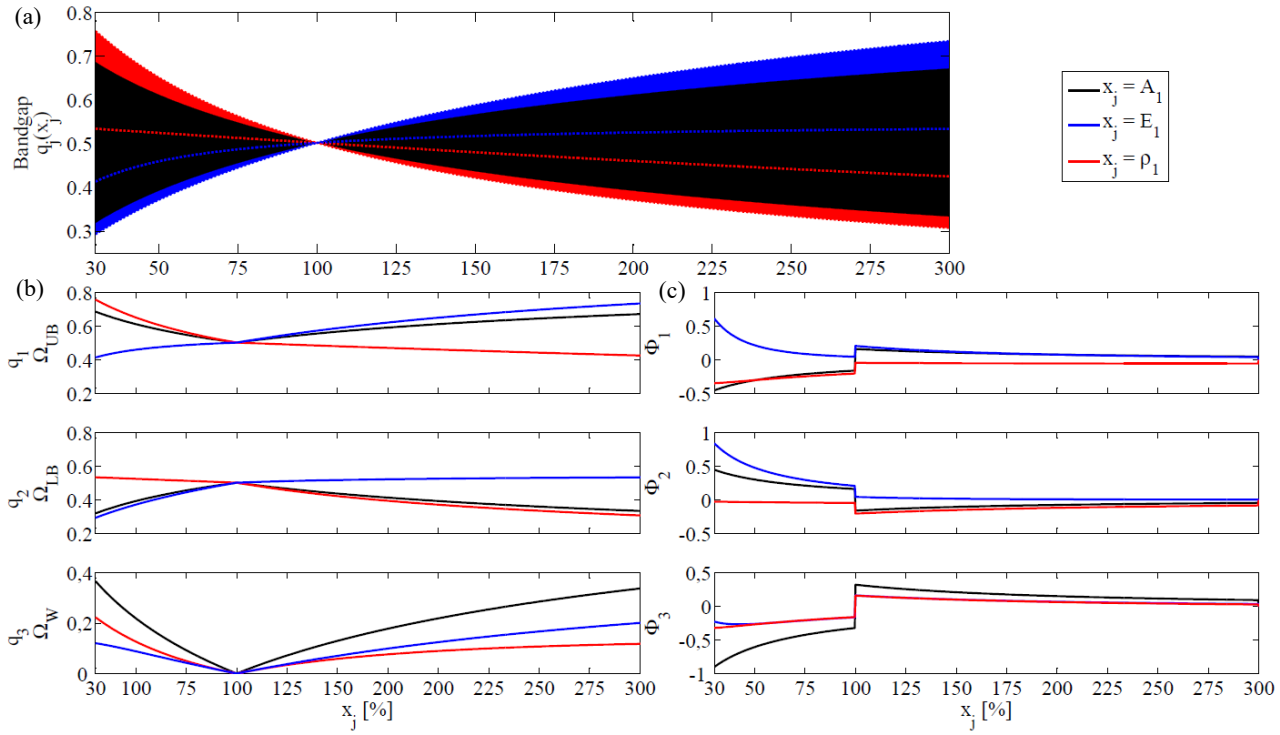

Figure 2.10 (a) Bandgap envelopes, (b) bandgap borders and width; (c) their respective numerical derivatives.

Figure 2.10(a) presents the bandgap created by varying each input parameter, while Figure 2.10(b) provides the lower and upper limit dimensionless frequencies, and Figure 2.10(c) shows the corresponding numerical derivatives.

It can be noticed that when the density is increased, the bandgap moves to lower frequencies. Oppositely, when the Young's modulus increases, the bandgap moves to higher frequencies. If these values cross the non-dispersive configuration values (x_j equals to 100%), the upper bound frequency turns to lower bound frequency and this creates a discontinuity in the corresponding Φ_i curve.

The bandgap created by varying the cross section area on Figure 2.10(a) is larger than the others and it is symmetric with respect to the dimensionless frequency equal to 0.5. Concerning the bounds, Young's modulus and density are the most influential parameters, depending whether the parameter is higher or lower than 100%. For $x_j < 100$ %, density is the most influential for upper bound and Young's modulus is the most influential for lower bound. For $x_j > 100$ %, the behavior is the opposite. The cross-section area is the second most influential variable in both cases.

It is possible to observe that the width of the attenuation zone is more sensitive to variations in cross section area than in the Young's modulus and density in both conditions.

Given that the cross section area is the most influential parameter for bandgap width and it is the second most influential parameter for bandgap borders before and after the 100% point, it seems suitable to be considered as an uncertain variable in uncertainty propagation analyses.

Inasmuch as this sensitivity analysis considers an infinite structure, the verisimilitude of considering different values for each cell of a complete structure is not verified. To deal with this problem, Monte Carlo Simulation can be used, as described in the next section.

2.4 Uncertainty propagation using Monte Carlo Simulation

Monte Carlo Simulation (MCS) is a method that consists in sampling input random variables, defined by probability density functions, to obtain the corresponding outputs samples (Haldar and Mahadevan, 2000; Lemaire, 2009; Melchers, 1987). However, it is widely recognized that the main disadvantage of MCS is that, for achieving statistical significance, a large number of samples is required. This convergence is characterized by the stabilization of mean and standard deviation of the output variables. For problems featuring random variables with low dispersions, very large numbers of samples are necessary.

According to Melchers (1987), the estimation error can be evaluated in function of the number of simulations and the confidence interval for a normal probability density function. Optimized sampling methods can be used to reduce the computation effort necessary for MCS convergence. In this work, the technique

referred to as Latin Hypercube Sampling (LHS) was used. More details about this sampling technique can be found in (Choi *et al.*, 2007).

Specific probability density functions must be chosen to represent the stochastic variables, accounting for their specific characteristics. In this work, normal (Gaussian) distributions are used. A numerical example using a stepped rod is presented in the following.

2.4.1 Uncertainty propagation for a two-segment continuous rod

In practice, due to manufacturing inaccuracies, it is not possible to obtain a perfect modulation of the inertia and the stiffness of a mechanical structure. Normally, properties such as Young's modulus and density do not vary considerably if the material comes from a same batch. Therefore, the main source of uncertainties are the imperfections or defects caused by the manufacturing process. Moreover, the cross section area is the most influential parameter as related to the bandgap width, as shown in Figure 2.10. Under these circumstances, the cross section areas $A_1 = 3A$, $A_2 = A$ were chosen as stochastic input variables for the numerical example considered in this section.

The variables of each cell are assumed to be independent from each other. In the following, infinite and finite models are used in the probabilistic analyses, and results are compared. To perform this investigation, based on the standard deviation of each input variable, the convergence of Monte Carlo Simulation is verified.

Figure 2.11 shows that a 10-cell model is satisfactory for identifying the attenuation zone on finite structure. In this calculation, the band gap edges corresponding to lower bound ($_{LB}$), upper bound ($_{UB}$) and width ($_{W}$) are the outputs as indicated in equations (2.27) to (2.29). Figures 2.11(a) and 2.11(b) show an illustration of these variables where the red dots are the *LB* and *UB* for a finite (*FS*) and an infinite structure (*IS*), respectively.

The random variables are represented by normal probability density functions. Two variants of uncertainty distribution are considered:

- Type 1: a single numerical sample of the random variable (RV) is applied to all the 10 cells. Consequently, the structure remains periodic;

- Type 2: 10 different samples of the random variable (RV) are applied, one in each of the 10 cells. In this case, the structure is not perfectly periodic, meaning quasi-periodicity.

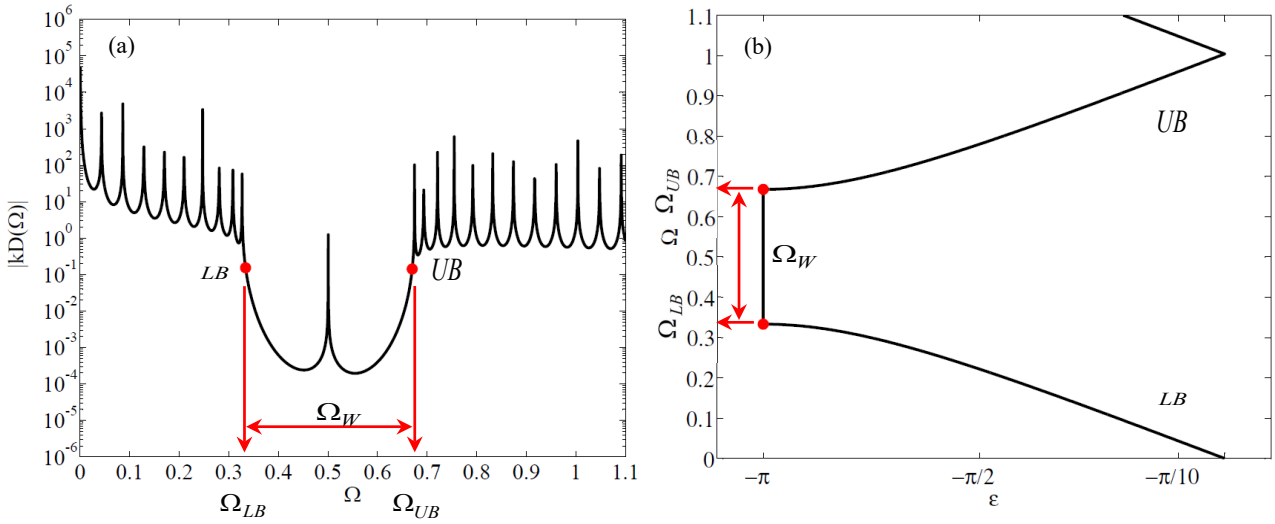

Figure 2.11 Bandgap borders for: (a) finite model and (b) infinite model.

For both cases, infinite and finite models are constructed using the Transfer Matrix exact model. The level of uncertainty is controlled with variation coefficient γ, that relates the standard deviation σ and the mean value μ as follows:

$$\sigma = \gamma \times \mu \,. \tag{2.31}$$

In the simulations, this parameter is varied from 2 % to 16 %, with a step of 2 %. Then, for each value considered, a Monte Carlo Simulation with Latin Hypercube is performed until convergence (number of samples around 5000).

The confidence interval for the outputs with normal distribution is defined as $\left[\mu_{q_i} - k\sigma_{q_i}; \mu_{q_i} + k\sigma_{q_i}\right]$. For a 95% confidence level, the value of *k* must be equal to 1.96. This means that the probability of the mean of the output variables to be within this interval is 95%.

Figure 2.12(a) shows the mean and 95% confidence limits of the bandgap lower and upper frequency for three situations: 1) infinite periodic structure with uncertainty of Type 1. In this case, the structure is strictly periodic, but stochastic; 2) finite periodic structure with uncertainty of Type 1. Also in this case, the structure is strictly periodic, but stochastic; 3) finite periodic with uncertainty of Type 2. In this case, one has a quasi-periodic structure. Similarly, Figure 2.12(b) shows the results in terms of bandgap width.

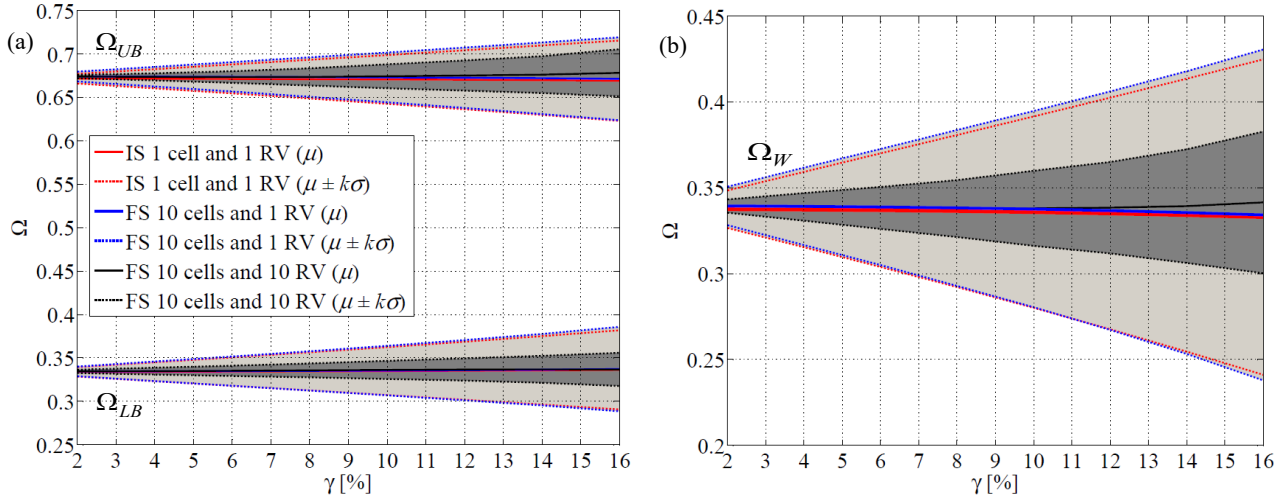

Figure 2.12 (a) Bandgap borders' and (b) width's mean and confidence intervals for infinite structure (IS) with 1 random variable (RV) and for finite structures (FS) with 1 and 10 random variables.

In Figure 2.12(a), it is possible to observe that the edges of the bandgap vary almost linearly according to the increase of the uncertainty level. For uncertainty of Type 1, for every 1% of uncertainty level, the dimensionless limits of the attenuation zone vary nearly ±0.035. For uncertainty of Type 2, these bounds vary around ±0.013. The behavior of the bandgap width is similar, but the ratio of the variations observed for the two types of uncertainty is approximately 2.

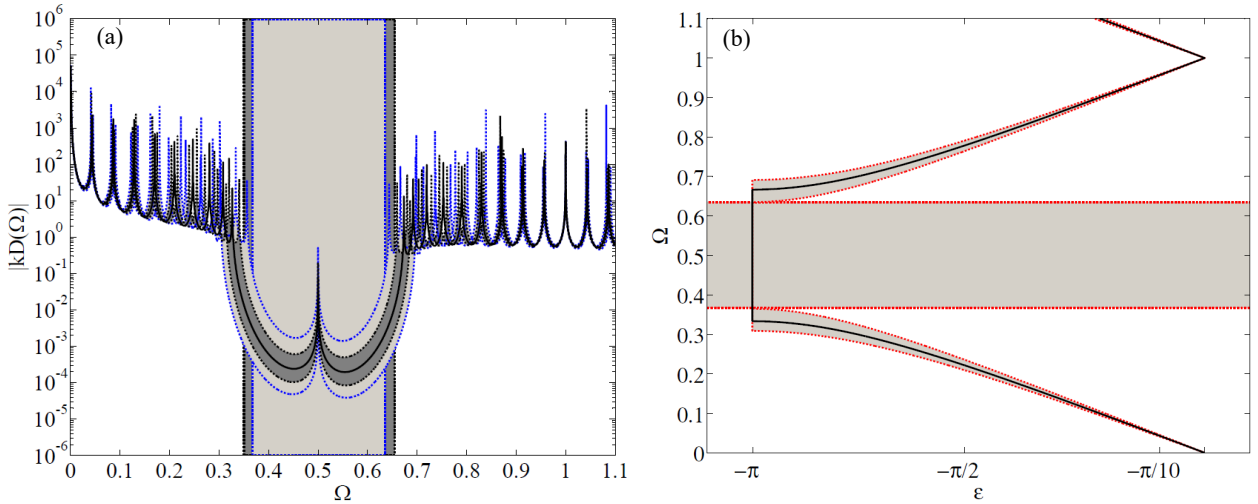

Figure 2.13 Robust bandgaps for rod example considering (a) finite structure and (b) infinite structure.

Assuming an uncertainty level of 10 %, for the cross-sectional area, the robust bandgap (bandgap almost certain considering these geometrical uncertainties) will be the light and dark gray areas considered in Figures 2.13(a) and 2.13(b) for finite and infinite models, respectively.

The light gray areas in Figures 2.13(a) and 2.13(b) indicate the robust attenuation zone calculated with a single random variable. They are obtained using the light gray confidence interval with the uncertainty parameter equals to 10 % on Figure 2.12. The dark gray areas in Figure 2.13(a) are obtained in the same way but considering 10 random variables for a finite structure. The light gray ones, contrarily to the envelopes representation where the light gray envelopes are larger, superpose these areas. Therefore, when one different random variable is considered for each cell of a finite structure, which corresponds to the quasi-real case, the robust bandgap is larger and it can be explained by a compensation effect on the responses. In other words, the probabilistic analysis with 10 random variables, which better represents the real situation, shows that the finite structure is intrinsically more robust.

2.4.2 Robust Bandgap and Localization phenomena

The envelopes in Figure 2.13(a) does not take into account the localization phenomena on the borders. It consider a magnitude threshold on FRFs of finite model to detect the bandgap borders. Consequently, a natural frequency can appear inside the attenuation zone without being detected.

The natural frequency that appears inside the attenuation zone is known as localized mode and this is referred to in literature as localization phenomena (Anderson, 1958). It is a confined mode in a specific place of the structure, in this case, at the right end. As the number of cells tends to infinity, the participation of this mode tends to diminish and this mode can be neglected. Consequently, it does not appear in the infinite model.

Some experimental results can be found in (Junyi *et al.*, 2016) for a localized mode near a clamped boundary condition. It is explained by the fact that the last unit cell that has a different boundary condition. It causes a distinct wave interaction, because of different impedance mismatch, and the localization phenomenon appears.

In the case of the structure studied herein, the fact that the last segment is different from the first induces a strong asymmetry, and this causes mode localization. To demonstrate this phenomenon, Figure 2.14(a) shows a nominal antisymmetric structure and its symmetric counterpart. Figure 2.14(b) shows the mode localization in frequency response and Figure 2.14(c) depicts the corresponding normalized deformed shape.

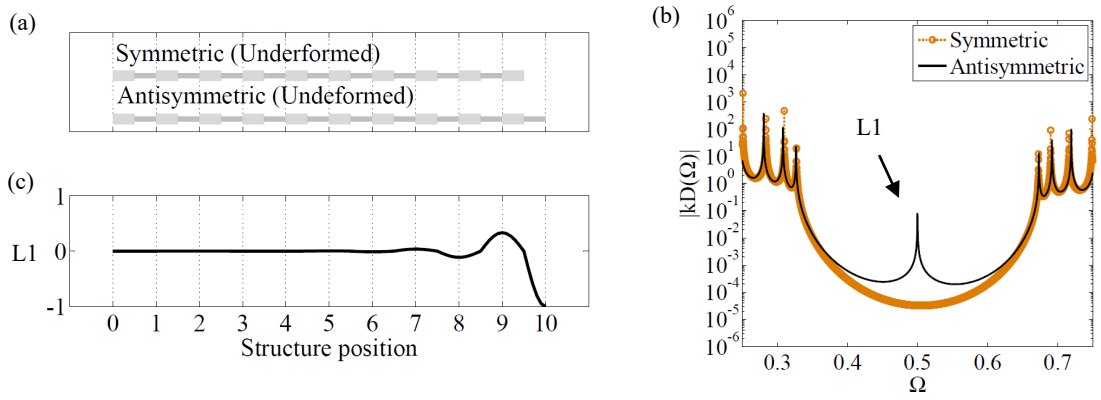

Figure 2.14 Comparison between (a) symmetrical and antisymmetrical structures, their (b) FRFs and (c) the shape of localized mode L1 for antisymmetrical one.

As it can be seen, the attenuation zone boundaries are the same for both symmetric and antisymmetric structures, whereas mode localization, with high amplitudes, occurs within the bandgap for the antisymmetric rod. Therefore, this phenomenon can produce incorrect confidence interval envelopes in Monte Carlo Simulations for a finite structure. If the deviation of a random variable of any cell of a finite structure is considerably different from the others, this peculiarity appears.

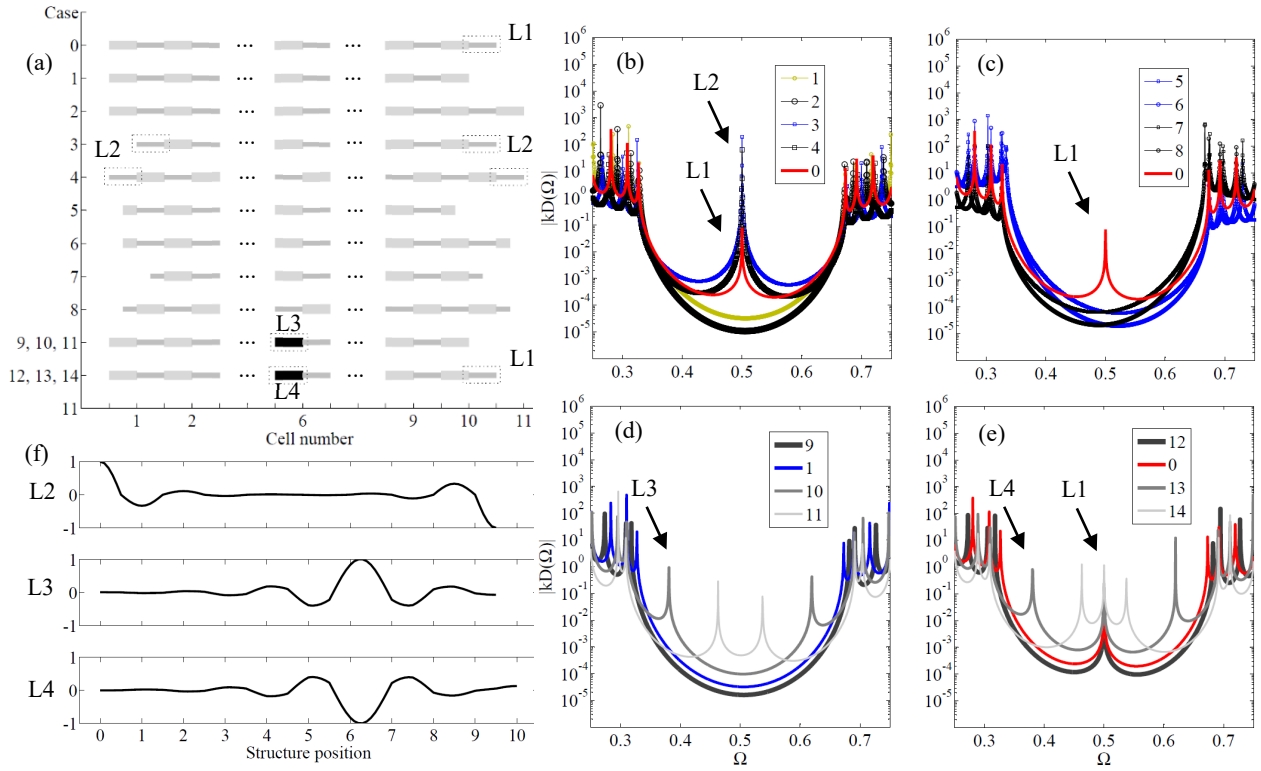

Figure 2.15 (a) 14 different structures cases and their corresponding FRFs for (b) cases 0, 1, 2, 3 and 4; (c) 0, 5, 6, 7 and 8; (d) 1, 9, 10 and 11; (e) 0, 12, 13 and 14; and (f) the shape of localized modes L2, L3 and L4.

Figure 2.15(a) shows some variations of the nominal structure studied to explain the localization phenomena. Case 0 represents the nominal finite structure. As the unit cell is asymmetric, the complete structure is also asymmetric. Cases 1 and 2 are symmetric variants of case 0, without the last half-cell and with half part of next one, respectively. Cases 3 and 4 are their opposites by permuting their half-cells. Similarly, cases 5, 6, 7 and 8 are their correspondents with one quarter first and last cells. Moreover, cases 9, 10, 11 and 12, 13, 14 are the variation of cases 0 and 1 by strongly and gradually changing cross section area value A_1 of the sixth cell.

Figures 2.15(b) to 2.15(e) show the natural frequencies that appear inside the bandgaps for each case. The symbol Li indicates the *i*-th localization phenomenon, whose corresponding normalized mode shapes are depicted in Figure 2.15(f). Li symbol also appears in Figure 2.15(a) to indicate where the localized mode is spatially located.

By observing Figure 2.15(a) and their FRFs, it is possible to see that where there is a strong impedance mismatch, different from nominal repetitive structures, there is also a localized mode. As the number of cells increases, the displacement decreases in magnitude and it becomes concentrated where the strong deviation takes place. In spite of having low amplitudes inside the band gap, the FRF attenuation zones are sensible and it can describe where it shows up.

In Figure 2.15(c), it is possible to observe that unit cell structures, which differs from nominal one, placed on the left or on the right side of finite structure can slightly shift the attenuation zone to the right (cases 5 and 6) or to the left (cases 7 and 8) in frequency response. Considering cases 5 and 6, these finite structures also has the amplitude of left side of bandgap increased and the amplituce of right side decreased. The opposite is observed for cases 7 and 8.

Figures 2.15(d) and 2.15(e) show that gradually increasing the cross-section area of sixth unit cell imply shifts of the localized modes from the bandgap borders to its center. In this situation, if the impedance mismatch is stronger than other cells, its localized mode frequency is placed in the middle of the attenuation zone. In spite of the presence of these localized modes, it is possible to observe that the bandgap width with localized modes is larger than the attenuation zone of nominal cases for symmetric and asymmetric structures. This can be confirmed by comparing the bandgap borders of light and dark gray FRF curves with corresponding blue and red curves. The attenuation zone has its attenuation reduced and its width increased.

These phenomena can be considered as beneficial as long as it reduces the variation of bandgap borders. In other words, this kind event can add robustness to the bandgap behavior in terms of variation of its borders. However, a robust interval confidence envelope will not take into account the localization phenomena since the worst configuration may take part in any cell in a random analysis. In addition, for high uncertainty paramenter values, the chances of appearing this situation is higher.

If these localized natural frequencies are present in a structure with low number of unit cells, their magnitude can affect the attenuation inside the stop band and it can be considered as a drawback. The same behaviour can be observed in longitudinal waves in spring-mass systems.

2.5 Partial conclusion

Two simple models describing longitudinal wave propagation in periodic structure were investigated in this chapter.

For the first one, a Transfer Matrix method was used to represent the dynamic behavior of a general spring-mass unit cell. The purpose was to observe the influential parameters in two kind of attenuation zones, Bragg's and local resonance bandgaps, and their particularities.

It was observed that analyzing the frequency response of one cell, one localized mode can be predicted if there is a peak inside the attenuation zone. For a resonance bandgap, this frequency is a bandgap border. For a Bragg's bandgap, this peak can be wrongly defined as an attenuation zone border.

For the second model, an exact solution using Transfer Matrix method was used to represent a continuous rod. Pursuing, a Transfer Matrix method was used to find an exact solution for a rod composed by two different continuous rods. Solutions for finite and infinite structures were found, as well as their frequency response and dispersion diagrams. A spectral approach was used for the finite model in frequency domain.

A number of cells equals to ten has been selected for both finite structures. This choice was made in order to obtain credible location of the first attenuation frequency zone without substantially increasing the computational cost.

A local sensitivity analysis was performed using finite differences. The cross-sectional area was found, in general, as the most influential input on the characteristics of the first band gap for this simple model.

An uncertainty analysis was performed using the finite and infinite models of the structure. The cross-sectional area was purposely chosen as a random variable with a Gaussian probability density function owning a mean and standard deviation as stochastic properties. Although the area value may achieve negative values for this model, an extremely high value of standard deviation is necessary to produces negative values.

A coefficient of variation was specified to vary the standard deviation as a percentage of the mean value. Numerous Monte Carlo Simulations with Latin Hypercube Sampling were conducted until their convergences for each value of the coefficient mentioned before.

The results for finite and infinite models with a single stochastic variable are slightly different. These results are not completely reliable since the same uncertainty is repeated indefinitely for the infinite structure and ten times for the finite structure with ten cells.

The confidence intervals for the complete structure with ten stochastic variables are narrower than those found with one random variable. Besides, they are more reliable due to the model being closer to reality for the same case. The fact of considering ten random variables, instead of one, illustrates that the uncertainties self-compensate and the periodic structures are intrinsically robust. In this case, a more accurate and reliable robust bandgap was obtained.

Another type of localization phenomenon was identified related to symmetry and asymmetry of the unit cell. This important remark was clarified with examples of finite structures and explains the influence of uncertainties in this kind of repetitive structure.

The other type of localization phenomenon is caused by a strong impedance mismatch, which highly differs from the other cells, in some place of the structure. It can reveal interesting properties for structural design such as damage detection. The localized modes can be advantageous for a structure with numerous unit cells since a defect shifts a mode inside the attenuation zone but it does not change its borders. However, they can be a drawback for a structure with low number of unit cells since this mode can be misinterpreted as a bandgap border.

A procedure to detect a priori all these localized modes, caused by unit cell asymmetry or strong impedance mismatch can help better understanding the behaviour of a studied periodic structure. Therefore, the analysis of a unit cell as finite structure must be done considering several boundary conditions to search for localized modes, which should be detected and accounted for in a probabilistic analysis.

This page intentionally left blank

Chapter 3 Flexural waves

3.1 Introduction

A flexural propagating wave in a beam is dispersive, *i.e.*, the group velocity of this kind of wave is not constant and, consequently, this velocity increases in higher frequencies. Completely different wave behaviors are observed comparing flexural and longitudinal waves. These can propagate together in the same structure, such as a truss, and some remarks of these two types of waves are important to be mentioned. In general, longitudinal waves are faster than flexural waves; Bragg's longitudinal bandgaps are normally in higher frequencies than flexural bandgaps; the second type is more dependent on geometrical properties than the first one. The geometry of cross section defines the second moment of area, which is associated to bending stiffness, and inertia effects. As long as more variables are required to be defined, this peculiar type of wave is also more susceptible to uncertainties.

Several researchers have already used exact models of periodic beams without changing cross section area and using specific boundary conditions. Examples of multi-supported beams are reported for aeronautic structures called skin-stringers (Lin and Yang, 1974; Mead; 1970) in which transversal displacement is blocked and rotation is allowed. In this case, a mono-coupled uniform beam has the rotation *dof* on supports coupled to the corresponding *dof* of neighbor cells (Lin and McDaniel, 1969; Sen Gupta, 1971; Mead and Bansal, 1978a, 1978b; Orris and Petyt, 1974). The article of Bouzit and Pierre (1993) shows an experimental investigation of vibration localization in this kind of structure. For periodic free-free beams, exact analyses of finite structures are scarce in literature. Usually, finite element models are used to represent the behavior of this finite structure. However, a fine mesh is needed for accurate results and, consequently, the computational cost rises, mainly when the number of cells is large.

Thin and long beams, whose sectional inertia and shear effects can be neglected, can be modeled with Euler-Bernoulli theory. The influence of these parameters can be verified a priori by adopting acceptable values of slenderness coefficient. Otherwise, a Timoshenko beam model must be used because these neglected effects becomes important and the Euler-Bernouilli models become less accurate when the frequency increases.

Keeping the idea of "exact model" and looking for analytical exact solutions, the use of continuum models remains a good option compared to bar models analyzed in the previous chapter. The Transfer Matrix method has been applied successfully in many cases (Lin and McDaniel, 1969; Yong and Lin, 1989; Yong

and Lin, 1990; Ruzzene and Baz, 2000; Thorp *et al*, 2001; Ruzzene and Scarpa, 2003) and one of its powerful properties is that it can be applied for both infinite and finite structures. It has also been proved to be fast and exact from a mathematical point of view. However, the Transfer Matrix method can present instability problems (Lin and McDaniel, 1969; Dazel *et al.*, 2013), especially when the size of the matrices involved increases. This inconvenience can be explained by the presence of ill-conditioned transfer matrices. According to (Dazel *et al.*, 2013), the reason of this divergence is a bad numerical evaluation of the involved exponential terms by finite-arithmetic computers. Exponentially growing terms make the results diverge with the minimal presence of errors.

Following this idea, in this chapter, a method that explores the reduction of matrices multiplications and inverse calculation is used for parametric and probabilistic analyses.

Firstly, a continuous Euler-Bernoulli beam transfer matrix is considered. The Transfer Matrix method is used to exemplify a divergence problem. A method termed as Translation Matrix method, based on (Dazel *et al.*, 2013) and other recursive methods, is presented and used. The general idea consists in not propagating the whole state vector but only non-redundant information. The most important characteristic of this method is that it can be considered mathematically equivalent to the traditional Transfer Matrix method and can thereby be considered as exact. A finite element method is used to validate this method by comparing the frequency response functions with gradually refining the mesh. Subsequently, for a numerical example, an asymmetric periodic beam unit cell is used for a parametric study with different geometrical properties focusing on Bragg's bandgap.

Infinite structures models do not represent the effect of dissimilarities between cells. In reality, these cells are not perfect. To verify the effects of uncertainties on infinity and finite structures, a probabilistic analysis using Monte Carlo Simulation with Latin Hypercube (Melchers, 1999; Haldar and Mahadevan, 2000; Lemaire, 2009) is performed and a robust bandgap is obtained.

The localization phenomena (Anderson, 1958) is inspected with different symmetric unit cells and their FRFs are used to observe peaks inside the attenuation zone (Hvatov and Sorokin, 2015). The flexural bandgaps are compared to longitudinal ones investigated in the previous chapter. At the end, a localization phenomenon is created in a finite periodic beam structure by removing an impedance mismatch and damping is added in this "imperfect cell" (Langley, 1994; Bouzit, 1995; Collet *et al.*, 2012).

3.2 Flexural waves in Euler-Bernoulli beams

Figure 3.1 shows a representation of a unit cell with rectangular cross-section that is used to characterize the propagation of flexural waves. In this case, an asymmetrical unit cell is investigated.

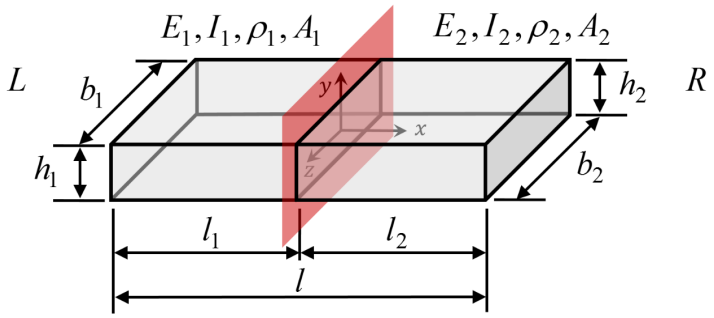

Figure 3.1 Representation of two continuous parts unit cell for a periodic beam structure.

The classical equation governing free motion of Euler-Bernoulli beams is (Graff, 1975):

$$\frac{\partial^2}{\partial x^2}\left(E_i I_i \frac{\partial^2 u_i(x)}{\partial x_i^2}\right) = -\rho_i A_i \frac{\partial^2 u_i(x)}{\partial t^2} \tag{3.1}$$

where u is the deflection y direction, E_i is the Young's modulus, I_i is the second moment of area, ρ_i is the mass density and A_i is the cross-section area of segment i. The slope θ_i, the bending moment M_i and the shear force V_i are expressed as

$$\theta_i(x) = \frac{\partial u_i(x)}{\partial x}, \quad -\frac{M_i(x)}{E_i I_i} = \frac{\partial^2 u_i(x)}{dx^2} \quad \text{and} \quad -\frac{V_i(x)}{E_i I_i} = \frac{\partial^3 u_i(x)}{dx^3}. \tag{3.2}$$

The general solution of equation (3.1) is

$$u_i(x) = A_1^{(i)} \cosh(\beta_i x) + A_2^{(i)} \sinh(\beta_i x) + A_3^{(i)} \cos(\beta_i x) + A_4^{(i)} \sin(\beta_i x) \text{ with i =1, 2} \tag{3.3}$$

for both parts of the beam (see Figure (3.1)). Constants $A_1^{(i)}$, $A_2^{(i)}$, $A_3^{(i)}$ and $A_4^{(i)}$ are determined by enforcing boundary conditions, and the wave number is found to be defined as:

$$\beta_i = \left(\frac{\rho_i A_i \omega^2}{E_i I_i} \right)^{\frac{1}{4}}. \tag{3.4}$$

For a beam having two segments with same physical and geometrical properties, the solutions can be found and the natural frequencies can be expressed as:

$$\omega_n = \frac{(\beta_n l)^2}{l^2} \sqrt{\frac{EI}{\rho A}} = (\beta_n l)^2 \sqrt{\frac{EI}{\rho A l^4}}. \tag{3.5}$$

where $\beta_n l$ is a value obtained by solving transcendental equations depending on boundary conditions and $l = l_1 + l_2$ is the total beam length. For two specific cases, the beam model can have the same frequency equation as a rod: pinned-pinned beam (simply supported) and sliding-sliding beam. Concatenating continuous models by linking their boundary conditions is a way to represent periodic continuous models for infinite and finite models.

3.2.1 Periodic models

Two beams with different characteristics can be linked with one or two degrees of freedom (deflection or slope), and can be defined as mono-coupled or bi-coupled, respectively. One method that can be used to do this in a simple way is the Transfer Matrix method. By replicating side by side the same boundary conditions, mass, stiffness and damping characteristics can be propagated from the left (*L*) to the right (*R*) side of a structure by using the Transfer Matrix method:

$$\{q^R\} = [T]\{q^L\} \tag{3.6}$$

with

$$[T] = [T_2][T_1] \tag{3.7}$$

for a beam unit cell with two different segments. Using the same development as the one used for the general solution of governing equation in Chapter 2, the following relation between right and left degrees-of-freedom and efforts can be obtained:

$$\begin{Bmatrix} u_y^R \\ \theta_z^R \\ M_z^R \\ V_y^R \end{Bmatrix} = \begin{bmatrix} c_1 & \frac{c_2}{\beta} & -\frac{c_3}{\beta^2 EI} & -\frac{c_4}{\beta^3 EI} \\ \beta c_4 & c_1 & -\frac{c_2}{\beta EI} & -\frac{c_3}{\beta^2 EI} \\ -\beta^2 EIc_3 & -\beta EIc_4 & c_1 & \frac{c_2}{\beta} \\ -\beta^3 EIc_2 & -\beta^2 EIc_3 & \beta c_4 & c_1 \end{bmatrix} \begin{Bmatrix} u_y^L \\ \theta_z^L \\ M_z^L \\ V_y^L \end{Bmatrix} \tag{3.8}$$

with

$$c_1 = (\cosh(\beta l) + \cos(\beta l))/2\,, \tag{3.9}$$

$$c_2 = (\sinh(\beta l) + \sin(\beta l))/2\,, \tag{3.10}$$

$$c_3 = (\cosh(\beta l) - \cos(\beta l))/2\,, \tag{3.11}$$

$$c_4 = (\sinh(\beta l) - \sin(\beta l))/2\,. \tag{3.12}$$

where l is the length of half-cell in this case.

Solving the eigenvalue problem $[[T] - \lambda I]\Phi = 0$, the eigenvalues and eigenvectors corresponding to the unit cell can be obtained. Dispersion constants can be obtained in the same way as in the previous chapter with $\lambda = e^{\mu}$, where the real part and the imaginary part of μ are denoted as δ and ε, respectively. The evanescent waves are represented by the attenuation constant δ and the propagating waves are defined by the phase constant ε.

Figure 3.2 shows a dispersion diagram for a continuous beam with unit cell length l and for stepped beam unit cell with different thickness (h_1=5h_2). The wave 2 on Figures 3.2(a) and 3.2(b) is evanescent inside all studied frequency domain while wave 1 is evanescent just inside the band gap zone. The ordinate (Ω) is normalized to the first non-zero natural frequency of the free-free unit cell stepped beam.

In spite of the fact that it is possible to calculate the dispersion constants, the Transfer Matrix can be ill conditioned because of finite-arithmetic operations in computers. This problem is addressed in the next section.

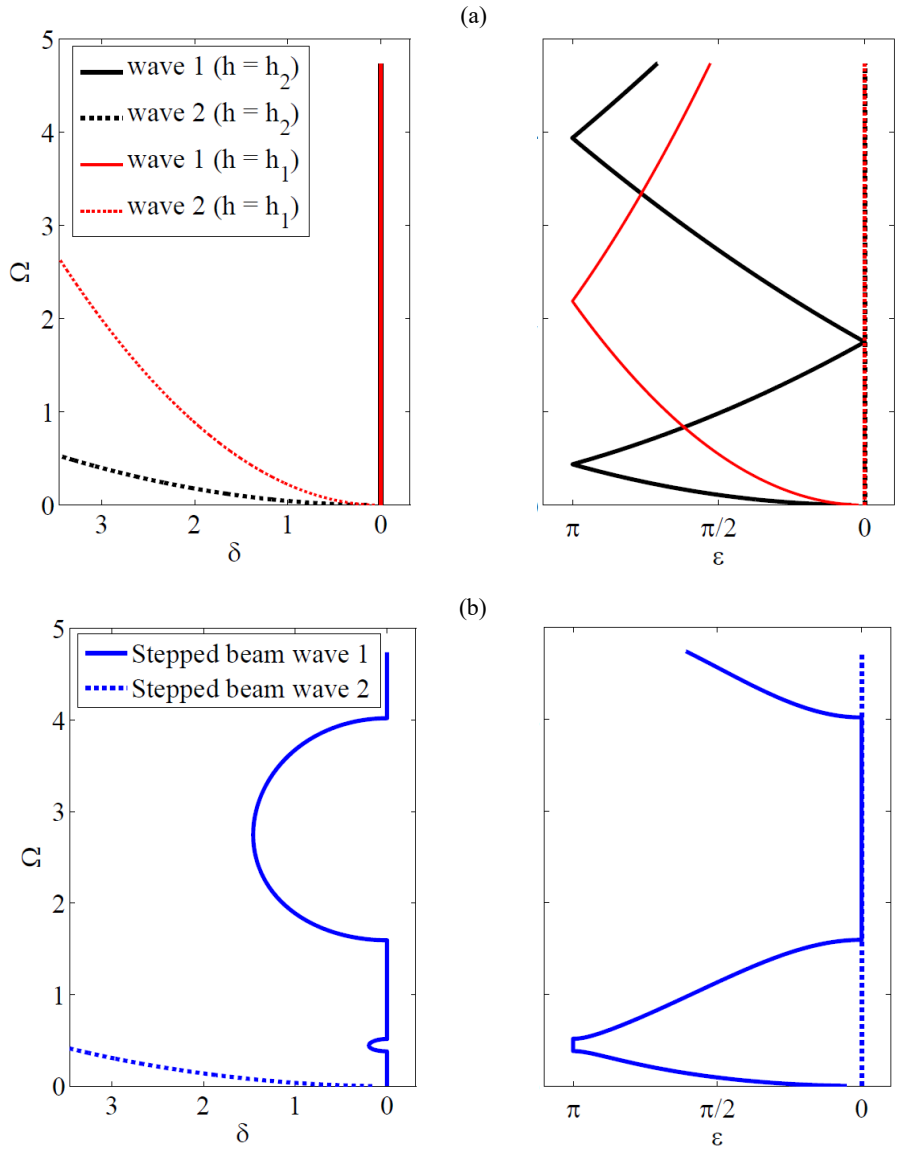

Figure 3.2 Dispersion constants considering flexural waves for (a) continuous beam and (b) stepped periodic beam.

3.3 Transfer Matrix method and stability problems

When assembling a high number of cells, the transfer matrix of equation (2.8) is self-multiplied many times. As an example, Figure 3.3(a) and Figure 3.3(b) show a frequency response function obtained with 10 multiplications of a transfer matrix for a continuous beam and for a periodic beam, respectively.

The *FRF* magnitude is scaled in dimensionless units $|kD(\Omega)| = |kD_{41}(\Omega)|$ with $k = 12EI_1 / l^3$ and subscripts representing vertical excitantion force on left (1) and response of vertical displacement on right (4).

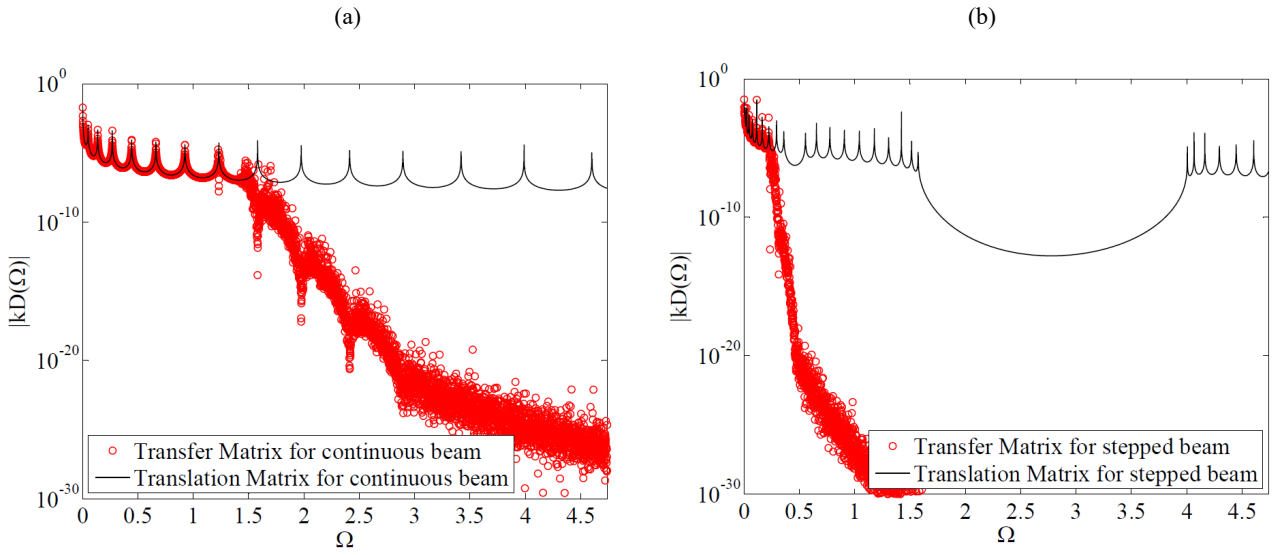

Figure 3.3 FRF Transfer Matrix method stability problem for: (a) continuous beam and (b) stepped periodic beam.

The black line in Figure 3.3 shows a frequency response function calculated using finite element method with fine mesh for an equivalent model. The red circles represent the FRF calculated with the Transfer Matrix method. It is possible to observe that numerical instability begins after $\Omega = 1.25$ and $\Omega = 0.25$ for a continuous beam and for a periodic beam, respectively. This problem appears as a result of small errors present in ill-conditioned matrices. Therefore, to avoid this multiplication, one alternative technique, termed Translation Matrix method is proposed.

The instability problem can be solved by improving the numerical conditioning of the transfer matrix, or avoiding self-multiplication and/or inverse calculation. A method, based on a recursive approach, adapted from (Dazel *et al.*, 2013) is proposed herein.

Some data, extracted from previous transfer matrix $[T_i]$, are necessary. The first step is to sort the eigensolution outputs, values $[\lambda_i]$ and vectors $[\Phi_i]$, according to the real part of eigenvalues as:

$$\mathrm{Re}(\lambda_1) > \mathrm{Re}(\lambda_2) > \ldots > \mathrm{Re}(\lambda_{2m}). \tag{3.13}$$

where m is the number of waves or *dofs*. The corresponding Transfer Matrix can be recalculated in function of sorted values as follows:

$$[T_i] = [\Phi_i][\lambda_i][\Psi_i]. \tag{3.14}$$

with $[\Psi_i] = [\Phi_i]^{-1}$.

In the following, the state-space representation is used for each layer or state i between cells, namely

$$\{S_i\} = [\Omega_i]\{X_i\}. \tag{3.15}$$

where $\{S_i\}$ is the state vector, $[\Omega_i]$ is the translation matrix and $\{X_i\}$ are the *dofs* or efforts vector (information vector). The Translation Matrix determines the link between information and state vectors. For a finite periodic structure, the first state on the left of a first unit cell is indicated by 0, as origin, and the last state on the right end of last cell is denoted by *n*. These states can be represented by the following equations:

$$\{S_0\} = [\Omega_0]\{X_0\}. \tag{3.16}$$

$$\{S_n\} = [\Omega_n]\{X_n\}. \tag{3.17}$$

Departing from the end of the structure, it is possible to obtain the state vectors from n to 0, and then recalculate all corresponding degrees-of-freedom or efforts from 0 to n:

$$\Omega_n \rightarrow \Omega_0 \rightarrow X_0 \rightarrow X_n. \tag{3.18}$$

For example, for a free end boundary condition, force and moment are imposed to be zero, while nothing is imposed on displacement and rotation. In this case, the following translation matrix $[\Omega_n]$ is used to link the state vector $\{S_n\}$ with the information vector $\{X_n\}$:

$$\begin{Bmatrix} u_y^n \\ \theta_z^n \\ M_z^n \\ V_y^n \end{Bmatrix} = \begin{bmatrix} \Omega_{11}^n & \Omega_{12}^n \\ \Omega_{21}^n & \Omega_{22}^n \\ \Omega_{31}^n & \Omega_{32}^n \\ \Omega_{41}^n & \Omega_{42}^n \end{bmatrix} \begin{Bmatrix} u_y^n \\ \theta_z^n \end{Bmatrix} = \begin{bmatrix} 1 & 0 \\ 0 & 1 \\ 0 & 0 \\ 0 & 0 \end{bmatrix} \begin{Bmatrix} u_y^n \\ \theta_z^n \end{Bmatrix}. \tag{3.19}$$

Typically, the goal is to obtain a displacement and rotation output on the right (n) caused by a force or moment excitation input on the left (0) of the structure. With specific components of Ω_0 it is possible to find X_0:

$$\begin{Bmatrix} u_y^0 \\ \theta_z^0 \end{Bmatrix} = \begin{bmatrix} \Omega_{31}^0 & \Omega_{32}^0 \\ \Omega_{41}^0 & \Omega_{42}^0 \end{bmatrix}^{-1} \begin{Bmatrix} M_z^0 \\ V_y^0 \end{Bmatrix} = \begin{bmatrix} \Omega_{31}^0 & \Omega_{32}^0 \\ \Omega_{41}^0 & \Omega_{42}^0 \end{bmatrix}^{-1} \begin{Bmatrix} 0 \\ 1 \end{Bmatrix}. \tag{3.20}$$

Table 3.1 shows the end translation matrices and information vector for a specific excitation and their corresponding boundary conditions.

Table 3.1 Examples of Translation Matrices and information vectors for the end and first layer or boundary.

End Type	**Diagram**	**Boundary condition on the end (response)**	$[\Omega_n]\{X_n\}$	**Possible excitations on first interface (excited)**	$\{X_0\}$
Free	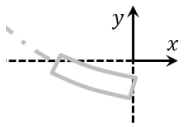	$\frac{\partial^2 y(L)}{dx^2} = -\frac{M_z^n}{EI} = 0$ $\frac{\partial^3 y(L)}{dx^3} = -\frac{V_z^n}{EI} = 0$	$\begin{bmatrix} 1 & 0 \\ 0 & 1 \\ 0 & 0 \\ 0 & 0 \end{bmatrix} \begin{Bmatrix} u_y^n \\ \theta_z^n \end{Bmatrix}$	$EI\frac{\partial^2 y(0)}{dx^2} = M_z^0$ $EI\frac{\partial^3 y(0)}{dx^3} = V_y^0$	$\begin{bmatrix} \Omega_{31}^0 & \Omega_{32}^0 \\ \Omega_{41}^0 & \Omega_{42}^0 \end{bmatrix}^{-1} \begin{Bmatrix} M_z^0 \\ V_y^0 \end{Bmatrix}$
Pinned (Rotating)	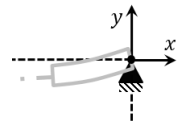	$y(L) = u_y^n = 0$ $\frac{\partial^2 y(L)}{dx^2} = -\frac{M_z^n}{EI} = 0$	$\begin{bmatrix} 0 & 0 \\ 1 & 0 \\ 0 & 0 \\ 0 & -1 \end{bmatrix} \begin{Bmatrix} \theta_z^n \\ V_y^n \end{Bmatrix}$	$y(0) = u_y^0$ $EI\frac{\partial^2 y(0)}{dx^2} = M_z^0$	$\begin{bmatrix} \Omega_{11}^0 & \Omega_{12}^0 \\ \Omega_{31}^0 & \Omega_{32}^0 \end{bmatrix}^{-1} \begin{Bmatrix} u_y^0 \\ M_z^0 \end{Bmatrix}$
Guided (Sliding)	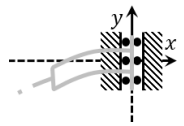	$\frac{\partial y(L)}{dx} = \theta_z^n = 0$ $\frac{\partial^3 y(L)}{dx^3} = -\frac{V_y^n}{EI} = 0$	$\begin{bmatrix} 1 & 0 \\ 0 & 0 \\ 0 & -1 \\ 0 & 0 \end{bmatrix} \begin{Bmatrix} u_y^n \\ M_z^n \end{Bmatrix}$	$\frac{\partial y(0)}{dx} = \theta_z^0$ $EI\frac{\partial^3 y(0)}{dx^3} = V_y^0$	$\begin{bmatrix} \Omega_{21}^0 & \Omega_{22}^0 \\ \Omega_{41}^0 & \Omega_{42}^0 \end{bmatrix}^{-1} \begin{Bmatrix} \theta_z^0 \\ V_y^0 \end{Bmatrix}$
Clamped	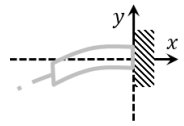	$y(L) = u_y^n = 0$ $\frac{\partial y(L)}{dx} = \theta_z^n = 0$	$\begin{bmatrix} 0 & 0 \\ 0 & 0 \\ -1 & 0 \\ 0 & -1 \end{bmatrix} \begin{Bmatrix} M_z^n \\ V_y^n \end{Bmatrix}$	$y(0) = u_y^0$ $\frac{\partial y(0)}{dx} = \theta_z^0$	$\begin{bmatrix} \Omega_{11}^0 & \Omega_{12}^0 \\ \Omega_{21}^0 & \Omega_{22}^0 \end{bmatrix}^{-1} \begin{Bmatrix} u_y^0 \\ \theta_z^0 \end{Bmatrix}$

For discontinuities created by supports inside the cell, i.e, not on the left neither on the right side of finite structure, continuity and equilibrium relations for displacement and stresses must be redefined. As this configuration is not observed with the periodic beam studied in this chapter, no intermediary condition is considered. More details can be found in (Dazel *et al.*, 2013).

To calculate all translation matrices, it is necessary to begin from the end of the structure until the first state as defined on following recursive equation:

$$\Omega_0 = T_1(T_2(T_3 ... (T_n(\Omega_n))...)) \tag{3.21}$$

where the function $T_i(\Omega_i)$ provides the translation matrix Ω_{i-1}. This function is presented as follows:

$$\Omega_{i-1} = T_i(\Omega_i) = [\Phi_i \,|\, ... \,|\, \Phi_{m-1} \,|\, 0]^{-1} + \Omega_i [\Xi_i']^{-1} \begin{bmatrix} \lambda_m - \lambda_1 & & & \\ & \ddots & & \\ & & \lambda_m - \lambda_{m-1} & \\ & & & 0 \end{bmatrix} \tag{3.22}$$

where

$$[\Xi_i'] = [\Psi_i][\Omega_i]. \tag{3.23}$$

In a similar way, all *dofs* and effort vectors can be obtained as:

$$X_n = W_n(W_{n-1}(W_{n-2}...(W_1(X_0))...)) \tag{3.24}$$

where the function $W_i(X_{i-1})$ provides the value of X_i:

$$X_i = W_i(X_{i-1}) = [\Xi_i']^{-1} \begin{bmatrix} -\lambda_1 & & & \\ & \ddots & & \\ & & -\lambda_{m-1} & \\ & & & -\lambda_m \end{bmatrix} X_{i-1}. \tag{3.25}$$

Considering a harmonic solution, all these steps can be performed for each frequency value and the *FRF* is obtained for a finite structure.

The improvement herein, compared to method presented by Dazel *et al.* (2013), is the manner of re-calculating the information vector presented in equation (3.20) for specific boundary condition. In addition, no application of this method, normally used in acoustics, was found in literature for multi-coupled systems involving flexural waves.

To verify the method described above, a finite element model using Euler-Bernoulli beam elements is used. Considering a harmonic excitation $V_y^L e^{i\omega}$, the following information vectors and translation matrices in function of ω are needed.

$$\{S_0(\omega)\} = [\Omega_0(\omega)]\{X_0(\omega)\}. \tag{3.26}$$

$$\{S_n(\omega)\} = [\Omega_n(\omega)]\{X_n(\omega)\}. \tag{3.27}$$

The equivalent of a FEM frequency response function can be obtained as:

$$\left|\frac{u_y^R}{V_y^L}\right| = \left|\frac{S_n^1(\omega)}{S_0^4(\omega)}\right| = |D_{41}(\omega)| = |D(\omega)|. \tag{3.28}$$

where $S_n^1(\omega)$ indicates the corresponding displacement (1 for u_y^n)value on interface *n* and $S_0^4(\omega)$ represents the corresponding effort (4 for V_y^0) value on interface 0.

Figure 3.4 shows the FE mesh convergence for 2, 6 and 10 finite elements per half-cell. For a finite model with 10 cells, the respective numbers of finite elements are 40, 120 and 200. The FE results are compared to those obtained by using the Translation Matrix method.

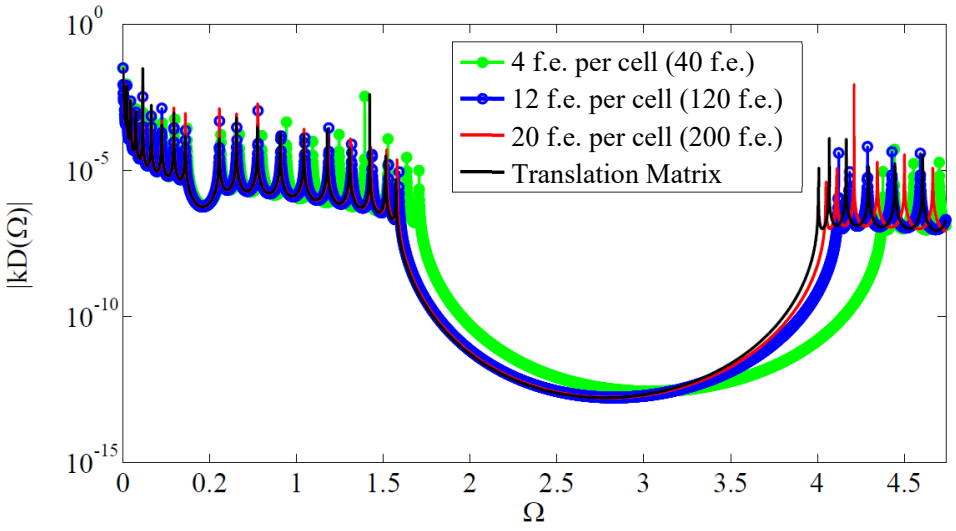

Figure 3.4 FRF convergence of finite element mesh to Translation Matrix model for a periodic beam with 10 cells.

It is possible to observe that as the number of finite elements increases, the frequency response become overlapped. The black line on Figure 3.4 is the frequency response function calculated with Translation Matrix method.

For a continuous structure, the analytical FRFs can also be used in comparison. In Figure 3.5, the analytical response frequency function is almost perfectly overlapped by that obtained by using the Translation Matrix method. Therefore, this method is validated.

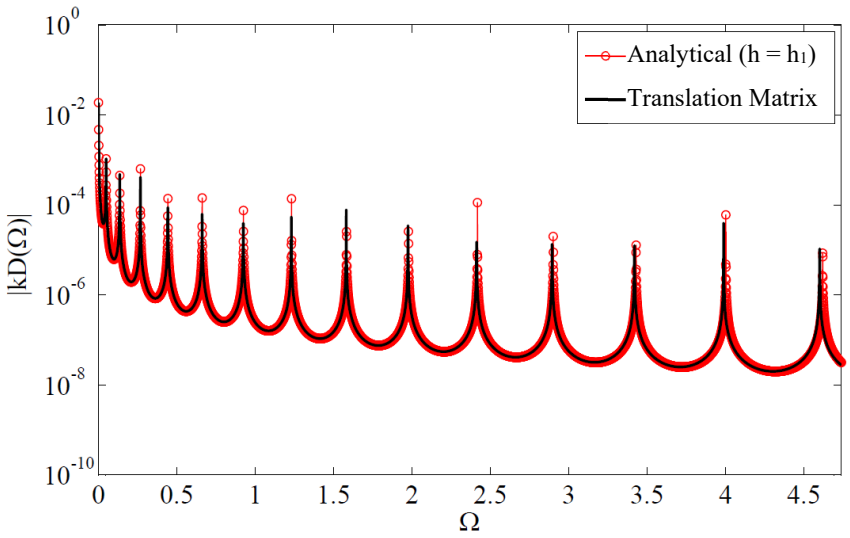

Figure 3.5 Comparison of Translation Matrix method FRF for a continuous beam composed of 10 continuous parts with analytical FRF.

3.4 Numerical examples

3.4.1 Two continuous part beam parametric study

In this numerical example, the effect of thickness change in the width of the bandgap and the robustness of this solution to uncertainties are investigated. It is interesting to notice that producing a thickness discontinuity can be used as an strategy to create a large Bragg bandgap. Differently from Chapter 2, the variation of physical parameters is not analyzed in this chapter. Special attention is given to effects of geometrical properties for a beam unit cell. As mentioned in Chapter 2, the manufacturing process is the main source of uncertainties in structures.

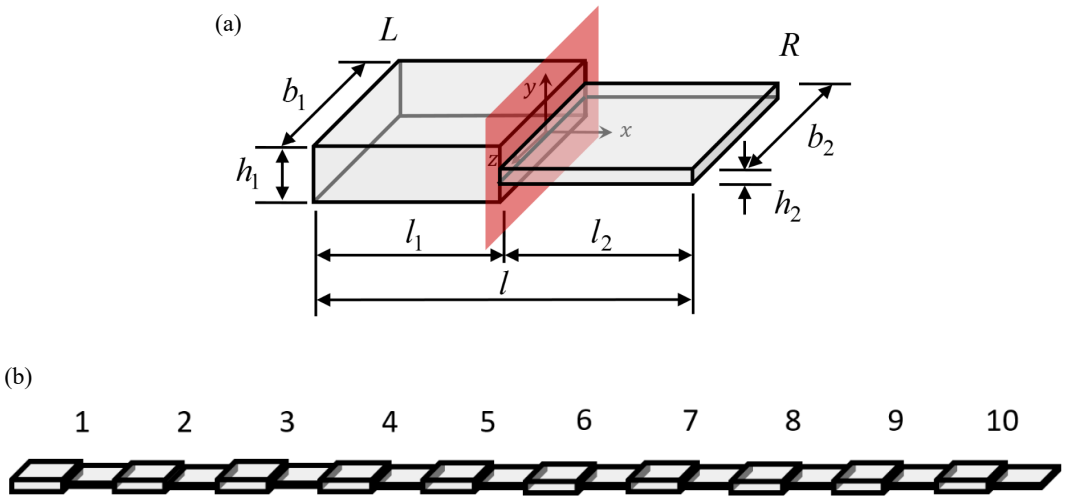

Figure 3.6 (a) Asymmetric beam unit cell and (b) its finite structure with 10 cells.

The variation of geometric variables are investigated in this subtopic. Figures 3.7(a) and 3.7(b) illustrate the influence of the variation of thickness h_2 and width b_2, respectively. In this case, the values of h_1 and b_1 are kept constant.

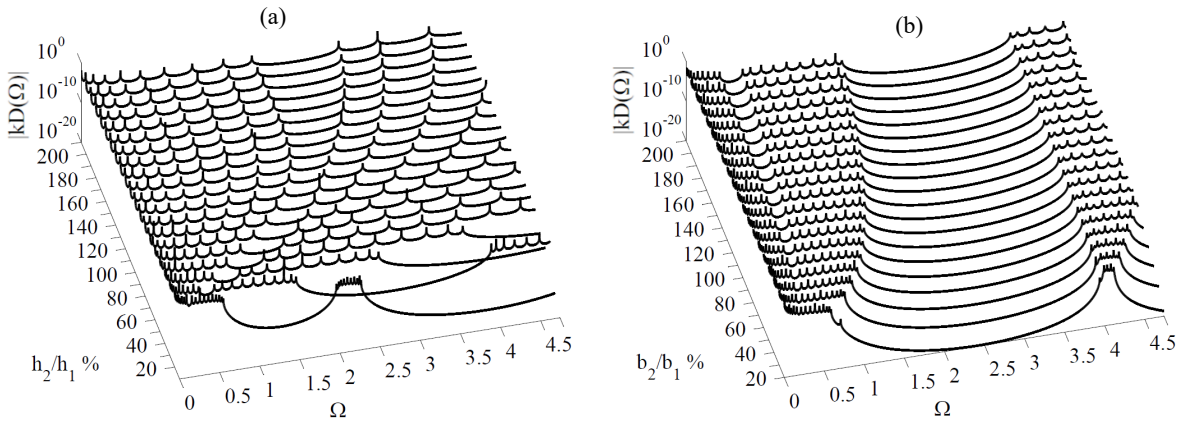

Figure 3.7 FRFs of stepped beam for several values of beam (a) thickness h_2 and (b) width b_2.

In other words, increasing geometric properties that are related to bending stiffness shifts the natural frequencies to higher frequencies and the same is observed for bandgap borders. Inversely, by increasing geometric properties related to inertia, the bandgap is moved to lower frequencies.

Figures 3.8(a) and 3.8(b) present the influences of the discontinuity location, *i.e.*, the position of cross section area mismatch, and the cell length l, respectively. They have a similar effect, shifting the attenuation zone to lower frequencies.

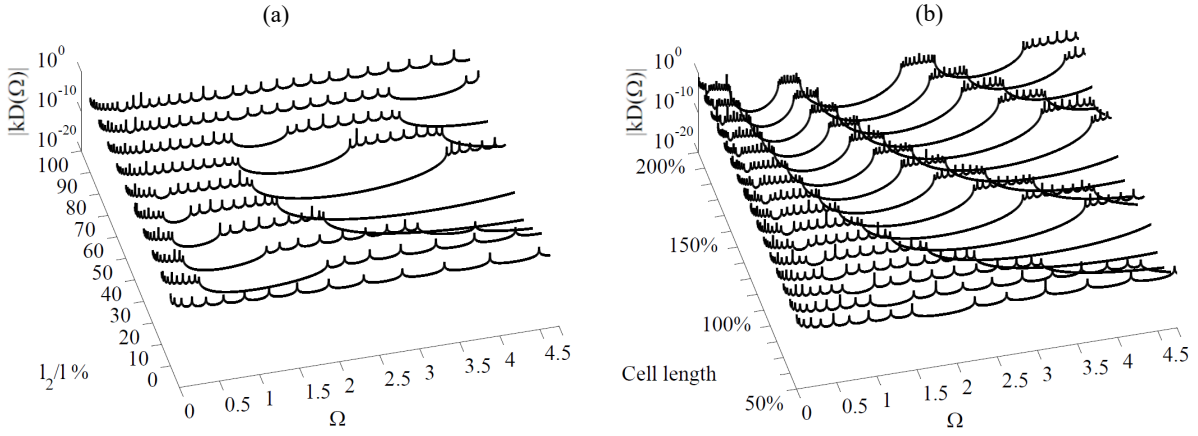

Figure 3.8 FRFs of stepped beam for several values of (a) discontinuity location and (b) cell length l.

3.4.2 Probabilistic analysis and robust bandgap

In the following, infinite and finite models are used in a probabilistic analysis, and results are compared. The same concept used in Chapter 2 is applied for flexural waves. As the cross section area is used in this example, in order to compare trends obtained for longitudinal and flexural waves, the thickness of the second segment h_2 is used as input stochastic variable. The relation $h_2 = h_1/5$ is adopted.

Considering the thickness h_2 as random parameter, a Monte Carlo Simulation (MCS) with Latin Hypercube is performed. To realize this investigation, for each standard deviation of input variables, a convergence of MCS is achieved and the outputs are obtained.

Figure 3.9 shows the frequency response functions for a finite structure with 1, 4, 10 and 16 cells. It can be again verified that as the number of unit cells increases, the attenuation inside the bandgap also increases.

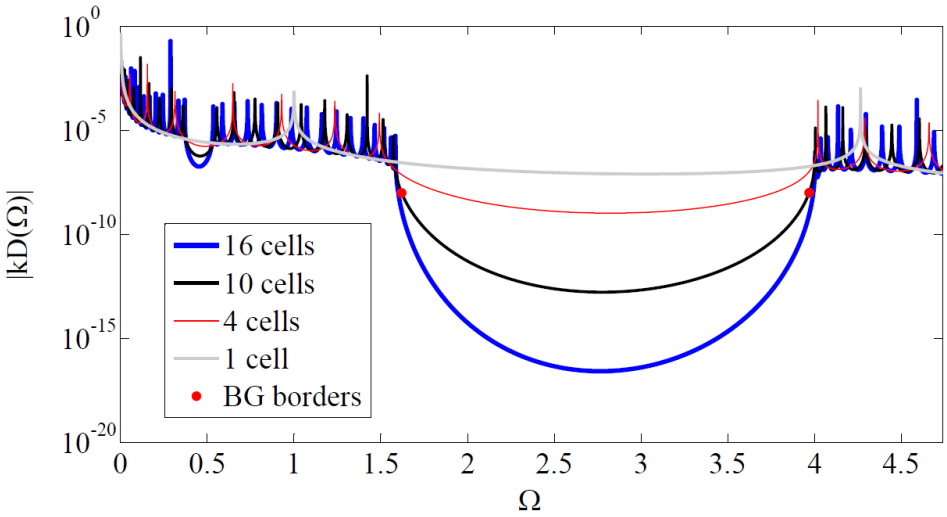

Figure 3.9 Number of cells for a stepped unit cell finite structure for an observable attenuation zone.

Similarly to what have been done in Chapter 2, Figure 3.9 shows that a 10-cell model is satisfactory for identifying the attenuation zone on finite structure. In this calculation, the band gap edges corresponding to lower bound (*LB*), upper bound (*UB*) and width (*W*) are the outputs as indicated in equations (2.27) to (2.29). Figures 3.10(a) and 3.10(b) show an illustration of these variables where the red dots are the *LB* and *UB* for a finite (*FS*) and an infinite structure (*IS*), respectively.

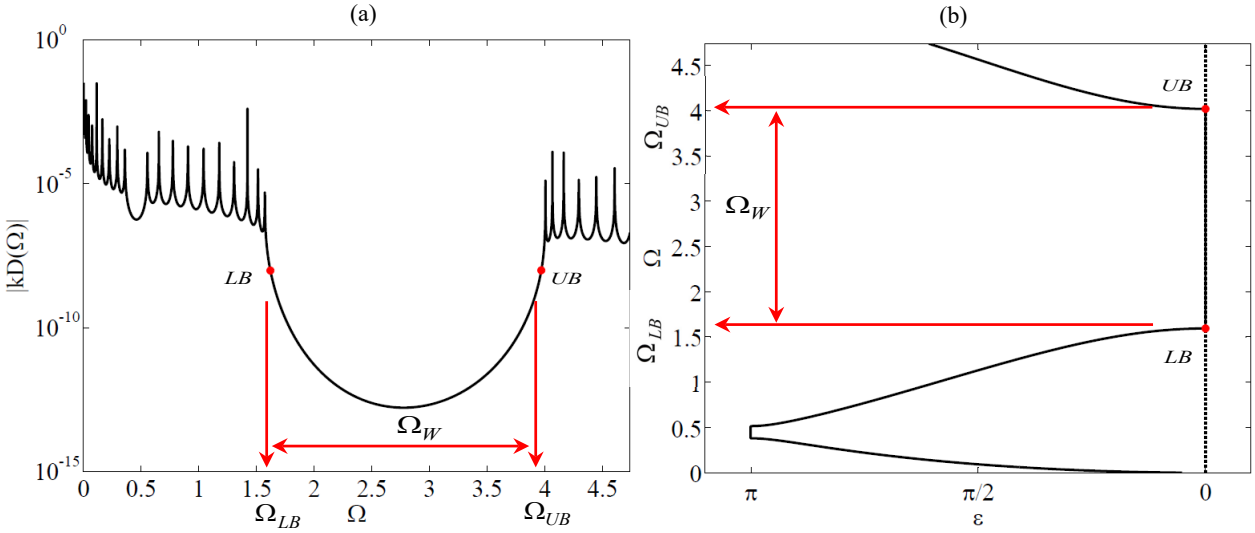

Figure 3.10 Bandgaps borders and width for (a) finite model and (b) infinite model.

The random variables are represented by normal probability density functions. Two variants of uncertainty distribution are considered:

- Type 1: a single numerical sample of the random thickness h_2 is applied to all the 10 cells. Consequently, the structure remains periodic;

- Type 2: 10 different samples of the random thickness h_2 are applied, one in each of the 10 cells. In this case, the structure is not perfectly periodic, meaning quasi-periodicity.

For both cases, infinite and finite structure models are analyzed considering the Translation Matrix exact model. The same values of the coefficient of variation γ used in Chapter 2 are used here. This parameter varies from 2% to 20% with a step of 2 %. Then, for each considered value, a Monte Carlo Simulation with Latin Hypercube is performed until its convergence (number of samples around 5000).

Figure 3.11 shows the variation of the frequency bandgaps, represented by mean values and their 95% confidence intervals, for variants types 1 and 2.

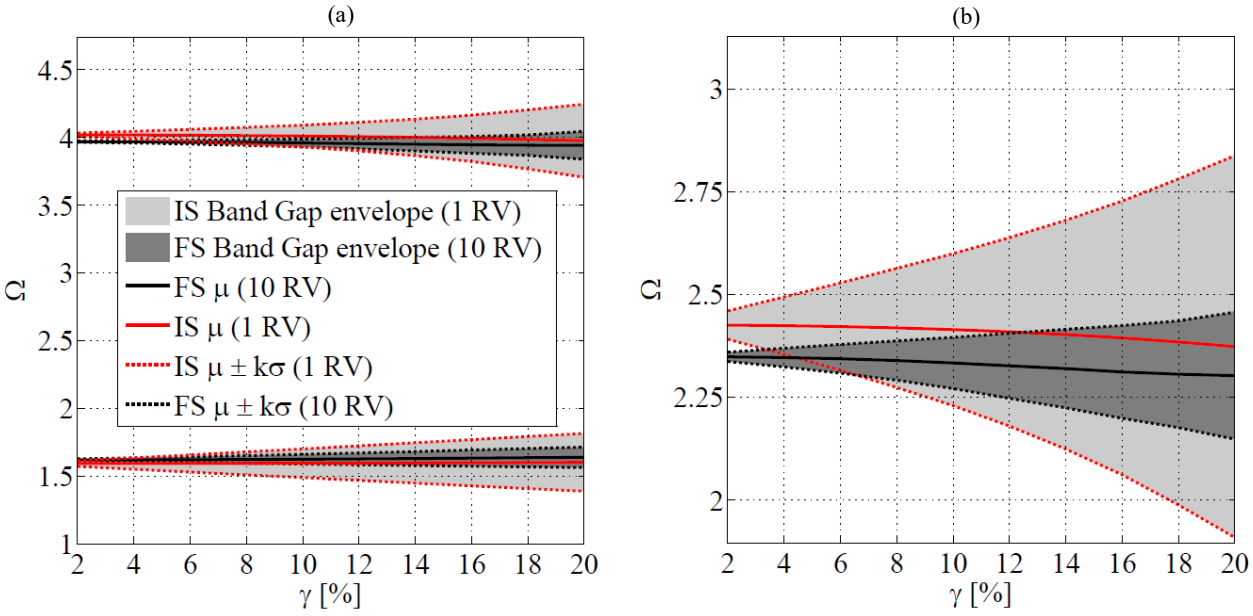

Figure 3.11 Confidence intervals for (a) LB, UB and (b) W for infinite structure (IS) with a stepped beam unit cell and for a finite structure (FS) with 10 stepped beam unit cells.

It is possible to observe that the edges of the stopband envelope increase their values according to the increase of uncertainty. In cases with one random variable, for example, for every 1% of uncertainty, the limits of attenuation zone vary nearly ±0.01 in terms of dimensionless frequency. In cases with 10 uncertainties, these bounds vary around ±0.005 in dimensionless frequency, almost the half of the case mentioned before. However, the means of border values are slightly different, which causes an offset between envelopes of confidence interval.

Considering an uncertainty level of 10 % for the thickness h_2, the robust bandgap will be the light and dark gray areas considered in Figures 3.12(a) and 3.12(b) for finite and infinite models, respectively.

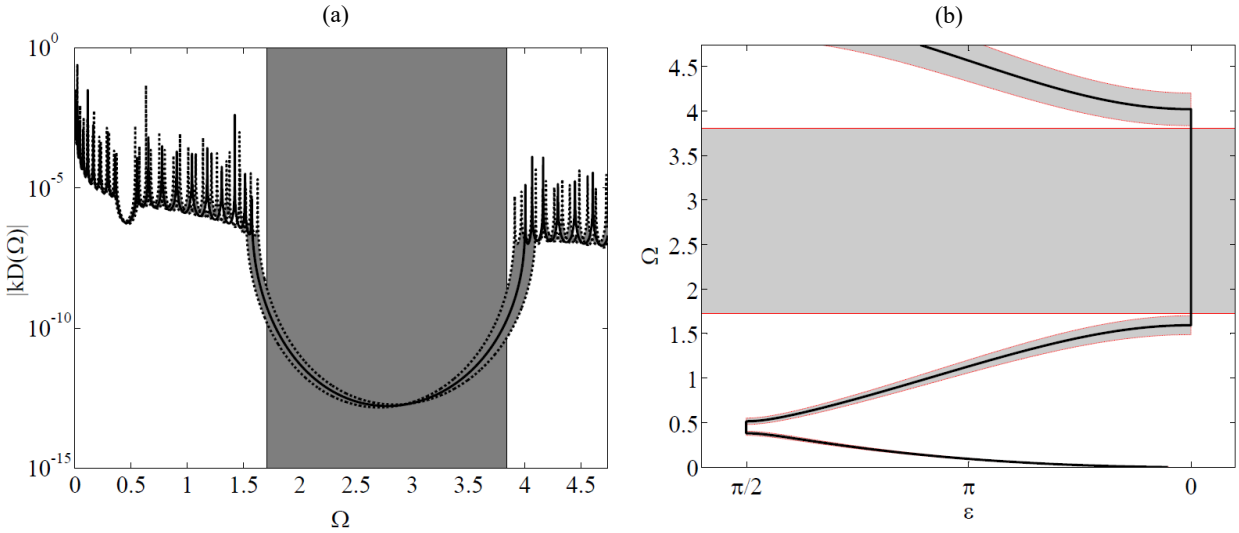

Figure 3.12 Robust bandgap for a stepped beam example considering (a) finite and (b) infinite structure.

The light gray areas in Figure 3.12(b) indicate the robust attenuation zone calculated with a single random variable. They are obtained using the light gray confidence interval with the uncertainty parameter equal to 10%. The dark gray area in Figure 3.12(a) is obtained in the same way but considering 10 random variables for a finite structure. In this case, the stop band has almost the same width as the light gray. Therefore, the same result is not verified as the robust band present in Chapter 2. The robustness of finite structure is not verified although this would be expected. It is necessary to consider more unit cells to be able to get more reliable attenuation zones using finite models. Considering values higher than 14% for γ in Figure 3.11(a), the robustness of finite structure is verified and it can be explained by a compensation effect on the responses.

3.4.3 Localization phenomena in stepped beam unit cell

The presence of localized modes on symmetric finite structures is investigated with two different types of symmetric unit cells presented in Figure 3.13. They have the same dispersion constants for an infinite model. They are composed by three segments, among which the first and third segments have the same thickness and length.

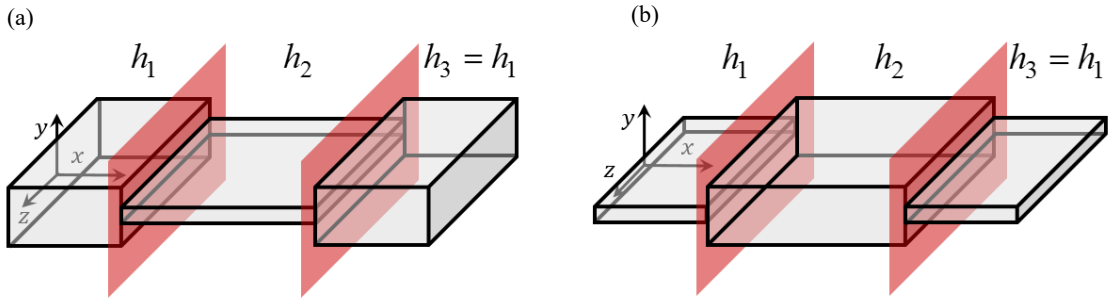

Figure 3.13 Symmetric unit cells (a) 1 and (b) 2 for flexural beams.

Figures 3.14(a) and 3.14(b) show the frequency response function for 1-cell finite structure (black line) and 10-cells finite structure (blue line with circles) for the symmetric unit cells of Figures 3.13(a) and 3.13(b), respectively. Differently from periodic rod models, the response function for one free-free cell presents resonance frequencies inside the attenuation zones but they are not the same as shown in the frequency response obtained with 10 unit cells for a finite structure. Therefore, the same localization phenomenon presented for rod models on the previous chapter, because of the asymmetry of the cell, is not observed in periodic beam models.

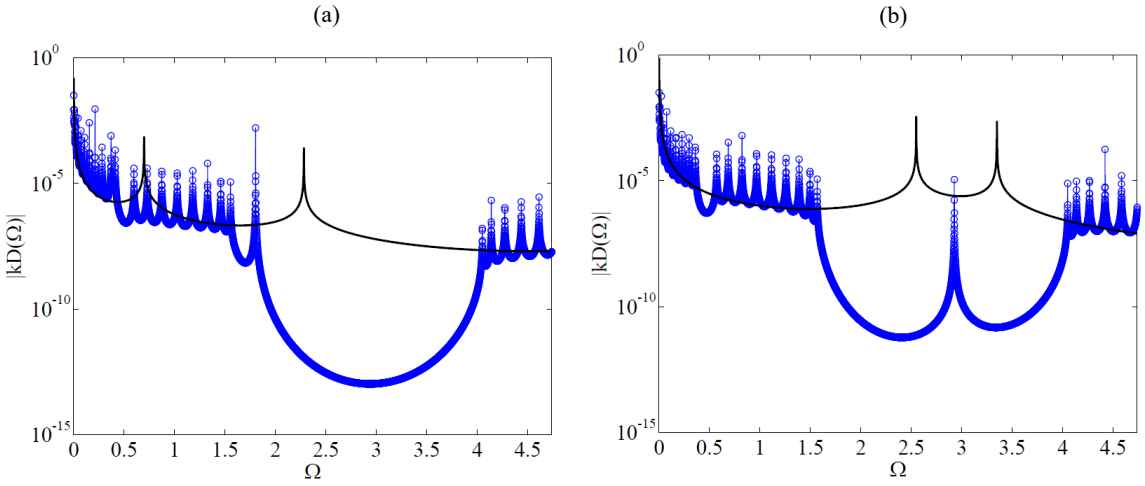

Figure 3.14 FRFs of a finite structure with one and ten cells for symmetric cell (a) 1 and (b) 2.

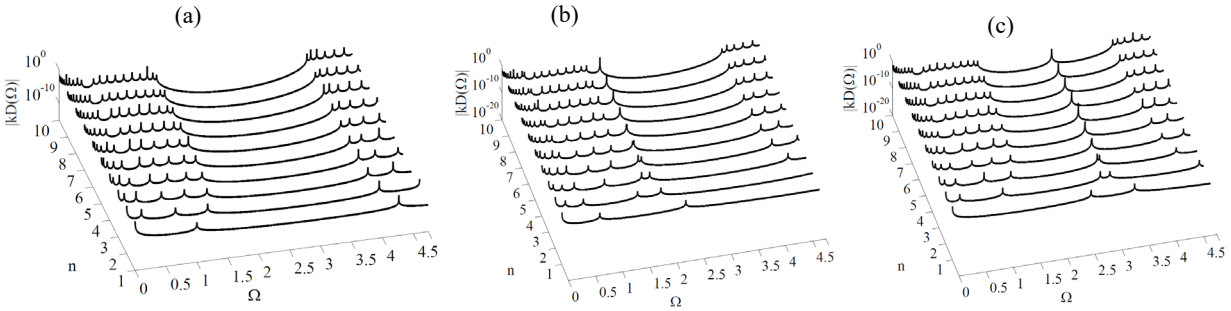

Figure 3.15 FRFs for convergence of cell number for: symmetric cases (a) and (b) and asymmetric case (c).

Figure 3.15(a) show the convergence of bandgap with increasing number of cells for assymetrical unit cell of Figure 3.6(a). Figures 3.15(b) and 3.15(c) show the FRFs with increasing number of cells for the unit cells presented in Figures 3.13(a) and 3.13(b). In the first figure, it is possible to note that as the number of cells increases, the natural frequency shifts to lower frequencies. Differently, for the second figure, two natural frequencies presented inside the attenuation zone seem to merge in just one as the number of cells increases.

3.4.3.1 Introduction of damping

To reproduce another type of localization phenomenon inside the bandgap region, without considering a unit cell analysis, a cell in the middle of the structure is considered with no impedance mismatch, *i.e.*, the

first half of cell 6 has the same thickness as its second half. Figure 3.16 shows the finite structure with induced localization.

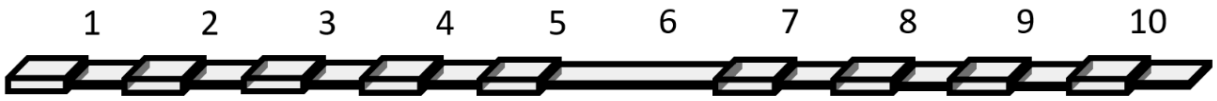

Figure 3.16 Periodic beam with 10 cells and localization phenomenon on cell 6 ($h_1 = h_2$).

In the following, proportional damping ($E = E(1 + \eta j)$) is introduced in cell number 6 where there is "defect" placement. Figure 3.17 shows the frequency response function with localized mode with η = 0.001 and without damping.

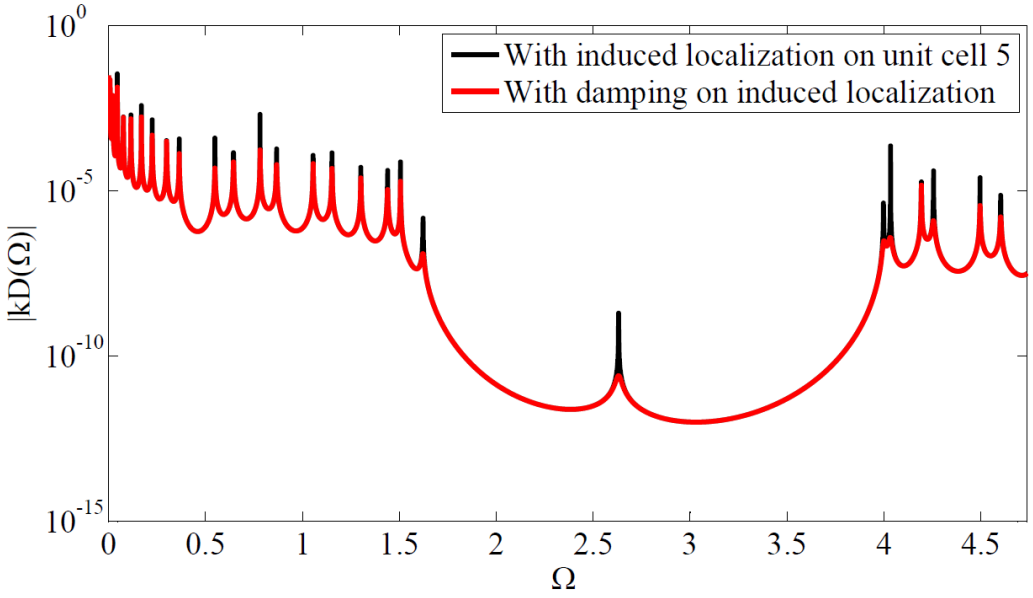

Figure 3.17 FRF of a beam periodic structure with localization phenomena and damping on cell 6.

Figure 3.17 shows that the natural frequency inside the attenuation zone has more damping than the others peaks analyzed in this frequency domain. In other words, a localized damping can be placed in localization mode location to reduce the amplitude of resonance peak. Therefore, by increasing the damping in this region, the magnitude of this localized mode can be also decreased.

3.5 Partial conclusion

One simple model describing flexural wave propagation using periodic Euler-Bernoulli beams is investigated in this chapter.

The use of exact solutions is envisaged. However, the Transfer Matrix method is not suitable for this case due to the presence of ill-conditioned matrices. A method called Translation Matrix method is proposed to circumvent the numerical stability problem in the computation of frequency response functions. This method, adapted from (Dazel *et al.*, 2013), is based on a recursive methods used in acoustic models involving sound waves. The results presented in this chapter illustrate its suitability for use in association with propagation of flexural waves. It is faster comparing to finite element models and more accurate, as it provides the exact solution from a mathematical point of view.

It is observed, in the parametric analysis, that increasing the values of geometric properties that are related to bending stiffness leads to shifts of the natural frequencies to higher frequencies; the same is observed for bandgap borders. Inversely, by increasing geometric properties related to inertia of structure, the stop band is move to lower frequencies.

A probabilistic analysis is performed using a Monte Carlo Simulation with Latin hypercube considering two cases: infinite and finite structures. Differently from periodic rods with stepped unit cells, the difference between robust band gap calculated with 1 random variable for infinite model and the robust bandgap calculated with 10 random variables for finite model is not so notable. The envelope with 95% confidence is larger for infinite structure. However, bandgaps obtained with infinite and finite models are almost the same.

Differently from periodic rods, it is verified that the cell asymmetry does not cause the appearance of localization phenomena inside the attenuation zone for flexural waves. Increasing the number of cells may however move some natural frequencies inside the stop band.

Concerning the induced localization phenomena by creating a different mismatch on a given cell, the presence of a new localized peak inside the flexural waves attenuation zone is verified. Moreover, damping can be used as a way to reduce the amplitude of natural frequencies inside the stop band.

Chapter 4 Experimental analysis of flexural beams

4.1 Introduction

This chapter presents an experimental analysis to validate the finite periodic models studied before, including the concept of robust bandgap. Despite the existence of uncertainties in all its dimensions, manufactured structures tend to have more deviations in specific dimensions according to the machining techniques. For example, milling technique can present more deviations in dimensions such as cut depth and cut length.

In the present study, a continuous extruded beam had material removed with this technique to produce a periodic beam. This type of structure is suitable for an experimental survey in virtue of the presence of attenuation zones for flexural waves in low frequencies, in comparison to longitudinal waves, as verified in Chapter 3.

The material selected for the beams is aluminum, since it facilitates the machining process and avoids cracks and other defects. A numerical simulation is performed, considering the above-mentioned aspects, and a periodic aluminum beam with stepped unit cells is designed for identification of flexural waves and Bragg's bandgap.

The experiment is carried-out based on the assumption that only flexural waves are excited. An impact hammer is used to excite the left end of the beam and an accelerometer is used to collect the response on the right end. Impact excitation is simpler, less expensive, and faster than using a shaker. However, it is difficult to control the direction of the impact.

In the following, the results obtained for a continuous and for a periodic beam are compared with numerical results calculated with the Translation Matrix method.

In spite of the existence of uncertainties in many parameters of this periodic beam, a probabilistic analysis is performed considering only the length of each half-cell as uncertain. The Gaussian probability density function is used to represent the stochasticity with measured mean and calculated standard deviation as inputs for a Monte Carlo Simulation combined with Latin Hypercube Sampling. A confidence interval envelope and a robust band gap are defined, considering only this random variable.

Unexpected modes appeared inside the attenuation zone and some comments and hypotheses are drawn to explain this phenomenon.

4.2 Modeling of stepped beam unit cell with six *dofs*

A rectangular cross-section with longitudinal, flexural waves on both planes and torsion is considered in the Translation Matrix model used in this chapter. Therefore, displacements and rotations in *x*, *y* and *z* are considered. These *dofs* are modeled using a full Euler-Bernoulli beam model enabling to characterize longitudinal wave propagation addressed in Chapter 2, as well as flexural wave propagation considered in Chapter 3, besides an additional *dof* related to torsion and shear waves. The interest is to create only one matrix composed by the others, such as used in finite element method. To introduce this degree of freedom, the same idea of Chapter 2 is used, since longitudinal and torsion motion have similar governing equations, but different wave speeds. This transfer matrix can be described by

$$\mathbf{T}_i(\omega) = \begin{bmatrix} \cos(\gamma_i l_i) & \frac{1}{z_i}\sin(\gamma_i l_i) \\ -z_i \sin(\gamma_i l_i) & \cos(\gamma_i l_i) \end{bmatrix} \tag{4.1}$$

with wave number $\gamma_i = \omega/c_i$, frequency ω, wave speed (for shear waves) $c_i = \sqrt{G_i/\rho_i}$ considering the shear coefficient $G_i = C_i/J_i$ where C_i is the torsional rigidity and J_i is the polar moment of inertia for *i* being the segment. Similar to longitudinal vibration, but for torsional, the impedance $z_i = \omega A_i \sqrt{G_i \rho_i}$ with the cross-section area A_i and the density ρ_i. For rectangular cross-section $A_i = b_i h_i$, the area moment of inertia on y-axis is $I_y = b_i h_i^3/12$, on z-axis is $I_z = h_i b_i^3/12$ and polar moment of inertia is $J_i = \kappa_i h_i b_i^3$ with the width b_i, the thickness the h_i and κ_i a constant ratio between these two previous dimensions. Together with other matrices, it can assemble a transfer matrix 12×12 with all *dofs*.

Using this transfer matrix with six degrees of freedom, the numerical instability problems addressed in Chapter 3 can appear for flexural modes in low frequency and at higher frequency for other wave types. Solving the eigenvalue problem for six *dofs*, the dispersion constants are obtained. To illustrate their use, the dispersion constants of a continuous beam and a stepped beam unit cell have been calculated using parameters described in Table 4.1 and are presented in Figures 4.1(a) and 4.1(b), respectively.

Table 4.1 – Properties for continuous beam and for periodic beam with stepped unit cell.

Parameter	Variable [unit]	Value		
		Continuous beam	Stepped beam unit cell	
			First half	Second half
Young's Modulus	E [N/m²]	0.7×10^{11}	0.7×10^{11}	0.7×10^{11}
Poisson	v [-]	0,333	0,333	0,333
Density	ρ [kg/m³]	2700	2700	2700
Width	b [mm]	60	60	60
Thickness	h [mm]	10	10	2
Length	l [mm]	100	50	50

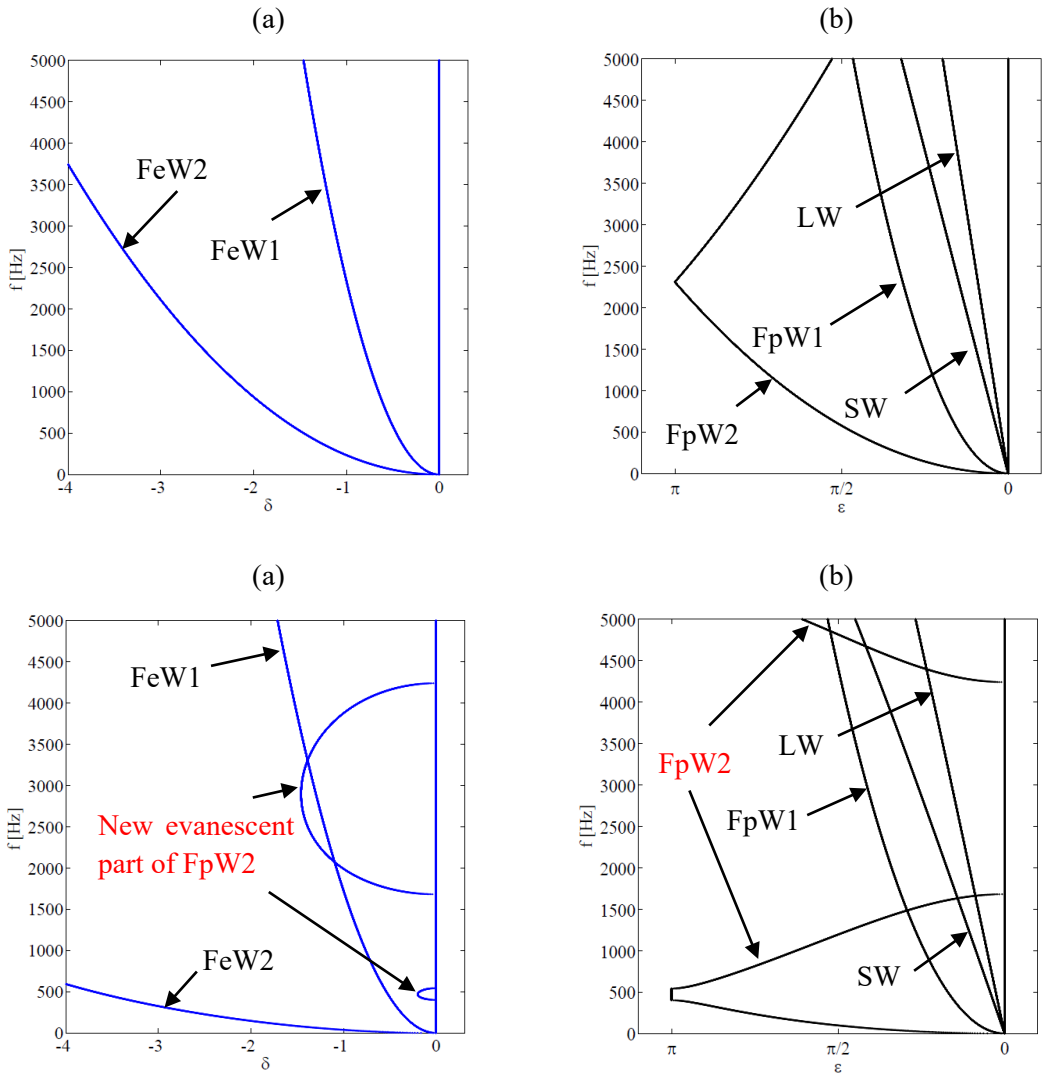

Figure 4.1 (a) Real and (b) imaginary parts of dispersion constants for continuous beam unit cell and (c) real and (d) imaginary parts for stepped beam unit cell.

It is possible to classify all types of waves propagating in a beam as shown in Figure 4.1(a) and 4.1(b). There are two non-dispersive waves, one corresponding to the longitudinal waves (*LW*) and the other to shear waves (*SW*). For each coordinate plan, there are two waves related to bending that are dispersive without presenting periodicity. Two of them (*FeW1* and *FeW2*) are evanescent inside all the analyzed domain and the other two are propagative (*FpW1* and *FpW2*). These wave types are pointed with arrows in Figure 4.1(a) and 4.1(b).

By removing material and creating the same periodicity considered in Chapter 3, it is possible to observe in Figure 4.1(c) and 4.1(d) that some branches change their shape. In other words, there are variations on stiffness and mass properties for corresponding wave type. The group speed changes for some waves and for a specific one there is the appearance of frequency zone where it becomes evanescent, *i.e.*, a partial bandgap is created and flexural waves cannot propagate inside this zone. When such a full model is used, it is hard to track and sort the dispersion diagrams branches according to wave type. They can be tracked according to various strategies (Billon, 2016; Silva, 2015) but the nature of stop bands (Bragg's, local reso-

nance and coupling waves) in different frequency zones makes them difficult to follow in the frequency domain. This topic will be enlighten in next chapter devoted to periodic truss.

Focusing on flexural waves in virtue of the presence of this partial bandgap in Figure 4.1, the Translation Matrix Method with six *dofs* is verified in the following.

4.2.1 Translation Matrix with six *dofs* verification

To validate the Translation Matrix method described above, a finite element model using Euler-Bernoulli beams was used. Considering a transverse harmonic excitation to excite only flexural waves on a free-free beam, the Figure 4.2 shows the frequency response using FEM and Translation Matrix method with six *dofs*.

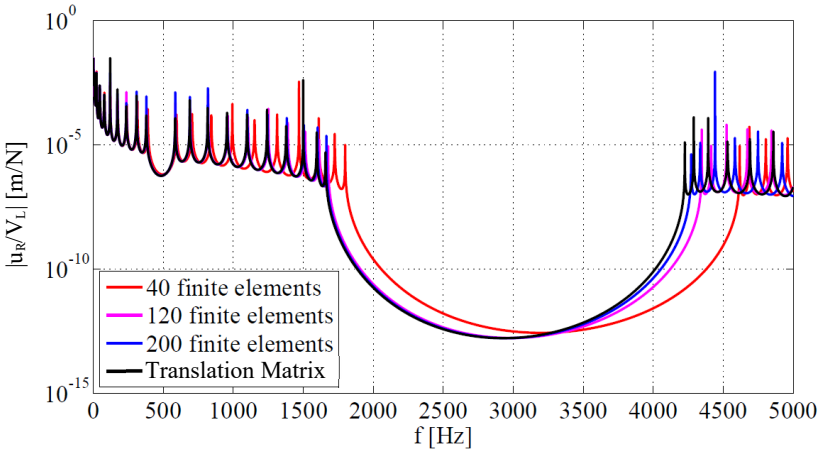

Figure 4.2 FRF convergence of F.E. model for a periodic beam with 10 cells to Translation Matrix model with six *dofs*.

In order to illustrate the performance of Translation Matrix method, the results obtained for flexural waves in periodic beams are compared. Table 4.2 shows the computation time and the error between *FRFs* obtained using method Translation Matrix method with six *dofs* and using FEM with 40, 120 and 200 finite elements. A computer with processor Intel Core i7-4500U CPU (two cores) and 8 GB of RAM was used to perform the calculations. The mean absolute percent error (MAPE) is calculated as:

$$MAPE = \frac{100}{5000} \times \sum_{i=1}^{5000} \left| \frac{FRF_{FEM}(i) - FRF_{TMM2}(i)}{FRF_{TMM2}(i)} \right| \tag{4.2}$$

where i is the frequency point from 1 to 5000, FRF_{FEM} is the frequency response function obtained with finite element method and FRF_{TMM2} is the corresponding frequency calculated with Translation Matrix method. It can be noted that the higher relative error correspond to the mesh with lower number of finite elements

and it means that the FEM results are converging to Transfer Matrix method. It is possible to considerer damping in this model and it is used to compare the experimental and numerical results.

Table 4.2 Validating method for two continuous part unit cell periodic beam.

Used Method*	Unit cell mesh (FEs)	Computation time	MAPE [%]	Time reduction [%]
FEM	40	0h 15m 17s	10,27 %	33 %
	120	0h 33m 41s	3,17 %	66 %
	200	1h 13m 11s	2,18 %	86 %
Translation Matrix	-	10 min	-	-

*For a FRF with 5000 points.

4.3 Experimental bench and setup

An experimental analysis is performed to verify the half-cell length uncertainty effects on a periodic beam with stepped unit cell. Figure 4.3 presents the experimental set-up composed by one impact hammer PCB®, one accelerometer ICP-PCB®, one acquisition and signal conditioning board NI® and a computer with software LabVIEW® and a homemade MATLAB® script for post-processing.

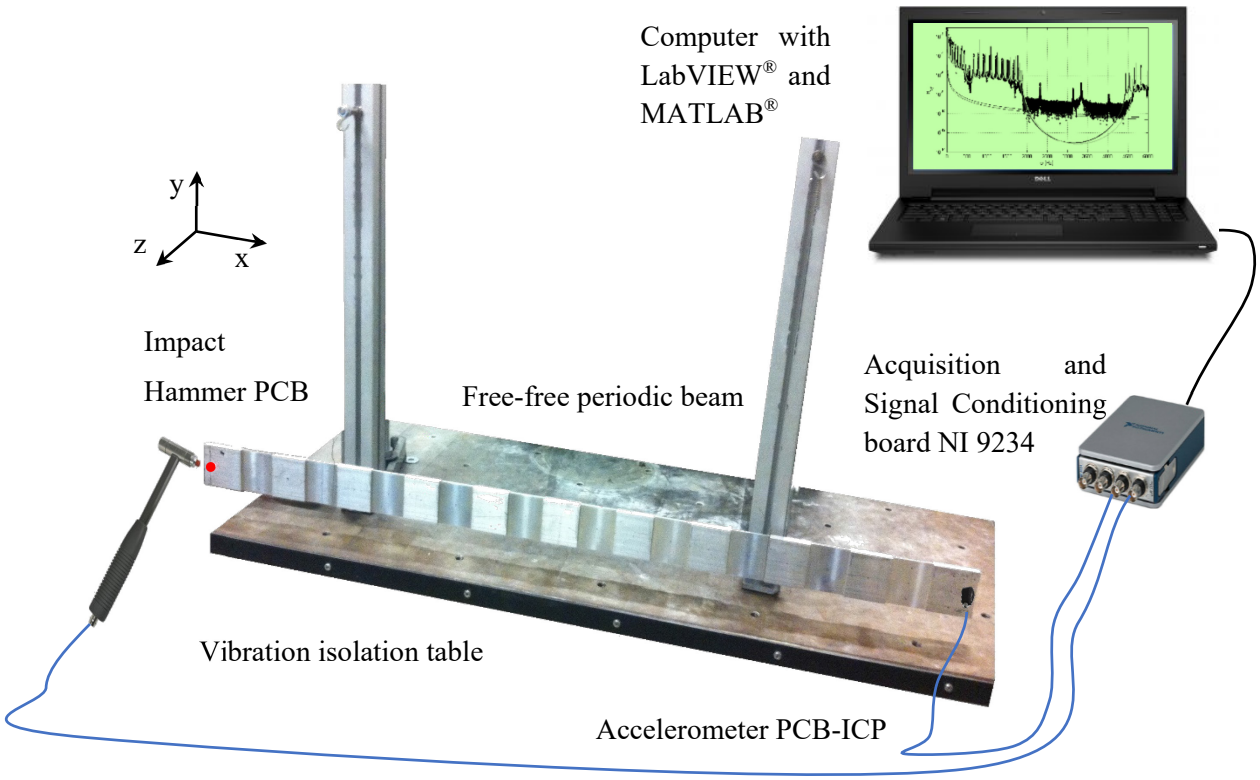

Figure 4.3 Experimental set up for a periodic free-free beam.

Two experiments are conducted: one to verify the results on a continuous beam and the second one using a periodic beam with dimensions described on Table 4.3. To avoid self-weight deflection and exciting

longitudinal waves on x-axis and flexural waves on xz-plane, thickness dimension is chosen to be considerably smaller than width dimension. See table 4.3 for details. Milling has been used to remove material and fabricate this periodic beam. The beam is suspended using fishing line to represent free-free boundary conditions. The PCB accelerometer is placed on the right side of the structure, *i.e.*, in the last cell, and first cell is excited by a PCB Impact Hammer. To avoid exciting torsion modes (shear waves), the excitation point was defined in the middle width of first cell with 1 cm from its left border as shown on Figure 4.3. In this case, the first half-cell has around 60 mm, 10 mm more than other cells segments. The accelerometer is placed 5 mm from the right border of last half-cell. The impact hammer and the accelerometer are connected to a board NI 9234 for data acquisition and signal conditioning. This board transfers the data to a computer with LabVIEW® that transforms this information in treatable data for MATLAB®. It is possible to excite the frequency band from 0 to 5000 Hz with the impact hammer with a rigid metal tip.

4.4 Numerical and experimental results

Table 4.3 presents the values of physical and geometrical properties for the periodic stepped unit cell beam illustrated in Figure 4.3.

Table 4. 3 Geometrical and Physical properties of periodic beam

	Parameter	**Variable [unit]**	**First half cell**	**Second half cell**
General properties	**Young Modulus**	E [GPa]	$0{,}7\times10^{11}$	
	Poisson	v [-]	0,333	
	Loss factor	η [-]	0,0001	
	Measured mass	M [kg]	1,12	
	Measured volume	V [m³]	$4{,}137\times10^{-4}$	
	Calculated Density	ρ [kg/m³]	2707,27	
	Width	b [mm]	60	
Cell 1	Thickness	h [mm]	10,15	2,20
	Length	l [mm]	60,34	49,22
Cell 2	Thickness	h [mm]	10.21	2,30
	Length	l [mm]	50,68	49,30
Cell 3	Thickness	h [mm]	10,12	2,25
	Length	l [mm]	50,65	49,28
Cell 4	Thickness	h [mm]	10,18	2,25
	Length	l [mm]	50,67	49,28
Cell 5	Thickness	h [mm]	10,16	2,29
	Length	l [mm]	50,68	49,28
Cell 6	Thickness	h [mm]	10,16	2,24
	Length	l [mm]	50,69	49,26
Cell 7	Thickness	h [mm]	10,13	2,19
	Length	l [mm]	50,72	49,31
Cell 8	Thickness	h [mm]	10,12	2.16
	Length	l [mm]	50,75	49,28
Cell 9	Thickness	h [mm]	10,15	1,98
	Length	l [mm]	50,34	49,28
Cell 10	Thickness	h [mm]	10,12	2.13
	Length	l [mm]	50,69	49,30
Cell 11	Thickness	h [mm]	10,11	-
	Length	l [mm]	56,32	-
	Thickness Mean (Standard Deviation)	h [mm]	10,14 (0,0304)	2,20 (0,0941)
	Cell Length Mean (Standard Deviation)	l [mm]	52,05 (3,2351)	49,28 (0,0251)
	Total Length	L [mm]	1065,32	

The geometrical data provided in Table 4.3 are sequentially measured for each cell. It means that the length of each cell is measured with respect to the end of previous segment end.

Firstly, to validate the experimental procedure, a continuous beam, with same width *b*, thickness *h* and length *L*, but without periodicities, is excited considering the same conditions as the experiment performed with the periodic beam. Figure 4.4 shows the frequency response functions obtained for this continuous beam and the numerical result obtained with Translation Matrix method.

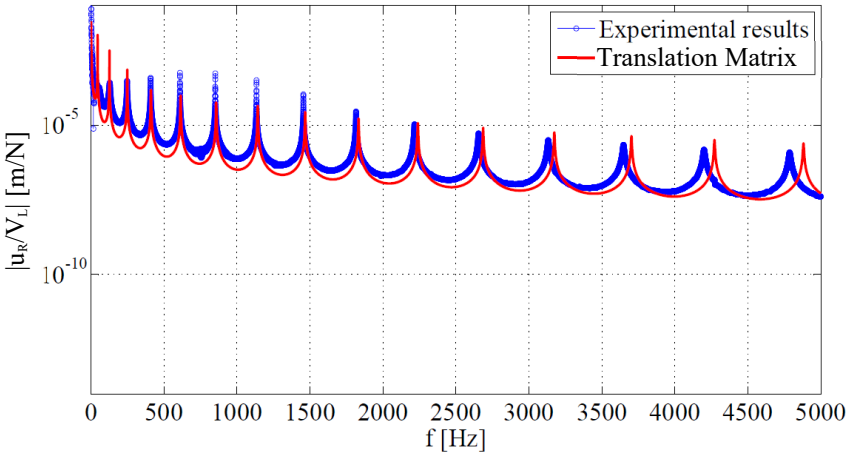

Figure 4.4 Frequency response function obtained experimentally for a free-free continuous beam.

In Figure 4.4, it is possible to observe that the numerical FRF fits well the experimental results in low-frequency range. However, the shear deformation and rotational inertia effect become evident for higher frequencies, which lead to conclude that a Timoshenko beam model must be used.

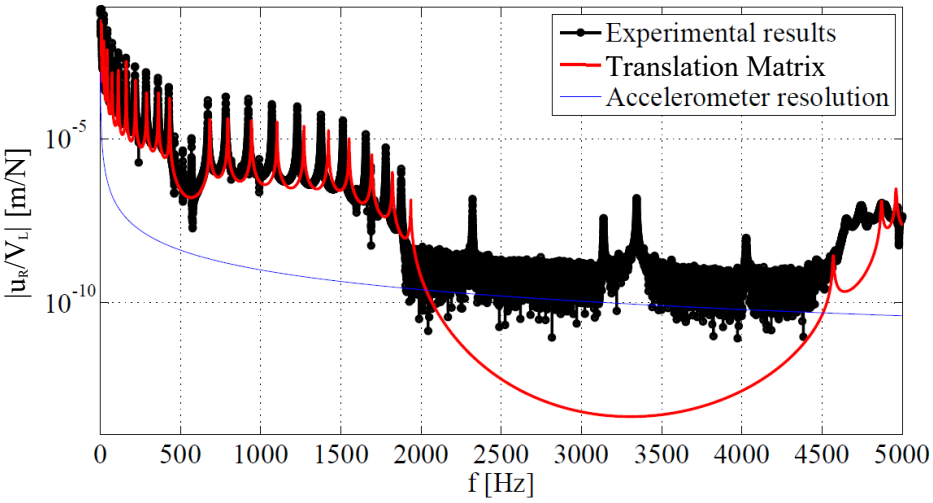

Figure 4.5 Frequency response function obtained experimentally for a free-free periodic beam with 10 stepped unit cells.

Figure 4.5 shows the FRF for a periodic beam with stepped unit cells. It is possible to observe that the region inside bandgaps is extremely sensitive and other resonant peaks appear inside this zone. Moreover, the accelerometer cannot measure the response inside this frequency band and the amplitude is limited by external noise. The red and blue thin curves represent the resolution that the accelerometer can measure. Therefore, there is an accelerometer resolution limitation to this kind of experiment involving periodic structures.

The appearance of these modes inside the attenuation zone can be explained in virtue of the impossibility to perfectly control the direction of the impact excitation force. Moreover, the accelerometer also has an angle deviation and it can measure small accelerations in other directions. Additionally, this slender beam can present other kinds of imperfections related to being bended or twisted.

4.4.1 Non localized modes inside the attenuation zone

Depending on the structure, unpredicted modes that are not considered in the used model can appear in virtue of the incapacity of perfectly applying appropriate boundary conditions (Junyi and Balint, 2015; Junyi *et al.*, 2016) or forces to excite only the desired motion, besides the fact that the beam is not perfectly straight. In this way, modes in different planes can be excited by changing the applied force characteristics. Even if small, a force component in other direction can excite other modes and it can be verified with numerical results presented in Figure 4.6. The four natural frequencies inside the attenuation zone are associated to one longitudinal mode (LM2) and three flexural modes (FM2, FM3 and FM4) on x-z plane. There are no torsion modes excited inside the bandgap for this experiment.

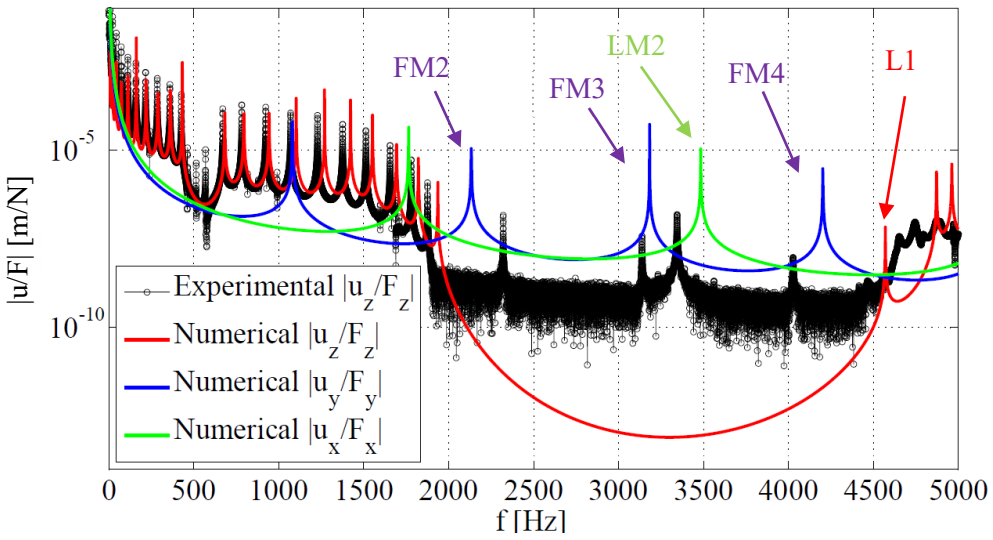

Figure 4.6 FRF with non-predicted resonance frequencies inside the attenuation zone.

Figure 4.6 also shows that the model also predicted a localized mode (L1) but it is not present in the experimental result because it may be detected in same magnitude as measurement noise.

A full-field measurement was done and the natural frequencies inside the BG were confirmed as longitudinal and flexural modes.

4.4.1.1 Considering variation on excitation and measument parameters

The variation of excitation and measurement parameters like position and measurement direction can excite other modes if a non-orthogonal excitation or measurement are used. To investigate this behavior, a study was performed using finite element model of the periodic beam and the applied force and the measured acceleration are considered inclined with two angles θ and φ. The first one in about the x-axis (yz plane) and the second one is about y-axis (xz plane). In other words, two rotations of the local coordinate system are applied, one around x-axis and the other around y-axis for the applied force on the left and displacement output on the right side of the beam.

Applying a moment as excitation, in this case, is the same as decentralize the point where the force is applied and suppress this vertical component in the middle, *e.g.*, by applying another in opposite direction. If the force position is considered as uncertain, it can creates the appearance of torsion modes. However, this study is not showed here.

Figure 4.7 shows the influence of the variation of angles θ and φ from one to four degrees.

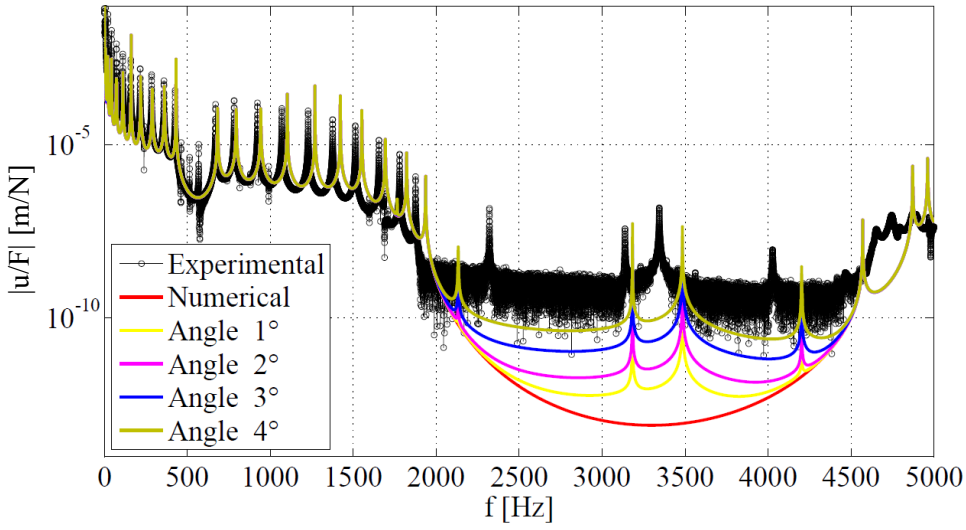

Figure 4.7 FRF with variation on exciting force angle and direction of measured displacement.

Figure 4.7 shows the influence of the variation of angles θ and φ from one to four degrees. It can be seen that as the angles values increase, more modes appear inside the attenuation zone in the frequency response function.

It is important to note that even for low disorientation values as one degree, the projected force can excite modes inside the bandgap that are related to other types of waves.

Therefore, it can be confirmed that these peaks are present because efforts cannot be applied perfectly perpendicular to the beam surface.

4.4.2 Robust bandgap and experimental FRFs

A probabilistic analysis, similar to those performed in Chapters 2 and 3, was performed considering the length of the first half-cell (l_1) as an uncertain variable. Table 5.3 shows that the standard deviation of this variable is 3,2351 mm (6,22 % of l_1 mean 52,05 mm). In this case, since this periodic structure has 10 cells plus 1 half-cell, a Monte Carlo Simulation with Latin hypercube is performed considering 11 random variables with Gaussian probability density function with mean 52,05 mm and standard deviation 3.2351 mm (6.22 % of mean). The detailed explanation is similar to that presented in Chapters 2 and 3, and is not repeated here.

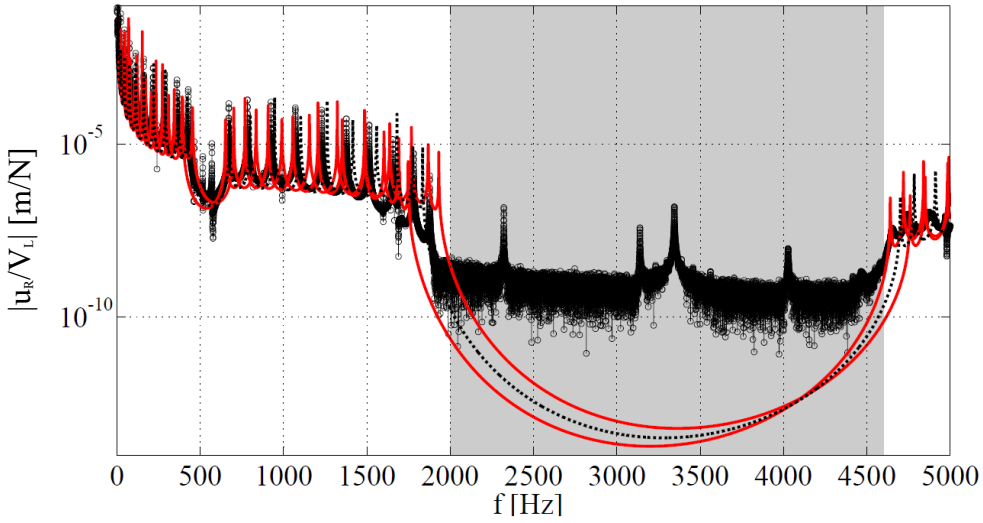

Figure 4.8 FRF with envelope confidence interval, experimental results and robust bandgap for calculated standard deviation.

Figure 4.8 shows the experimental results with the bandgap envelope for 95% confidence interval and the robust bandgap, indicated by the gray region, considering 6.22 % of the mean, *i.e.* the standard deviation, as the variatioan coefficient.

It is possible to verify that the robust bandgap calculated considering the mean and standard deviation of each half-cell as input uncertain variables agrees well with the experimental bandgap region presented in the FRF.

4.5 Partial conclusion

Periodic beams are investigated experimentally and numerically in this chapter. Firstly, a Translation Matrix method with six degrees of freedom is proposed for assembling transfer matrices for longitudinal, flexural in two planes and torsion. Then, dispersion constants for a continuous beam and for a periodic beam with stepped unit cell are observed for six types of waves: four flexural in two planes (two evanescent and two propagative), one longitudinal and one torsional (shear). There is a partial bandgap for flexural waves in the periodic structure. Subsequently, Translation Matrix method is verified for flexural waves by comparing frequency response functions to the counterparts obtained with a finite element model using 40, 120 and 200 finite elements. As the number of finite elements increase, the calculated errors are reduced and it was concluded that the Translation Matrix method present satisfactory accuracy for 200 finite elements. An experimental analysis is performed and its results are compared to numerical results for flexural waves. In low frequencies, the numerical frequency response function agree well with experimental results. Inside the bandgap region, is not possible to measure the magnitude and most part of bandgap region is affected by measurement noise.

Four resonant peaks appear inside the attenuation zone and they are not localized modes. The numerical model predicts one localized mode near the upper border but it is not possible to be identify it experimentally because the noise presented the same magnitude.

A probabilistic analysis was performed using the half-cell length of first segment for each cell as random variable with Gaussian probabilistic density function and a robust bandgap is obtained for this kind of uncertainty. The lower bound of this large bandgap seems coherent with experimental results.

The four modes excited inside the stop band are investigated and their values are found to be close to three flexural modes in the other plane xz and one longitudinal on axis x. A study corresponding to the angles of excitation force and displacement measurement is done. It was possible to conclude that, for even for small variations on the values of these angles, other modes can be excited and the low magnitude inside the bandgap zone favors their appearance.

This page intentionally left blank

Chapter 5 Truss structures

5.1 Introduction

Smart and periodic structures have received the attention of researchers by virtue of their great potential. These structures have powerful properties like adaptiveness and the ability to operate as mechanical filters.

However, the presence of uncertainties must be taken into account to guarantee robustness. Thus, in this chapter, a finite element model is proposed to elucidate the importance of stochastic aspects and to present the concept of robust frequency bandgap for smart trusses. The smart components consist of piezoelectric transducers connected to resonant circuits in a tridimensional truss unit cell. Although this truss presents three dimensions, the wave propagation is unidirectional. The periodic part is the replication of this cell to assemble the final structure. Floquet-Bloch conditions are used to model the infinite representation. Then, a Monte Carlo Simulation is carried out and the bandgap bounds are analyzed considering frequency responses and dispersion diagrams, the goal being to evaluate the influence of uncertainties affecting the prediction of the attenuation zones.

Detailed reviews about these periodic structures can be found in (Mead, 1996) and some perspectives are drawn in (Hussein *et al.*, 2014). One of these perspectives is related to adaptiveness and tunable frequency bandgaps.

Smart materials and structures capacity of self-sensing and self-changing to adapt to new conditions according to design requirements is their most important characteristic. Some fundamental aspects of these intriguing structures can be found in (Leo, 2007). Among others, periodic and smart structures are good candidates to help the resolution of complex vibration problems. Interesting reviews are proposed in (Thorp *et al.*, 2011) and (Spadoni *et al.*, 2009).

Piezoelectric (PZT) actuators (Leo, 2007; Hagood and Von Flotow, 1991; Preumont, 2004) are used in the numerical example of this study. When they are coupled with electric circuits, the dynamics of the structure becomes coupled with the dynamics of the electric circuit. This concept can be used for structural vibration control and it is referred to as “piezoelectric shunt” in the literature. The principle behind this strategy is that the vibrational energy is transformed into electric energy through the direct piezoelectric effect and is transferred to the circuit where it is partially dissipated and/or dispersed. Among the types of electric circuit, one composed by electrical resistance and inductance (RL) is known as resonant circuit and it is probably the

most popular because of their simplicity and efficacy (Hagood and Von Flotow, 1991; Sales *et al.*, 2013). Such circuits comprise an inductor and a resistor that are connected to the piezoelectric transducer that is assimilated to a capacitor, thus forming an RLC circuit. When coupled to a dynamic system, this device operates similarly to a dynamic vibration absorber (DVA). This kind of mechanism creates resonant bandgaps if placed periodically in a structure. More information about DVAs can be found in (Den Hartog, 1956; Korenev and Reznikov, 1993; Rade and Steffen, 2000). Distributing these devices may lead to multimodal control (dell'Isola *et al.*, 2004).

The main advantage of using piezoelectric actuators, rather than DVAs, is the characteristic of no addition of significant mass to the main structure and the convenience of electronically tuning without changing mechanical properties. Moreover, these circuits can be redesigned and unusual behaviors can be induced. One example of this is the negative capacitance shunting (Park and Baz, 2005), which aims at removing the intrinsic capacitive effect of the piezoelectric transducer (Marneffe and Preumont, 2008). This may be combined with resonant circuits (Casadei *et al.*, 2012), opening the way to new strategies with wideband efficiency (Lossouarn *et al*., 2015; Tateo *et al*., 2014a; Tateo *et al*., 2014b).

Reference (Signorelli and Von Flotow, 1988) show the wave propagation behavior in truss structures by using beam finite elements and the Transfer Matrix method. This sort of structure also has the lightweightiness as its major characteristic. In virtue of this, the use of piezoelectric actuators in these lattice like structures seems to be a good choice because it favors the weight requirements. Nevertheless, uncertainty and robustness analysis of truss structures are rare in literature. Near-periodic structures, defects, impurities on periodic structures and the localization phenomena are well detailed in (Lust *et al.*, 1995; Wu *et al.*, 2014; Mester and Benaroya, 1995), but robustness analyses are scarce.

In this chapter, one addresses the robustness of repetitive truss structures whose attenuation zones are created and passively controlled by using piezoelectric stack actuators associated with electrical shunt circuits (Leo, 2007; Hagood and Von Flotow, 1991. The finite element method is used to find the equation of motion for unit cells (Orris and Petyt, 1974; Mace and Manconi, 2008) which contain a piezoelectric stack actuator connected to this circuit. Just like DVAs, shunt circuits can be tuned, which means that the values of their electric parameters must be precisely chosen for vibration attenuation in a narrow frequency band. However, the characteristic values of electronic components are prone to variability, due to manufacturing process and temperature, which can lead to mistuning and, consequently, decrease of the control performance.

In this scenario, it becomes essential to evaluate the probability that the system will comply with the design requirements, given the probability density functions ascribed to the uncertain variables considered. For that, three different cases are analyzed based on typical operation and performance requirements. Uncertainties in the values of some model parameters (mass of the joints and inductance of the shunt circuit) are modeled as Gaussian random variables. Next, a Monte Carlo Simulation (Melchers, 1999; Lemaire, 2009; Haldar and Mahadevan, 2000) is performed considering infinite and finite models by using the dispersion constants and frequency response function bandgaps data as output variables. The uncertainty level is varied

by increasing the standard deviation of input variables as a percentage of their means. Subsequently, the results are presented and discussed.

Likewise, the consequences of increasing the uncertainty level are evaluated and a comparison with another truss model to investigate the inner resonances is performed.

5.2 Methodology for truss structures

In the following, on considers a simple truss unit cell, composed of 12 longitudinal rods, as ilustrated in Figure 5.1. The embedded smart devices will be described in the next section.

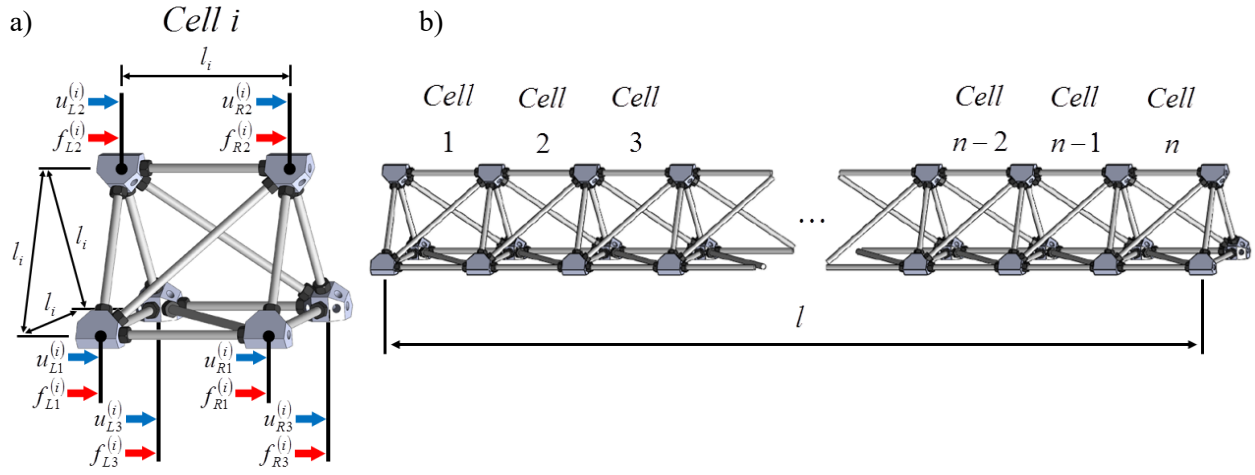

Figure 5.1 (a) 3D truss unit cell and (b) its finite model.

Firstly, for the sake of simplicity and to reduce the computational cost, the repetitive truss structure in Figure 5.1 is composed of rod finite elements with 2 nodes and 3 degrees-of-freedom (dof) per node. This structure has 3 boundary nodes on each side, and the relevant properties of the rods are cross section area A, Young's modulus E, mass density ρ. Moreover, l_i denotes the length of the *i-th* cell, while l is the total length of a structure with n cells.

5.2.1 Discrete systems comparison

As seen in previous chapters, each type of wave has its own branch in the dispersion diagram. Numerical tools provide discrete evaluation of these curves and tracking these branches is easy only on simple structures. For more complex structures, a simple wave type can be tracked in many different branches. When a bandgap zone is open, for Bragg's, local resonance or coupling modes, the understanding of both propagation constants is not easy. Figures 5.2(b) and 5.2(c) show the dispersion diagrams for the unit cell of Figure 5.2(a) which does not have concentrated masses on the nodes. Although this truss structure present periodic spatial characteristics, the imaginary part of the dispersion constant does not present bandgaps. Moreover, the propagation constant does not present information in an easily understandable format as presented in previous chapters.

Figure 5.3 presents equivalent results for a unit cell with concentrated masses (Spadoni and Ruzzene, 2006; Taniker and Yilmaz, 2013) on its nodes. It is possible to verify, comparing both figures, that the curves

of dispersion constants shifted to lower frequencies and the same tendency observed for the structures considered in previous chapters are obtained. Such as the discrete spring-mass unit cell on Chapter 2, the number of solutions on imaginary part of dispersion constants is limited because of the finite number of dofs of the unit cell. Therefore, the region after 6500 Hz is not considered as a bandgap for a real structure.

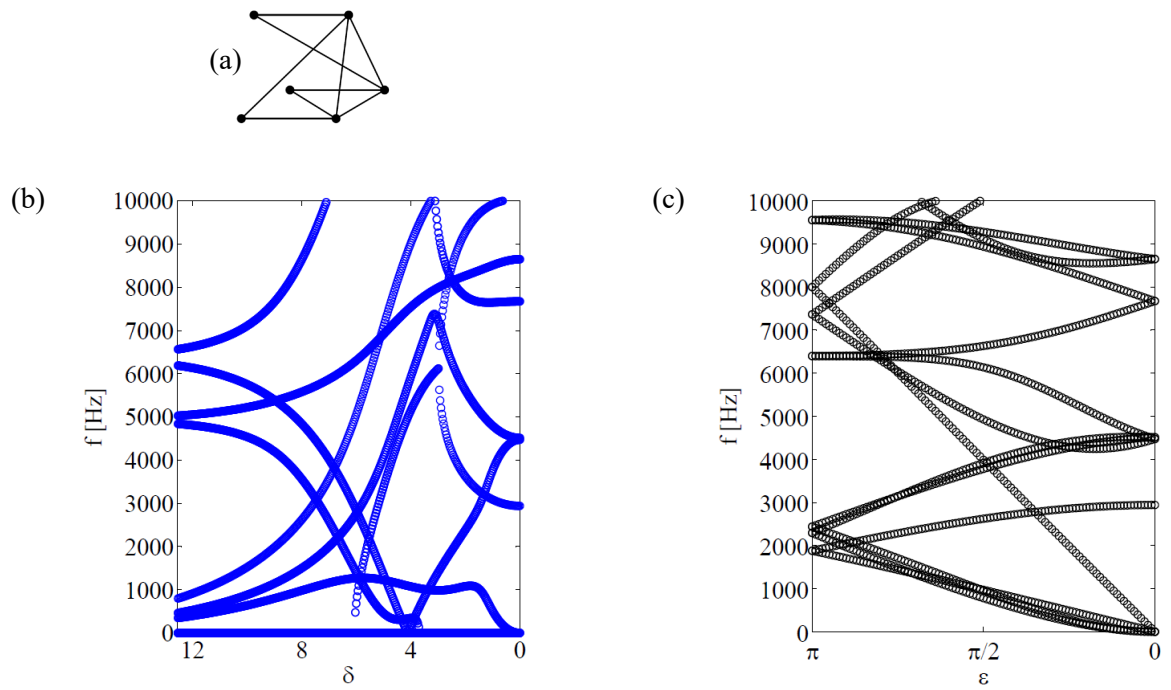

Figure 5.2 (b) Attenuation and (c) phase constants of truss unit cell (a) without concentrated mass on nodes.

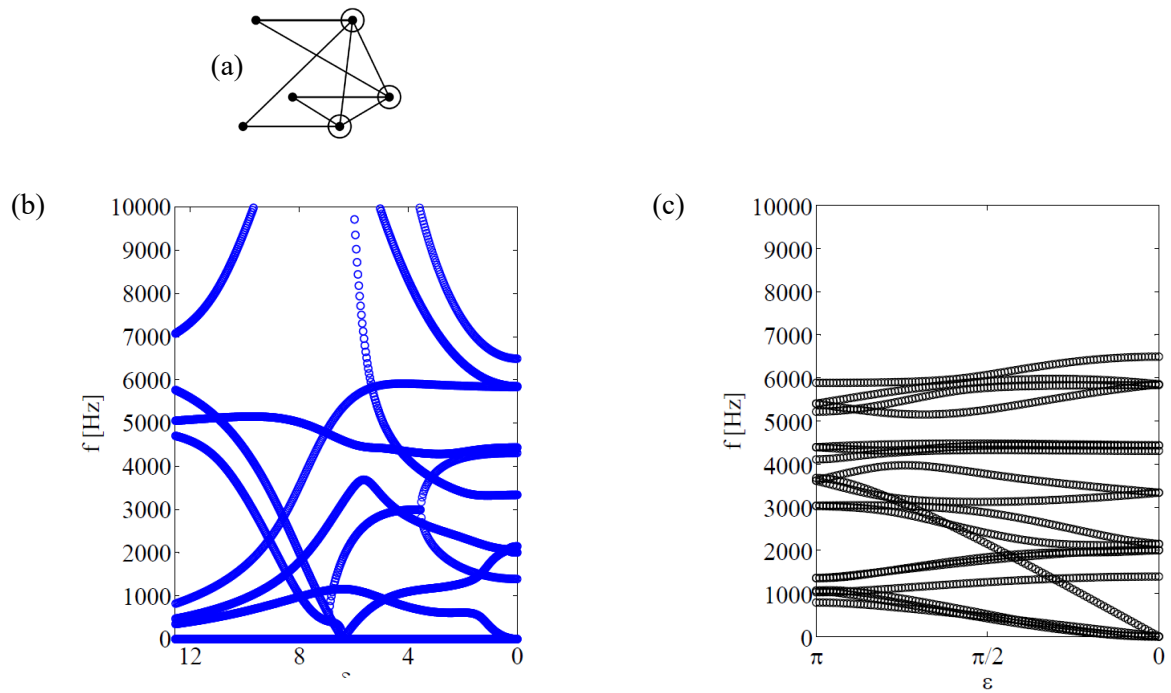

Figure 5.3 (b) Attenuation and (c) phase constants of truss unit cell (a) with concentrated mass on nodes.

5.3 First structure: smart rod finite element truss

5.3.1 Smart cell: Constitutive equations of linear piezoelectricity

The fundaments of piezoelectric material modelling is explained are first introduced. These materials produce an electrical output when a mechanical strain is imposed. This is called direct piezoelectric effect. Oppositely, a mechanical strain can also be induced by applying an electrical signal. This is the inverse piezoelectric effect. The electromechanical coupling is expressed mathematically by the following constitutive equations

$$\begin{Bmatrix} D \\ S \end{Bmatrix} = \begin{bmatrix} \varepsilon_{33}^{T} & d_{33} \\ d_{33} & s^{E} \end{bmatrix} \begin{Bmatrix} E \\ T \end{Bmatrix}, \tag{5.1}$$

where D and S are the electric displacement and the mechanical strain, E and T are the electrical field and mechanical stress. The material properties $\varepsilon_{33}^{T}(F/m)$, d_{33} (C/N or V/m) and s^{E} (m²/N) are, respectively, the dielectric permittivity coefficient, piezoelectric strain coefficient and mechanical compliance of the piezoelectric material. The indexes E and T are used to designate the properties measured in short-circuit (constant electric field) and stress-free conditions, respectively, while subscript 3 indicates the direction along the axis of piezoelectric material polarization, which is one of the most common operating modes of piezoelectric devices. These characteristics are used to model the semi-active finite element present on the structure considered in this work.

5.3.1.1 Smart unit cell with shunt circuit

This section presents the finite element model of the three-dimensional truss cell shown in Figure 5.4. This unit cell is composed by 6 nodes, 9 passive elements and 3 active elements. The nodes displacement are connected and, as long as the rotations are not coupled, the joint has a spherical function. Each of the active members is considered as being composed of a stack-type actuator placed between two passive segments. The actuator is assumed to be composed of piezoelectric discs poled in the axial direction (direction 3), wired in such a way that those discs are electrically connected in parallel.

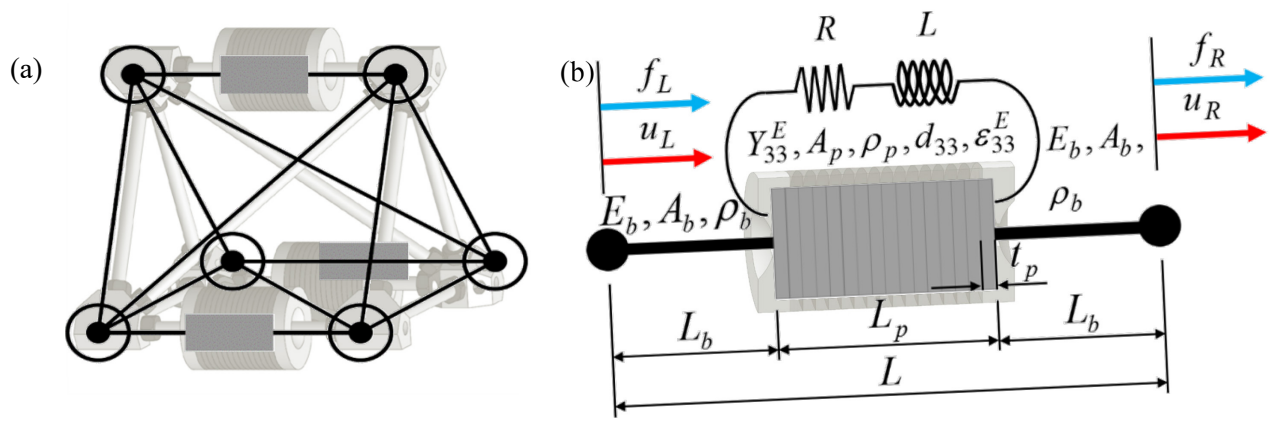

Figure 5.4 (a) Smart unit cell and (b) its piezoelectric stack actuator described as a finite element model.

As indicated in Figure 5.4, E_b (N/m^2), A_b (m^2) and ρ_b (kg/m) are the Young's modulus, cross-section area and linear mass density of the passive members, respectively. The others properties, Y_{33}^E (N/m^2), A_p (m^2), t_p (m) and ρ_p (kg/m^3) are the Young's modulus, cross-section area, thickness of the piezoelectric discs and linear mass density of the piezoelectric material of the active members. The physical and geometrical properties of the main structure and the actuator are provided in Table 5.1, in which subscripts *b* and *p* indicate the properties related to the metallic and piezoelectric material.

Table 5.1 Properties of the smart periodic cells.

Property	Unit	Symbol	Steel (*b*)	PZT-5H (*p*)
Young's modulus	$[N/m^2]$	E_i and Y_{33}^E	2.1×10^{11}	60.0×10^{9}
Density	$[kg/m^3]$	ρ_i, ρ_b or ρ_p	7860.0	7860.0
Cross section area	$[m^2]$	A_i, A_b or A_p	25.0×10^{-6}	27.5×10^{-6}
Bar lengths (Cell length)	$[m]$	L_b or L_p (L or l_i)	0.033 (0.1)	0.033 (0.1)
Piezoelectric strain coefficient	$[C/N]$ or $[V/m]$	d_{33}	-	650.0×10^{-12}
Dielectric permittivity coefficient	$[F/m]$	ε_{33}^T	-	33.0×10^{-9}

As detailed in references (Leo, 2007; Hagood and Von Flotow, 1991), neglecting damping, the finite element model of the electromechanical system can be written as:

$$\mathbf{M}\ddot{\mathbf{U}}(t)+\mathbf{K}\mathbf{U}(t)-\widetilde{\mathbf{K}}V(t)=\mathbf{F}(t), \tag{5.2}$$

$$\widetilde{\mathbf{K}}\mathbf{U}(t)+\mathbf{\Gamma}V(t)=Q(t), \tag{5.3}$$

where $\mathbf{M}$ is the mass matrix, $\mathbf{K}$ is the stiffness matrix, $\widetilde{\mathbf{K}}$ is the electromechanical coupling matrix, $\mathbf{F}$ is the vector of external loads, $\mathbf{\Gamma}$ is the matrix of dielectric permittivity, $\mathbf{U}$ is the vector of mechanical degrees of freedom, $Q(t)$ is the electric charge and $V(t)$ is the voltage across the electrodes of the piezoelectric patches. If a RL shunt circuit is connected to the piezo stack, the voltage and the electrical charge are linked by

$$V(t) = R\dot{Q}(t) + L\ddot{Q}(t). \tag{5.4}$$

Associating Eqs. (5.2), (5.3) and (5.4), the electromechanical equations of motion are found under the form:

$$\overline{\mathbf{M}}\,\ddot{\mathbf{Z}}(t) + \overline{\mathbf{C}}\dot{\mathbf{Z}}(t) + \overline{\mathbf{K}}\mathbf{Z}(t) = \overline{\mathbf{F}}(t), \tag{5.5}$$

where $\mathbf{Z}(t)$, $\overline{\mathbf{M}}$, $\overline{\mathbf{C}}$ and $\overline{\mathbf{K}}$ are equal to $\left[\mathbf{U}(t) \;\; Q(t)\right]^T$, $\left[\mathbf{M} \;\; -L\widetilde{\mathbf{K}};\mathbf{0} \;\; L\boldsymbol{\Gamma}\right]$, $\left[\mathbf{0} \;\; -R\widetilde{\mathbf{K}};\mathbf{0} \;\; R\boldsymbol{\Gamma}\right]$ and $\left[\mathbf{K} \;\; \mathbf{0};\widetilde{\mathbf{K}} \;\; -\mathbf{I}\right]$, respectively, and $\overline{\mathbf{F}}(t)$ is the load vector. An equivalent equation of motion of a truss model using the admittance of the shunt circuit can be found in (Preumont, 2004).

5.3.1.2 Tuning a resonant RLC circuit

Figure 5.4(b) illustrates a piezoelectric transducer connected to a resonant (RL) shunt circuit and bonded to a host vibrating structure. Similarly to a dynamic vibration absorbers, the resonant shunt circuits must be tuned, which means that the values of the electrical resistance and inductance parameters must be accurately determined for the attenuation of vibrations of the host structure in a given range of frequencies. According to Hagood and Von Flotow (1991), the electromechanical coupling coefficient Δ plays the same role as the mass ratio in tuning a DVA. Indeed, this coefficient can be approximated as follows: $\Delta^2 = \left(\left(\omega_n^D\right)^2 - \left(\omega_n^E\right)^2\right) \Big/ \left(\omega_n^E\right)^2$ where ω_n^D and ω_n^E are the n-th natural frequencies in open and closed circuit, respectively. Knowing the value of Δ, one can calculate the optimum values of resistance R_{opt} and inductance L_{opt} according to: $r_{opt} = \left(\sqrt{2}\Delta\right) \Big/ \left(1 + \Delta^2\right)$, $R_{opt} = r_{opt} \Big/ \left(C^S \omega_n^E\right)$, $\delta_{opt} = \sqrt{1 + \Delta^2}$ and $L_{opt} = \left(\left(\omega_n^E\right)^2 C^S\right)^{-1}$. Herein, the electrical resistance is considered as null and no optimal values are used to tune because the bandgap border lose definition when damping is considered. Thus, equation (5.6) shows how the inductance value is obtained for a specific tuning frequency:

$$L = 1 \Big/ \omega_n^2 C^S. \tag{5.6}$$

where C^S is the capacitance of piezoelectric actuator and ω_n the tuning frequency. In practical conditions, the values of the electric characteristics of the shunt circuit are inevitably affected by uncertainties resulting from material composition, manufacturing process and temperature variations. Such uncertainties can lead to mistuning of the shunt circuit and, as a result, deterioration of the performance of the damping/resonating device. In the case of periodic structures, they influence the bandgap bounds and, for a strong impedance

mismatch in mechanical and electrical domains, natural frequencies can appear inside the bandgap and, consequently, decrease the attenuation zone efficacy.

5.3.2 Frequency response function and dispersion diagrams

There are several ways to create impedance mismatch in truss structures to create Bragg's bandgaps or to tune the shunt circuit with piezoelectric stack to create local resonance bandgaps. Accordingly, one manner is to increase the mass value of the joints and another is to change the inductance value to tune a specific frequency. To give a sense on the influence of the joint mass and shunt inductance, 8 scenarios are compared by observing the dispersion diagrams and frequency responses, which are illustrated in Figure 5.5.

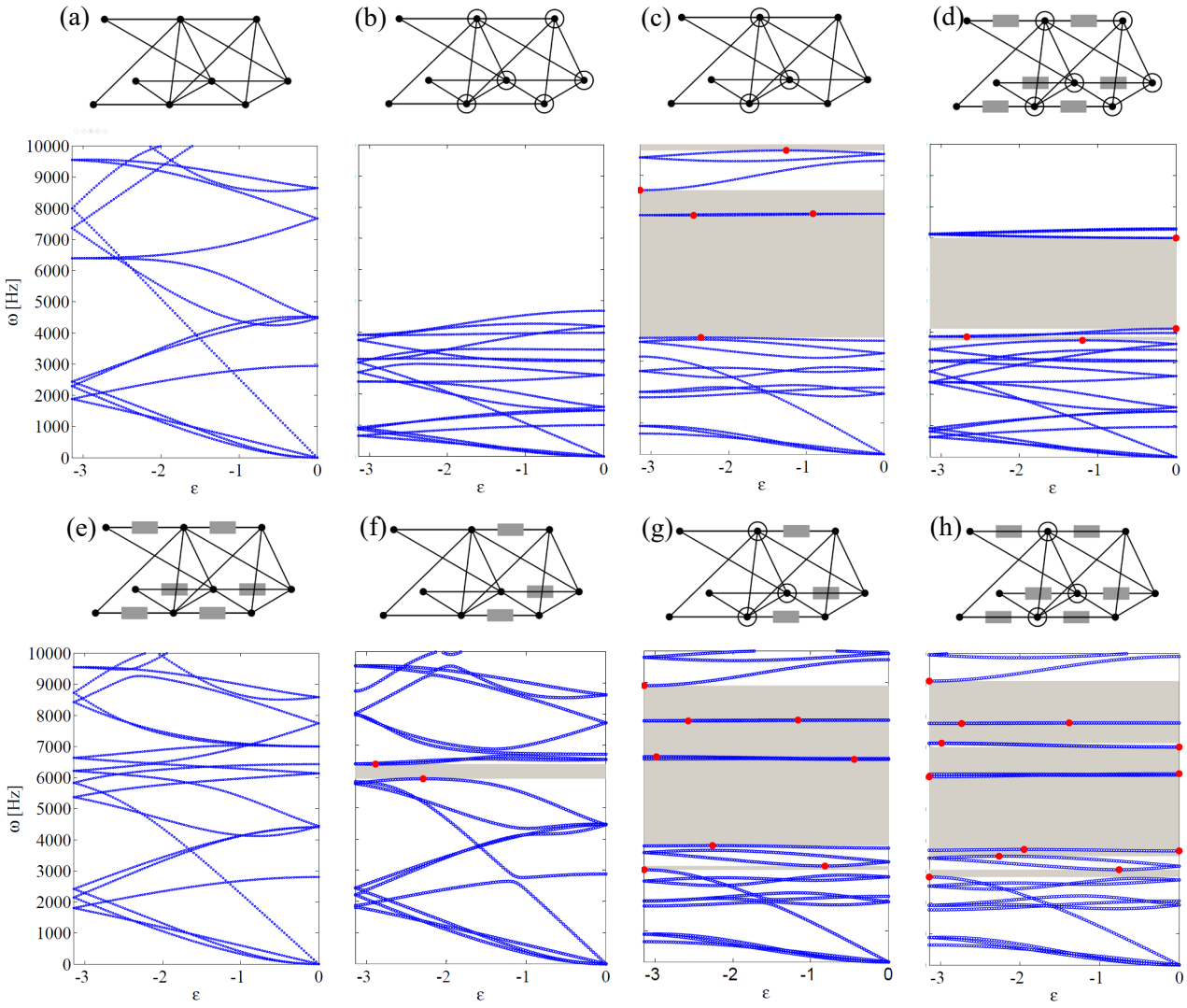

Figure 5.5 Considered unit cells (a), (b), (c), (d), (e), (f), (g) and (h) with their respective dispersion diagrams.

Equation (5.5) can be solved considering a harmonic solution to obtain the frequency response function (FRF) in equation (5.7). Moreover, equation (5.8) is achieved by solving equation (5.5) considering infinite periodic boundary conditions of continuity and equilibrium (Floquet, 1883).

$$\overline{\mathbf{H}}(\omega) = \left(-\omega^2\overline{\mathbf{M}} + j\omega\overline{\mathbf{C}} + \overline{\mathbf{K}}\right)^{-1}, \tag{5.7}$$

$$\left[\overline{\mathbf{K}}^{(r)}(\mu) + j\omega\overline{\mathbf{C}}^{(r)} - \omega^2\overline{\mathbf{M}}^{(r)}(\mu)\right]\ \mathbf{U}^{(r)}(\mu) = 0 \tag{5.8}$$

where (r) means reduced matrices considering boundary conditions. Figures 5.5(a) to 5.5(h) show the added mass and actuator position with their corresponding imaginary parts of dispersion constants. Transversal and longitudinal wave modes are not tracked and the bandgaps highlighted in gray are valid for these two types of waves. The red dots indicate the bandgap bounds. It is important to mention that as the model of one cell has 18 and 21 *dofs* (3 dofs per node and 3 more electric dofs for active members), considering reduced matrices (r), the same number of mode branches are found. As the unit cell does not represent all *dofs* that one finite structure can have, the area after the last branch is not considered as an attenuation zone and the respective areas are not exposed in these diagrams. Figure 5.6 shows the frequency responses by considering a transversal (x or y) and longitudinal (z) excitation on the first cell node on the left and observing the response of equivalent node of the last cell for a finite structure with 10 cells.

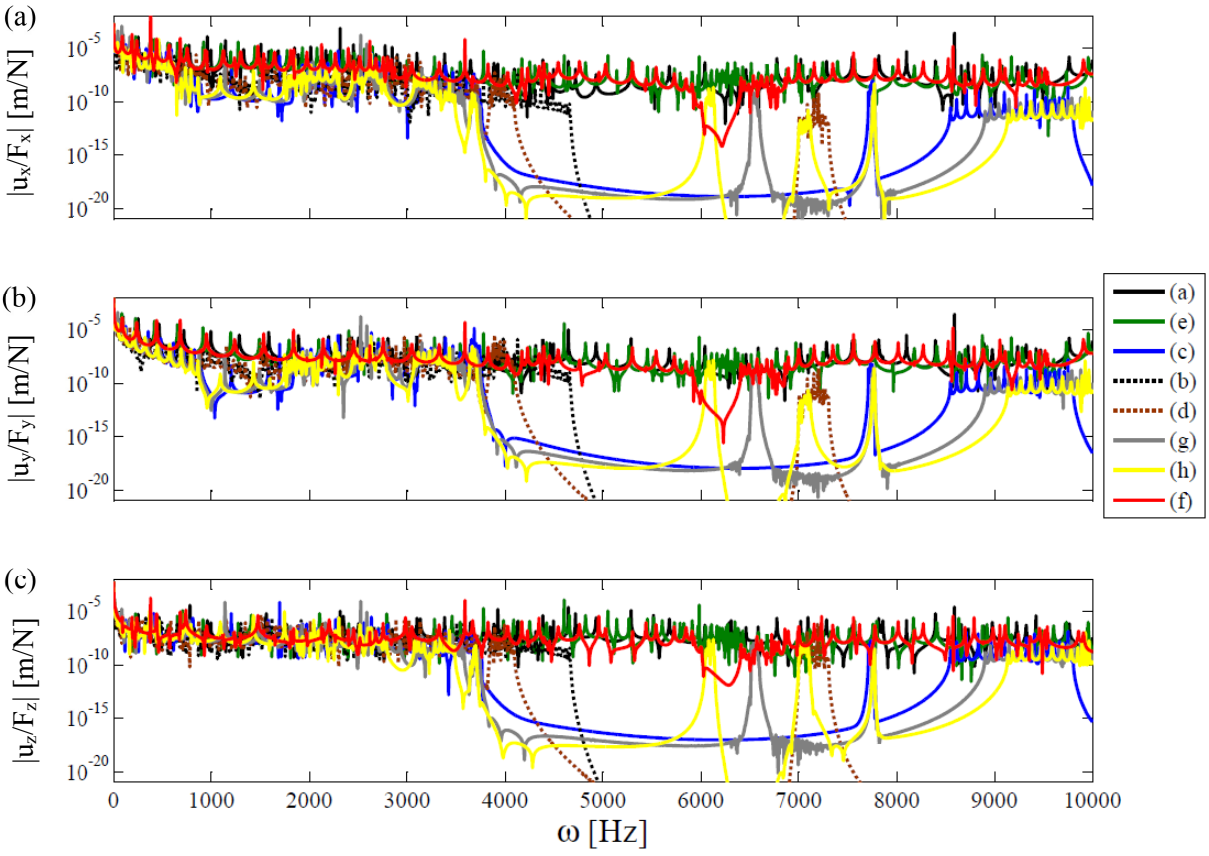

Figure 5.6 (a), (b) and (c) frequency responses of 8 scenarios periodic finite structures with 10 cells by exciting the firt node on direction x, y and z and observeing the corresponding dofs on the last unit cell.

The joint mass (m_a) is equal to 0.3 kg and the value of the inductance (L) to tune to a 7000 Hz, considering equation (6.6) is 0.1084 H. Some configurations does not exhibit the stop band corresponding to local resonance because the impedance mismatch and the anti-resonances were not strong enough to open a bandgap.

It is possible to observe that infinite and finite models have the same bandgaps, as can be verified by comparing Figures 5.5 and 5.6. Some important aspects can be observed. Firstly, the models without joint mass and piezoelectric actuator have no band gaps (Figure 5.5(a)). The same can be observed by adding mass in all joints or adding actuators as shown in Figures 5.5(b) and 5.5(e). Adding mass to joints, or considering the actuators in half-cell, creates attenuation zones as seen in Figures 5.5(c) and 5.5(f). By comparing these diagrams, a larger bandgap is found in the case of added mass and a deeper one with added mass and PZT in shunt circuit. It is similar to the added mass and mass-spring effects (Clayes *et al.*, 2013).

Figures 5.5(d), 5.5(g) and 5.5(h) are the combination of the others. The bandgap width is increased by combining added masses and actuators in scenarios of Figures 5.5(g) and 5.5(h). Uncertainties can drastically change these bandgaps behavior, as show in the next section.

5.3.3 Monte Carlo Simulation and localization phenomena

The localization phenomenon can be briefly explained as normal mode that is confined in a specific region of the structure. As the number of cells tends increases, the influence of this mode diminishes. Consequently, it does not appear in the infinite model. As already mentioned in Chapter 2, it is explained due to the stronger impedance mismatch compared to other cells. This phenomenon is worthy of exploration since it enables to reduce the variation of bandgap borders.

This kind of event in a Monte Carlo Sampling adds robustness to the bandgap behavior in terms of borders variation but it becomes hard to observe the amplitude on FRF inside bandgaps zones and to identify the effective attenuation zones. Consequently, a robust interval confidence envelope will not take into account the localization phenomena since the worst configuration may take part in any cell in a random analysis.

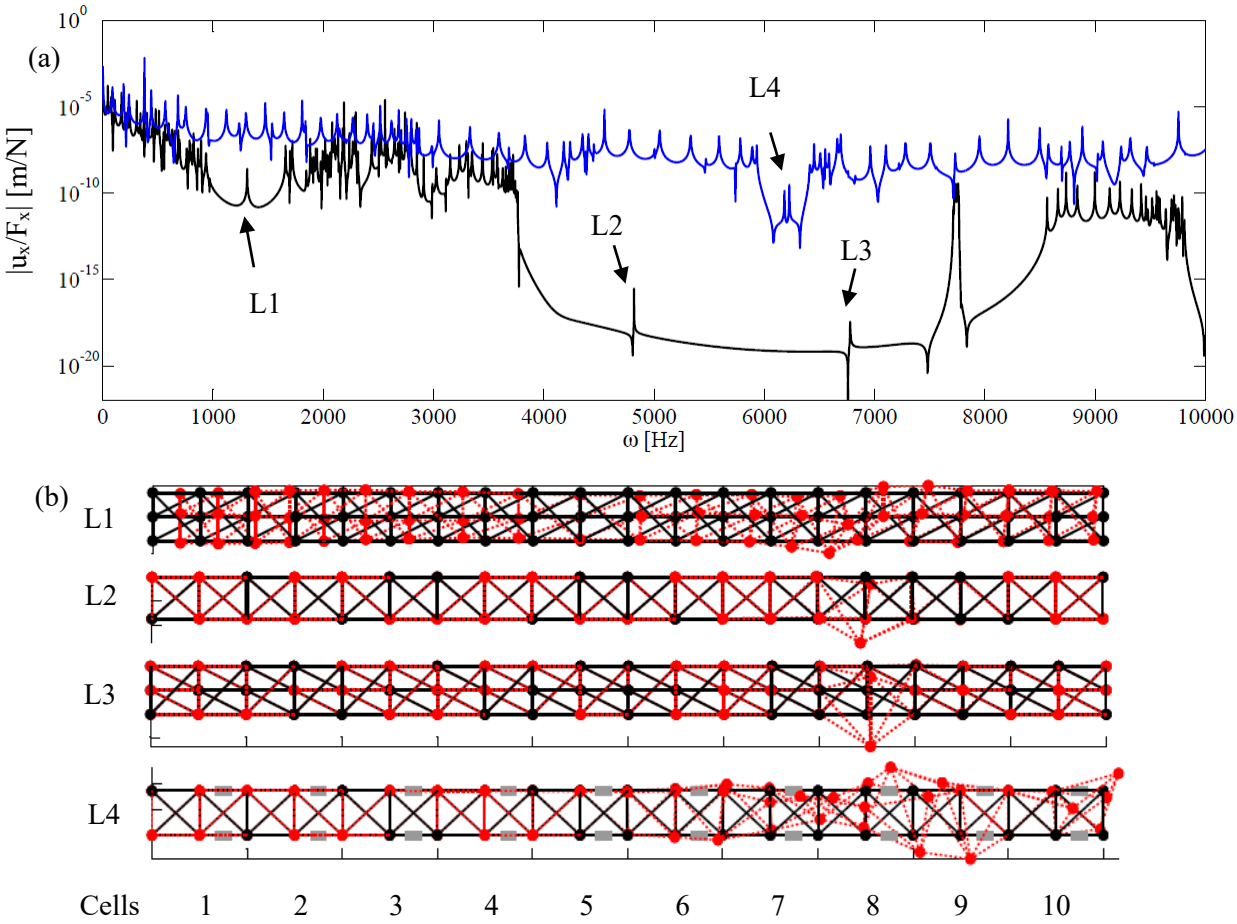

Figure 5.7 (a) FRFs with localization phenomena L1, L2, L3 and L4 and (b) their corresponding mode shape.

Figure 5.7(a) shows two FRFs considering a strong mismatch between one or two cells and the others in the same structure. L1, L2 and L3 illustrate the localization phenomena by adding a mass of 1 kg on dofs located in cell 8. L4 is the same but by changing the inductance of cells 8 and 9 to 0.001 H. Figure 5.7(b) depicts their respective mode shapes, and it can be observed that the displacements of nodes in these places are higher than the other positions of finite structure.

5.3.4 Probabilistic Analysis

In practice, it is not easy to design locally or to modulate periodically the inertia and the stiffness of a mechanical structure. Normally, properties as Young's modulus and density do not vary considerably if the material comes from same batch. Therefore, the principal source of uncertainties are the imperfections or defects caused by the manufacturing process. Accordingly, Figures 5.5(c), (f) and (h) illustrate the three situations of interest in which the added joint mass and inductance values are stochastically analyzed. Table 5.1 shows the properties of the truss unit cell for the numerical example.

A robustness analysis is employed for this periodic structure with the goal of estimating a robust bandgap. For this case, to get closer to reality, the variables of each cell should be independent. For the sake of comparison, infinite and finite models are used in this probabilistic analysis. To realize this investigation, for each standard deviation of random input variable (RV), a convergence of Monte Carlo Simulation is achieved and the outputs are obtained. The band gap edges are the outputs. For infinite structures analyses, Figures 5.5 show an illustration of these variables where the red dots are the bounds for the infinite structure. For finite structures, a specified magnitude in the FRF, defined according to an observable bandgap that is different for each case, is used as a threshold for obtaining the bandgap limits for a finite structure. The stochastic properties of the input random variables are shown in Table 5.2.

Table 5.2 Probabilistic variables and their distributions.

	Variables	**Distribution**	**Mean** (μ)	**Standard Deviation** (σ)
X_1	m_a $[kg]$	Normal (Gaussian)	0.3	$\gamma \times \mu_{X_1}$
X_2	L $[H]$	Normal (Gaussian)	0.1084	$\gamma \times \mu_{X_2}$

Again, using the same technique as in previous chapters, two different cases are considered for each of the three scenarios of Figures 5.5(c), 5.5(f) and 5.5(g):

- a single uncertain variable is associated repeatedly to each cell and, consequently, the structure remains periodic (infinite model);
- all 10 cells are independent from the uncertainty point of view (the structure is not perfectly periodic anymore, meaning quasiperiodicity).

For both cases, FE models are considered. To quantify and increase gradually the value of random variables, a stochastic coefficient γ is used. It permits the variation of uncertainty level, given by the standard deviation, which is obtained from a percentage of probability distribution mean, according to $\sigma_{X_n} = \gamma \times \mu_{X_n}$.

The variation coefficient γ varies from 2 % to 20 % with a step of 2 % for this numerical example. Then, for each considered value, a Monte Carlo Simulation with Latin Hypercube is performed until its convergence (number of samples around 5000). Considering a Normal (Gaussian) distribution with 95% of confidence level envelope, the output standard deviation value must multiplied by 1.96 to obtain the interval in which the output samples have 95% of probability to be in.

5.3.5 Numerical results

Figure 5.8 shows the envelope of the frequency band gaps for the three considered scenarios. Figures 5.8 (a), 5.8(b) and 5.8(c) for infinite model are obtained from the imaginary part of propagation constant,

considering 1 RV (strictly periodic structure), and Figures 5.8(d), 5.8(e) and 5.8(f) for finite model are obtained from frequency responses with 10 RV (quasi-periodic structure).

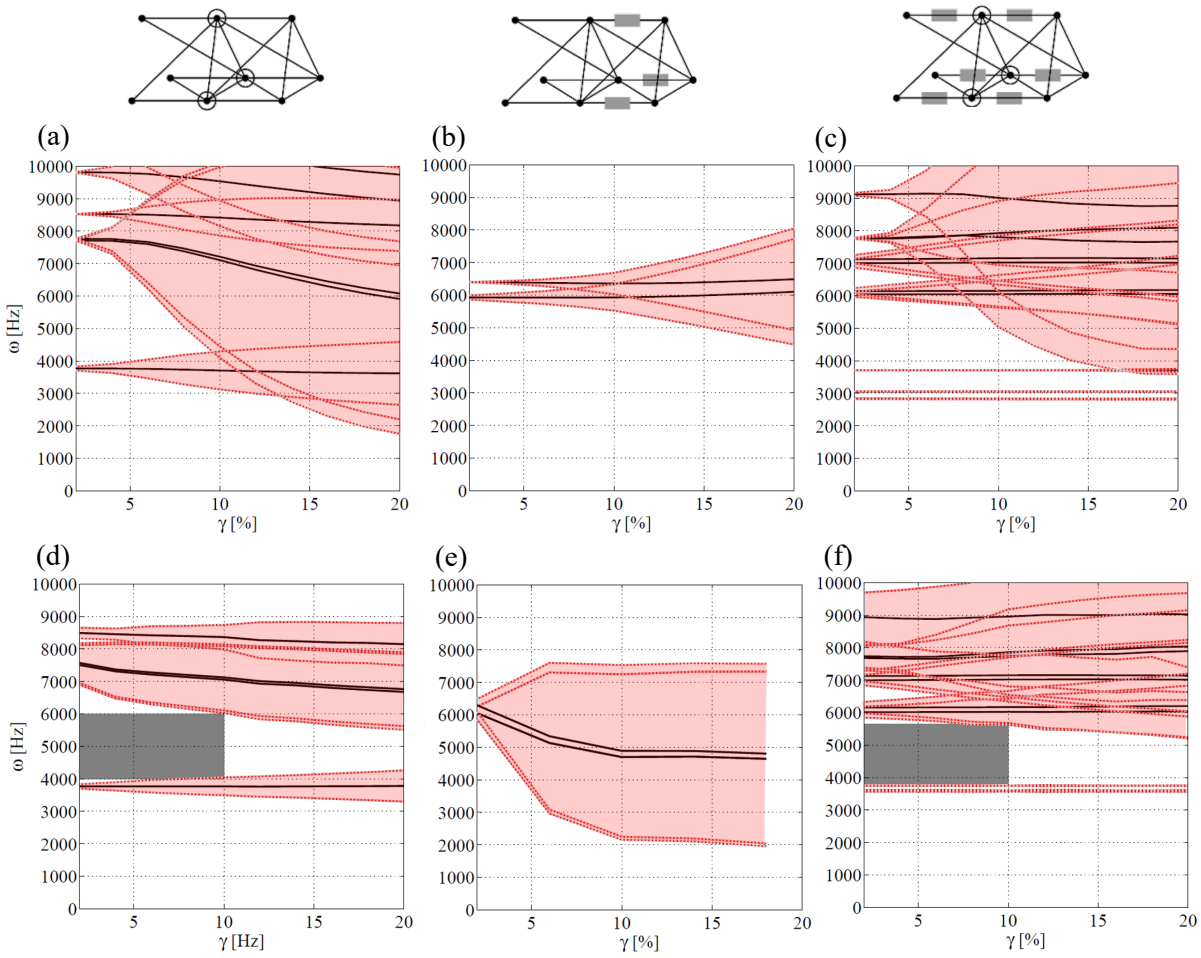

Figure 5.8 Bandgap bounds envelopes relatives to scenarios on Figures 5.3(c), 5.3(f) and 5.3(h), with: (a) mass as RV, (b) and (c) inductance as RV considering an infinite model (1 RV) with their corresponding (d), (e) and (f) for finite results with 10 RV.

Considering a Normal (Gaussian) distribution, this picture shows the means (black lines) and the 95% confidence intervals (red area). It is possible to observe that the envelopes widths increase according to the increasing of uncertainty level. In general, the envelopes are narrower for the models with finite structures (10 RV), approximately less than a half of the bandgaps obtained with infinite structures (1 RV). There is an exception for bandgap borders on Figures 5.8(b) and 5.8(e), where it was not possible to obtain the bandgap borders for finite structure.

If an uncertainty level of 10 % is considered for the random variables, the dark gray areas represent the robust bandgaps (bandgap considering uncertainties on each cell of finite structure).

The localization phenomenon perturbed the result in Figure 5.8(e) and equivalent results were not found as related to Figures 5.8(d) and 5.8(f). This proves that this phenomenon is strongly sensitive to small variations of inductance values in the shunt circuit and an erroneous result is obtained because the border values were not correctly detected.

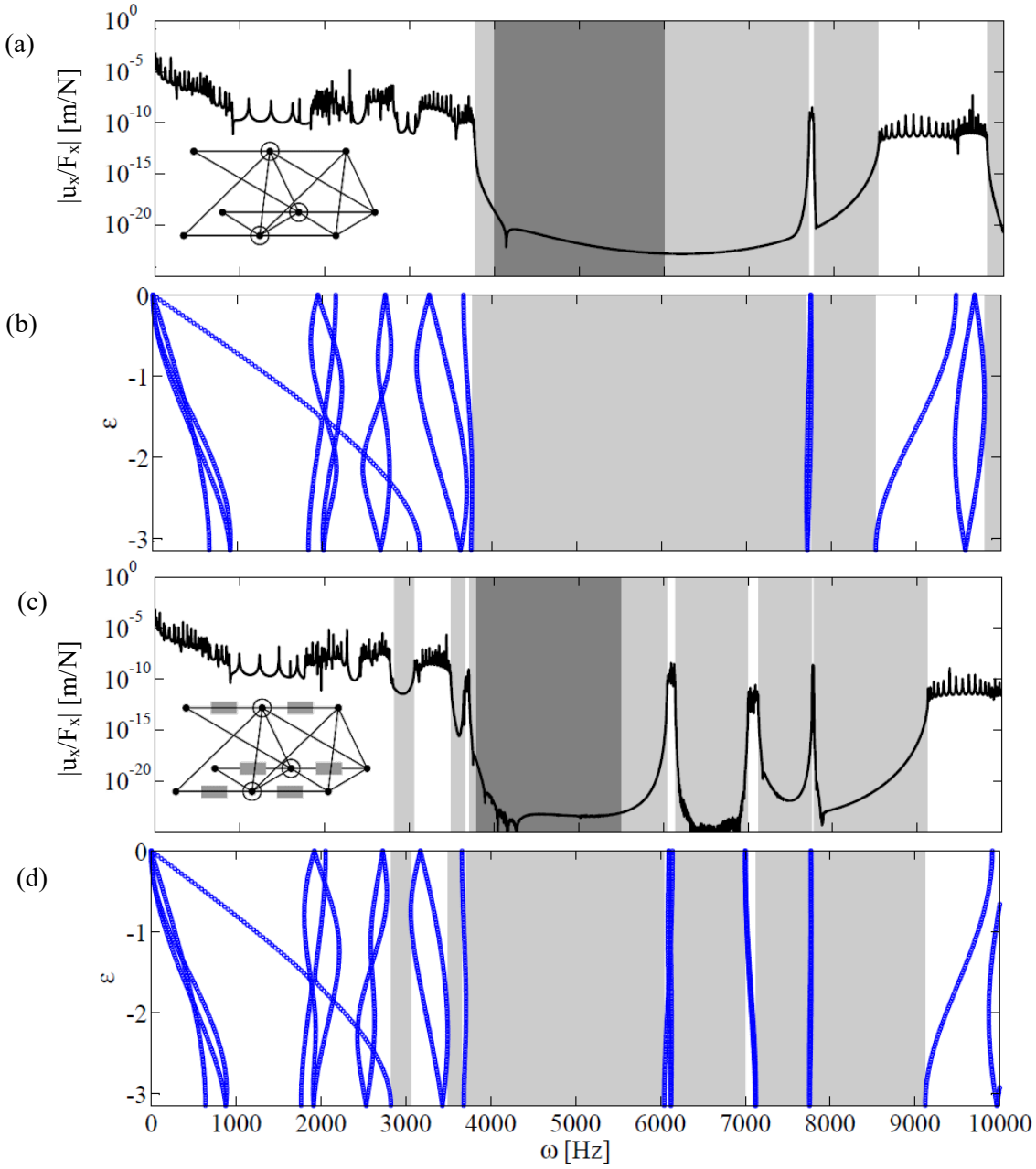

Figure 5.9 Robust band gaps for finite structures composed of 10 unit cells (a) and (c) and their respective dispersions diagramas for infinite structures (b) and (d).

Figure 5.9 elucidates the concept of robust band gap by situating the classical bandgaps and robust bandgaps inside the frequency response and dispersion diagrams, for infinite and finite models.

The light red areas (envelopes) in Figure 5.9 indicate that the attenuation zone calculated with a single random variable is narrower than the dark gray, which was obtained with ten random variables for gamma, considering $_{\gamma}$ = 10%. Thus, when one uncertainty is considered for each cell of a finite structure, which corresponds to practical cases, the effects on the responses are compensated and the structure is intrinsically more robust. This remains true as long as localization phenomena does not appear. However, it can appear

just in the case of finite model simulation. For high values of γ, the chances of appearing this situation is higher.

It is also possible to observe in Figures 5.9(b) and 5.9(d) that there is a branch corresponding to a longitudinal wave that inhibits the appearance of two others low frequency bandgaps, as confirmed in the FRFs shown in Figures 5.7(a) and 5.7(c).

For the case with only local resonance bandgaps, Figures 5.8(b) and 5.8(e), the robust bandgap does not appear in Figures 5.10(a) and 5.10(b) because the envelope cannot be obtained for finite structures. Even if the result for infinite structures is considered for creating this region, it covers the stop band for the value of ten percent of stochasticity level.

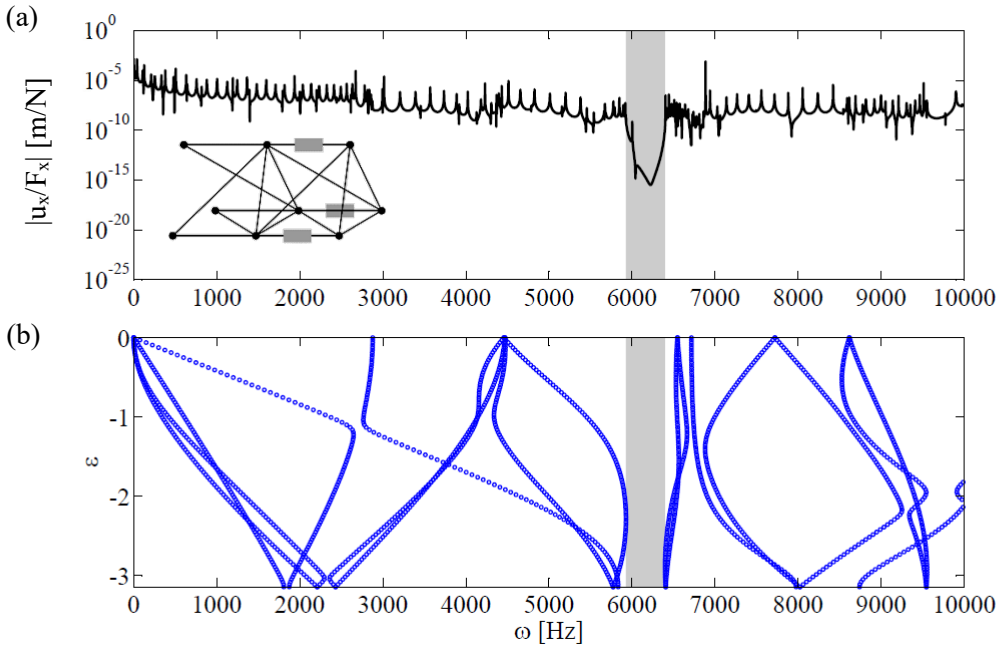

Figure 5.10 Band gap for (a) finite and (b) infinite structures considering the local resonance effect.

After having observed the presence of bandgap in the smart truss, it is necessary for the designer to characterize the physical phenomenon that could increase the width of these bandgaps. In the following, a fully passive truss is presented. Its physical behavior is comparable to the previous interesting cases and its simplicity will help to understand the underlying phenomenon. This lattice structure can be represented analytically by a beam like structure with inner resonances as proposed by (Chesnais *et al.*, 2010; Baravelli and Ruzzene, 2013). However, these inner resonances are not easy to comprehend. Complex modes, as related by Signorelli and Von Flotow (1987) of a wave that can be propagating and attenuating at same time, can be present and the interpretation of the phase and propagation constants on dispersion diagrams are difficult.

5.4 Second structure: beam finite element truss

This numerical example is an attempt to create a truss with lower frequency inner resonances (Chesnais *et al.*, 2010) to observe their effects on dispersion diagrams, according to infinite and finite models. Therefore, the same truss is numerically modeled using Euler-Bernoulli beams with six *dofs* per node. Figure 5.11 illustrates two possibilities of inner resonance unit cells that are substructures with embedded local mass, which implies the presence of local resonance. For vertical excitation, the first one favors the longitudinal modes for beams with concentrated mass in the middle and the second one favors their flexural modes. For horizontal excitation, the flexural modes of the first one are excited while both, flexural and longitudinal modes, are excited for the second unit cell.

Figure 5.12 illustrates the finite element model used for this analysis. Since the beams are excited in multiple directions, it is expected that their behavior is similar to a multi-modal dynamic vibration absorber.

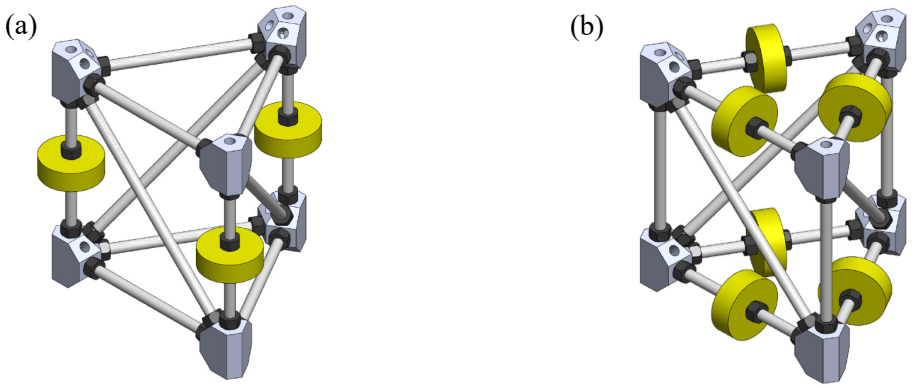

Figure 5.11 Example of truss unit cell with concentrated mass in the middle of (a) vertical and (b) horizontal bars to reduce frequency of inner resonances.

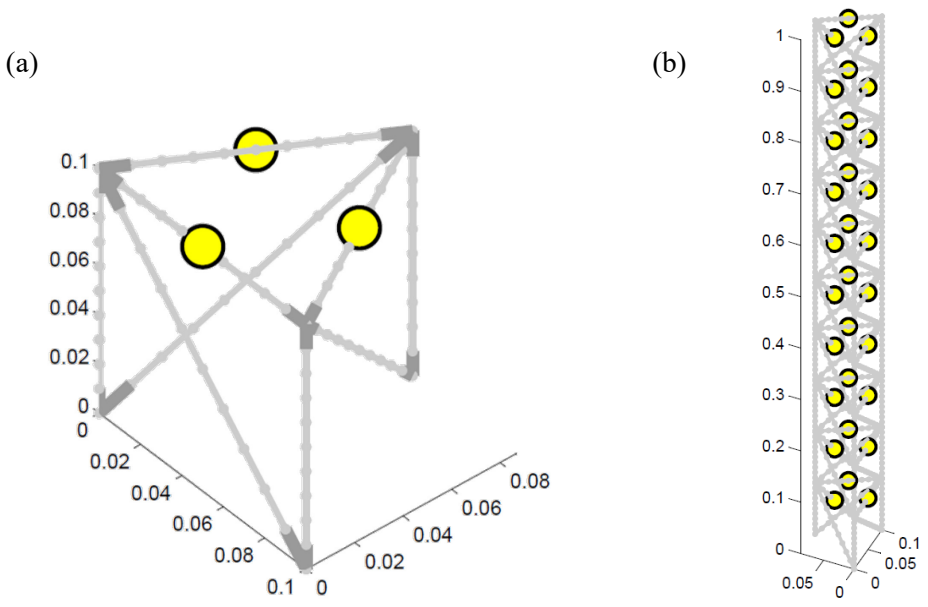

Figure 5.12 (a) Truss unit cell modeled with Euler-Bernoulli beams with concentrated mass on yellow circles dofs and (b) corresponding finite structure.

The frequency response functions are analyzed while a concentrated mass has its position changed from 1 to 9. These numbers represent positions equally spaced along the beam where a mass with 142,5 g is purposely placed.

Figures 5.13(a) and 5.13(b) show the frequency response functions of a clamped-clamped beam with 10 finite elements mesh. It is possible to observe that changing the mass position along the beam can increase or decrease the frequency values for longitudinal and flexural modes. Figure 5.13(c) is a zoomed portion of Figure 5.13(b) and confirms the presence of flexural modes in lower frequency range. The beam with mass on position 5 presents the lowest natural frequencies. In the following, this beam is used as an internal component of a periodic truss.

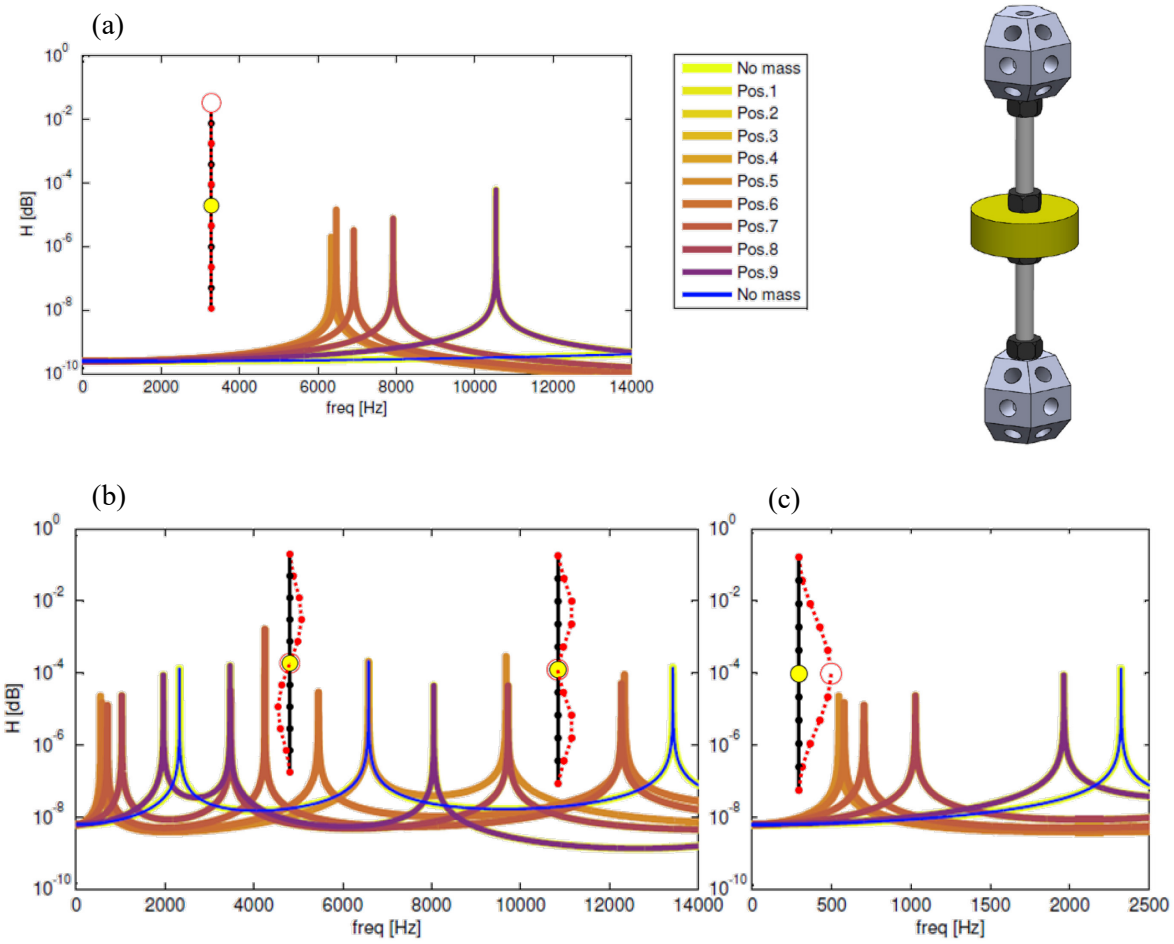

Figure 5.13 Resonant beam with concentrated mass and its (a) first longitudinal mode, (b) first three flexural modes and (c) a zoom of (b) in low frequency.

5.4.1 Dispersion constants

For the sake of better understanding, two different unit cells are considered, the first one without concentrated mass and the second one with this mass in position 5 of horizontal beams. The dispersion constants of the first one are illustrated in Figures 5.14(a) and 5.14(b). The curves for the truss with the inner resonances are presented in Figures 5.14(c) and 5.14(d).

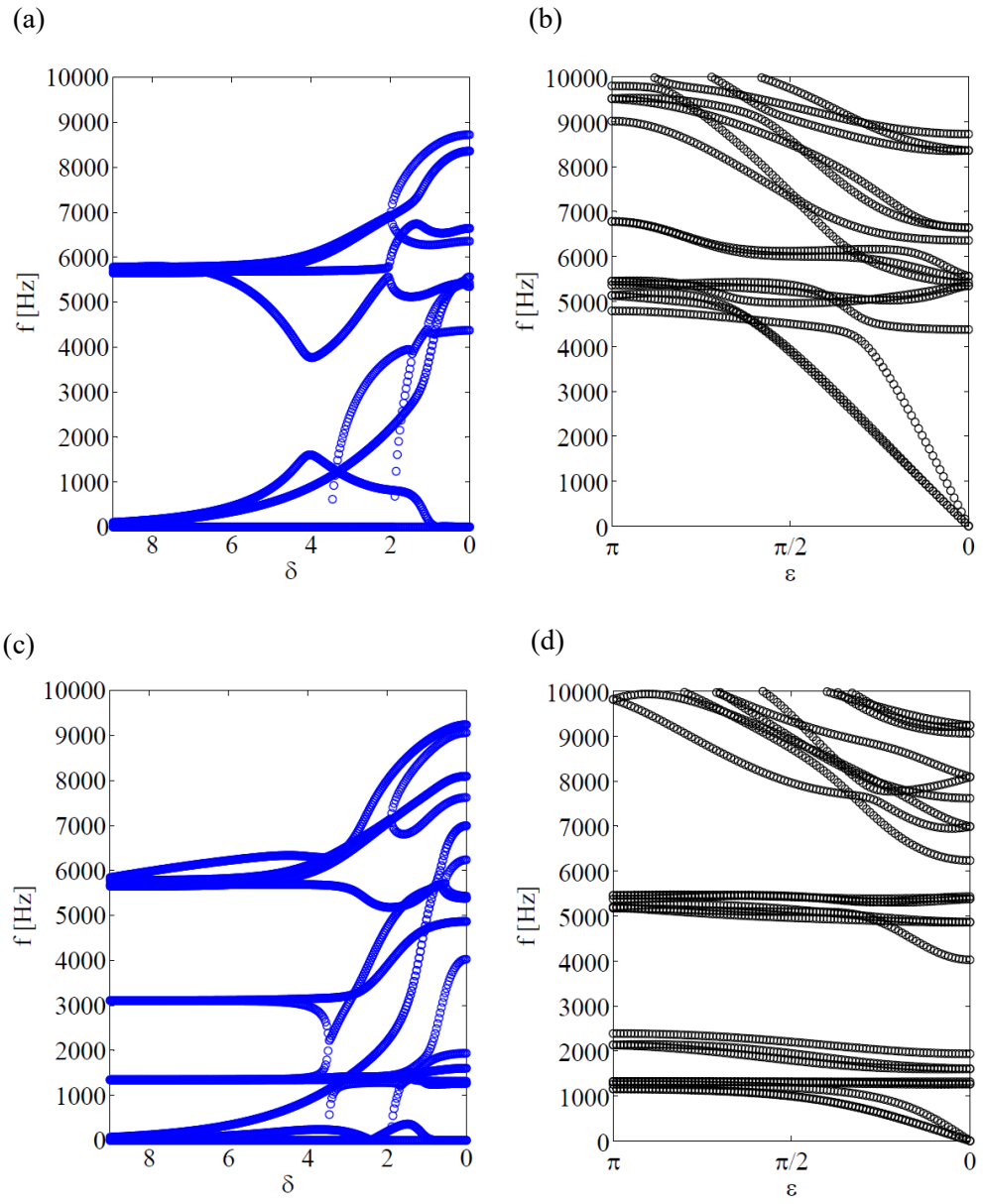

Figure 5.14 Dispersion constants for unit cell (a) without concentrated mass and (b) with mass on position 5.

It is possible to observe that the truss without concentrated mass presents no stop band from 0 to 5000 Hz. However, it is noticed that some wave branches are coupled for different wave types.

Considering attenuation constants of the unit cell with embedded mass, some branches of real part of dispersion constants tend to specific values. Comparing to dispersions constants of local resonance bandgaps of Chapter 2, the real part of propagation constants indicates that their values are related to inner resonances.

5.5 Partial conclusion

A low computational cost three-dimensional periodic structure truss is used as a numerical example. Firstly, solutions for finite and infinite structures are found as well as their frequency response and dispersion diagrams. This structure is discretized by a bar finite element with 3 degrees of freedom per node. A number of cells equals to ten has been selected for the finite structure. This choice is made in order to obtain accurate location of the attenuation frequency zones without substantially increasing the computational cost.

The localization phenomenon is identified related to a location with strong impedance mismatch. This important remark is clarified and explains the behavior of uncertainties in this kind of repetitive structure. A relevant impedance mismatch, which highly differs from the other cells, localized in some place of the repetitive structure can reveal interesting properties.

An uncertainty analysis is performed using the finite and infinite models of the structure. The added joint mass and inductance values are purposely chosen as random variables with a Gaussian probability density function having a mean and standard deviation as stochastic properties.

A coefficient of variation is specified to vary the standard deviation as a percentage of the mean value. Monte Carlo Simulations with Latin Hypercube are conducted until their convergences for each value of the coefficient mentioned before.

The conclusions for infinite and finite models are different. The results for infinite structures are not completely reliable since the same uncertainty is repeated indefinitely. Finite analysis is required to correctly estimate the statistics of dynamic responses.

The confidence envelopes for the full structure with ten stochastic variables is narrower than those found with one random variable on infinite model. Besides, they are more reliable due to the model being closer to reality for the same case. The fact of considering ten random variables, instead of one, proves that the uncertainties self-compensate and the periodic structures are intrinsically robust. Accordingly, a more accurate and reliable robust bandgap is obtained.

Inner resonances are investigated for a numerical example with no spherical joints on nodes, *i.e.* considering Euler-Bernoulli beams with coupled rotation. The dispersion constants are obtained for a truss with and without concentrated mass in the middle of their beams for two different kind of unit cells. The purpose is get more information about these complex modes, where a wave can be propagating and attenuating at same time. There is presumption that the propagation constants are related to the inner resonances. However, the model is computationally time consuming and more research about this topic is needed.

Chapter 6 Conclusion and Perspectives

6.1 Conclusions

In this thesis, the first and main objectives were to perform a probabilistic and reliability analysis of a smart periodic truss and its members, as bar or beams, followed by an experimental validation.

This truss, composed by intelligent actuators as piezoelectric stacks in shunt circuit, would be able to simulate the uncertainty effect by tuning different frequencies while arbitrarily changing the inductance value with small deviations. Although presenting an innovative and ambitious idea, creating local resonance bandgaps in trusses is not an easy task, even assuming hypothesis to facilitate their simulation. In other words, all the objectives were not possible to be reached and some work is still necessary to solve all the issues discovered on the way.

The periodicity effect, which can transform a periodic mechanical structure in mechanical filters that are able to filtrate the vibration in determinate frequency bands, does not induces the appearance of stop bands in low frequency on classical trusses. The impedance mismatch created by their intersection between bays, or referred as unit cell for periodic structures, is not strong enough to create “omni” wave type bandgaps for this kind of structures. Moreover, for local resonance bandgaps, the used models were not able to create attenuation zones in lower frequencies using piezoelectric stack actuators in shunt circuit. These models were presented in the international conference *ASME 2015* and in the workshop *JJCAB 2015*.

For the sake of better understanding these two mechanical filter behaviors, simple models, which can constitute the truss members, were used and a probabilistic analysis was performed presenting the concept of “Robust bandgap”. In other words, this term can be defined as a stop band that considers the uncertainty effects on structure geometrical and physical properties. Consequently, a narrower attenuation zone would be calculated but presenting more chance that those defects, impurities, temperature variation, difference on cell dimensions and many unpredictable situations would not affect the bandgap function.

Firstly, a periodic structure with stepped bar unit cells was numerically simulated using principally two methods: finite element and transfer matrix. The first method is an extremely powerful tool but it can be expensive for infinite and finite models as long as a fine mesh is needed. Moreover, for a probabilistic analysis, which normally need samplings of the model considering different values of parameters, it is not a smart solution considering computational cost. Accordingly, two approaches using transfer matrix, which gives the exact solution from a mathematical point of view, were used to analyze the effect of finiteness on periodic

structure models. The goal was to compare infinite and finite models and, by considering one uncertainty for one infinite cell and one for each cell in a finite structure, respectively, observe the difference between the envelopes with 95% of confidence for a Gaussian distribution for both cases. The obtained results show that the robust bandgap obtained with finite number of cells is larger than the robust bandgap obtained for an infinite structure. The conclusion was that the uncertainties are compensated for a finite model while they are repeated infinitely for an infinite model. However, a natural frequency was inside the attenuation zone which got the attention because, normally, a bandgap does not present resonant peaks. Accidentally, the localization phenomena appeared on simulation results. This study was presented in conference *CFA/VISHNO 2016*. A periodic journal about this subject is in process of correction and it will be submitted soon.

Parametric studies and local sensitivity analyses were performed in these stepped unit cell bars and in general spring-mass unit cell for Bragg's and Local resonance bandgaps. For spring-mass unit cells, the resonance inside the attenuation zone can be obtained by calculating the value of natural frequencies for a free finite structure with only one unit cell. The same can be observed for both types of attenuation zones. This was presented in the international conference *MEDYNA 2017*.

For longitudinal vibration, the symmetry of an unit cell can tells by calculating its natural frequency for free-free boundary conditions the presence of specific localized modes. It can be verified for periodic bar models and spring-mass systems. However, for beam free-free models it cannot be verified.

Envisaging a future experimental evaluation, a periodic Euler Bernouilli beam model was investigated. The Transfer Matrix method was firstly used to simulate this model, but stability problems were found. This multi-coupled periodic structure present an ill-conditioned transfer matrix which, if self-multiplied, makes the computer finite arithmetic errors grow exponentially. One way to reduce this problem is avoiding matrix multiplication. An adapted recursive method (Translation Matrix method), normally used in acoustics, was used and the finite periodic structure response was calculated. The robust bandgap was obtained considering first half-cell thickness as uncertain variable. Although this beam stepped unit cell not being symmetric, no natural frequencies were found inside the attenuation zone. Its corresponding symmetric unit cells, *i.e.*, presenting same dispersion constants, has natural frequencies inside the attenuation zone and it does not correspond to natural frequencies of finite structure with only one unit cell.

Experimentally, a truss is not a structure of simple construction and instrumentation. Their joints are not perfect and several other uncertain geometrical and physical parameters can be influent on frequency response. To observe the feasibility and the measurement of frequency responses with bandgaps, a periodic beam with stepped unit cell was used. An impact hammer was used to apply an impulse to favors flexural waves on the left size of a periodic beam with uncertainties on thickness and length of half-cell. The experiment was executed under free-free boundary conditions. The corresponding acceleration was measured in the right side of this beam. In low frequency until the first border of second bandgap, the numerical model agrees with experimental results. Inside the attenuation zone, it was not possible to measure the structure response because, as it is demonstrated in theory, its magnitude is extremely small and the room noise over-

lay the structure response near the accelerometer resolution. However, unexpected modes appeared inside the attenuation zone and it was verified by simulation with small angle variations on excitation force.

Finally, a periodic truss model was simulated considering bar models with passive and active members. A probabilistic analysis was performed and for the cases where the bandgaps were observable, the robust bandgap considering uncertain values for mass value on joints and inductance value for infinite and finite models was obtained. This work was presented in *ISMA/USD2016* and it received the *award of best student article in uncertainties*.

For a mesh convergence for this truss model, beam finite elements were used. However, the active PZT stack members were not considered because of the presence of bending moments that could damage these type of actuators for a future experimental implementation. Therefore, to analyze the presence of inner resonances, concentrated mass was considered in the middle of specified beams with the purpose of bringing the value of local resonances to lower frequencies. This was presented at *JJCAB2016*.

6.2 Contributions

The originality of this work is based on robustness aspects of periodic structures. Although the presence of several unexpected facts, some important contributions were made and they are listed as follow.

For longitudinal waves in stepped rod unit cells, one contribution is the concept of Robust Bandgap that was presented for the first time and it was verified by considering uncertainties in finite models that periodic structures are naturally robust. For finite structures, the presence of deviations in physical and geometrical unit cell properties creates the localization phenomenon inside the stop band and it goes from its borders to the middle as the impedance mismatch that caused this localized mode becomes stronger. If the peaks inside the bandgap are not considered a problem, although their presence within this region, the attenuation zones have less variation in their border positions and the finiteness of a periodic structure shows that this type of structure is consequently more robust. These conclusions were obtained comparing results of infinite and finite models. Additionally, it was verified that the natural frequencies of one unit cell can predict a kind of localized mode.

For longitudinal waves in spring-mass systems, analytical equations for Bragg's and local resonance bandgap borders were presented. It was also possible to track the natural frequency inside the stop band. One important observation and contribution it that this mode can be near of bandgap borders and it can be misinterpreted as a bandgap border. In addition, a local resonance bandgap can be inside the zone of a Bragg's bandgap and the dispersion constants may not show its presence. To the best knowledge of the author, it was the first time that a general unit cell was proposed to investigate analytically, with the developpement of

closed-form equations, the bandgap borders for Bragg's and local resonance bandgaps considering the number and type of spring-mass chaings and internal resonators.

For flexural waves in stepped beam unit cells, the same robust conclusion was verified with numerical probabilistic analysis. Another novelty is that a recursive method termed as Translation Matrix method was successfully used for the first time for flexural waves to avoid stability problems. Semi-analytical results were presented for finite structures and this procedure presented efficiency and low computation time comparing to finite element analysis. Furthermore, the natural frequencies of one unit cell for free-free boundary conditions does not predict the presence of localized modes inside the attenuation zone. In this case, the asymmetric unit cell does not present natural frequencies inside the attenuation zone while the symmetric unit cells do.

It was shown experimentally that it is impossible to excite a structure intending to excite just one type of wave if the frequency band is not a stop band for other wave types. The region inside the bandgap is sensitive and the modes corresponding to other type of waves can be excited because of the presence of weak angle deviations.

For several types of waves propagating in a truss unit cell, a robust bandgap was also verified for a truss model considering spherical joints. The effects of adding mass on joints and tuning a shunt circuit for this kind of structure were investigated using infinite and finite models and the localization phenomena was intentionally created to be analyzed in this model.

Moreover, it is the first time a 3D smart periodic truss with periodic assumptions was purposely modeled to simulate uncertain input variables, as circuit components, that can be tuned. This original approach is a powerfull tool concerning uncertainty investigation no matter what domain is investigated.

6.3 Perspectives

Several ideas were conceived to solve the problems above mentioned and to explore more the great potential of combining periodic and smart materials. Therefore, the perspectives are listed in the following.

- Firstly, other probabilistic methods can be used to verify the robustness of a stop band. Different ways to obtain the bandgap borders in a finite structure can be used. One idea would be to combine the use of both analyses to investigate complex structures by using infinite models to firstly discover the bandgap zone and, after, execute an algorithm to search all important measures inside this region using a finite model, *i.e.*, where the borders, anti-resonances and localized modes are placed.

- Secondly, create a bandgap, to be analized experimentally, without having other type of waves and excited modes inside the attenuation zone. On solution could be optimize the structure considering place the unwanted natural frequencies of other wave types inside the propagation zone. For example, a structure with circular cross-section would not have this problem for flexural waves. The Translation Matrix method can be used to create the objective function of this multi-objective optimization problem.

- Thirdly, as observed in frequency response with localization phenomena, bandgap robustness and width can be improved using gradient effects. Another perspective is investigate the potential of non-uniform periodicity or gradient meta-structures.

- Investigate the localization phenomena as valuable information about unexpected impedances mismatches inside the periodic structure. For example, it can be used for Structural Health Monitoring for a purposely-designed periodic structure. Thus, more investigation is needed and this phenomenon can be intentionally created in periodic beams to be investigated with more details.

- Explore the idea of tunable periodic structures. It has to be developed for simple structures involving smart materials. More information is needed before implementing the powerful smart truss.

6.4 List of publications and presentations

- L.R. Cunha, R.J. Portugal, D.A. Rade, M. Ouisse. *Estrutura periódica unidimensional contendo atuadores piezelétricos para controle de vibrações*, **Simpósio do Programa de Pós-Graduação em Engenharia Mecânica (POSMEC 2014)**, Uberlândia/MG, Brazil, November 2014 (Article and Poster);

- L.R. Cunha, M. Ouisse, D.A. Rade, *Uncertainty analysis of a Smart Periodic truss*, **Smart Materials, Adaptive Structures and Intelligent Systems (SMASIS, ASME 2015)**, Colorado Springs - CO, EUA, September 2015 (Abstract and presentation);

- L.R. Cunha, M. Ouisse, D. A. Rade, *Analyse d'incertitudes sur des treillis périodiques intelligents,* **Journées Jeunes Chercheurs en vibration, Acoustique et Bruit (JJCAB 2015)**, Besançon, France, November 2015 (Abstract, poster and presentation);

- L.R. Cunha, D.A. Rade, M. Ouisse, *Conception de Bandes Interdites Robustes pour les Structures Périodiques Unidimensionelles,* **Congrès Français d'Acoustique joint avec Colloque Vibrations, Shocks and Noise (CFA/VISHNO 2016)**, Le Mans, France, April 2016 (Abstract, article and presentation);

- L.R. Cunha, M. Ouisse, D.A. Rade, *Robust Smart Periodic Truss*, **International Conference on Noise and Vibration Engineering/International Conference on Uncertainty in Structural Dynamics (ISMA/USD 2016)**, Leuven, Belgium, September 2016 (Abstract, Article and presentation with **USD2016 best Student Paper Award**);

- L.R. Cunha, M. Ouisse, D. A. Rade, *Accord non uniforme d'amortisseurs dynamiques multi modaux pour treillis périodiques*, **Journées Jeunes Chercheurs en vibration, Acoustique et Bruit (JJCAB 2016)**, Marseille, France, November 2016 (Abstract, poster and presentation);

- L.R Cunha, M. Ouisse, D.A. Rade*, Analytical and Numerical Local Sensitivity Analysis of Periodic Spring-Mass Chains*, **2nd Euro-Mediterranean Conference on Structural Dynamics and Vibroacoustics (MEDYNA 2017)**, Sevilla, Spain, April 2017 (Abstract, article and presentation).

References

[1] ANDERSON, P.W. Absence of Diffusion in Certain Random Lattices. **Physical Review**, v. 109(5), p. 1492-1505, 1958.

[2] ANDERSON, P.W. Local Moments and Localized states, **Nobel Lecture**, 1977.

[3] BANSAL, A.S. Free wave motion in periodic systems with multiple disorders. **Journal of Sound and Vibration**, v. 60(3), p.389-400, 1978.

[4] BANSAL, A.S. Free waves in periodically disordered systems: natural and bounding frequencies of unsymmetric systems and normal mode localization. **Journal of Sound and Vibration**, v. 207(3), p. 365-382, 1997.

[5] BANERJEE, B. **An Introduction to Metamaterials and Waves in Composites**. CRC Press. New York, 2011.

[6] BARAVELLI, E. and RUZZENE, M. Internally resonating lattices for bandgap generation and low-frequency vibration control, **Journal of Sound and Vibration**, v. 332, p. 6562-6579, 2013.

[7] BILLON, K.; ZAMPETAKIS, I.; SCARPA, F.; OUISSE, M.; SADOULET-REBOUL, E.; COLLET, M.; PERRIMAN, A. and HETHERINGTON, A. Mechanics and band gaps in hierarchical auxetic rectangular perforated composite metamaterials. **Composite Structures**, 2016.

[8] BILLON, K. **Composites périodiques fonctionnels pour l'absorption vibroacoustique large bande. Mécanique des solides**, Université de Franche-Comté, Besançon, 2016.

[9] BLIVEN, D.O. and SOONG, T.T. On frequencies of Elastic Beams with random imperfections. **Journal of the Franklin Institute**, v. 297(4), p. 297-304, 1969.

[10] BLOCH, F. Uber die quantenmechanik der elektronen in kristallgittern. **Zeitschrift fur Physik**, v. 52, n. 7-8, p. 555–600, 1929.

[11] BOGDANOFF, J.L. and CHENEA, P.F. Dynamics if some disordered linear systems, **Int. J. Mech. Sci**., v. 3, p. 157-169, 1961.

[12] BOUZIT, D. and PIERRE, C. Localization of vibration in disordered multi-span beams with damping. **Journal of Sound and Vibrations**, v. 187(4), p. 625-648, 1995.

[13] BOUZIT, D and PIERRE, C. An Experimental Investigation of Vibration Localization in Disordered Multi-Span Beams, **Journal of Sound and Vibration**, v. 187(4), p.649-669, 1995.

[14] BRAGG, W. Bakerian lecture: X-rays and crystal structure. **Philosophical Transactions of the Royal Society of London. Series A**, Containing Papers of a Mathematical or Physical Character, v. 215, p. 253–274, 1915.

[15] BRAGG, W. L. The diffraction of X-rays by crystals, **Nobel Lecture**, September 6, 1922.

[16] BRILLOUIN, L. **Wave Propagation in Periodic Structures**. New York: Dover, 1946.

[17] BUTAUD, P.; PLACET, V.; KLESA, J.; OUISSE, M.; FOLTÊTE, E. and GABRION, X. Investigations on the frequency and temperature effects on mechanical properties of a shape memory polymer (Veriflex). **Mechanics of Materials**, v. 87, p.50-60, 2015.

[18] CASADEI, F.; BECK, B.S.; CUNEFARE, K.A. and RUZZENE, M. Vibration control of plates through hybrid configurations of periodic piezoelectric shunts. **Journal of Intelligent Material Systems and Structures**, v. 23(10), p. 1169-1177, 2012.

[19] CHEN, A.-L. And WANG, Y.-S. Study on band gaps of elastic waves propagating in one-dimensional disordered phononic crystals. **Physica B**, v. 392, p. 369-378, 2007.

[20] CHESNAIS, C.; BOUTIN, C. and HANS, S. Effects of the local resonance on the wave propagation in periodic frame structures: Generalized Newtonian mechanics. **Journal of Acoustical Society of America**, v. 132(4), p.2873-2886, 2012.

[21] CHOI, S.K.; GRANDHI, R.V. and CANFIELD, R.A. **Reliability-Based Structural Design**, London: Springer-Verlag, 2007, 306p.

[22] CLAEYS, C.C.; VERGOTE, K.; SAS, P. and DESMET, W. On the potential of tuned resonators to obtain low-frequency vibrational stop bands in periodic panels, **Journal of Sound and Vibration**, v. 332, p. 1418-1436, 2013.

[23] COLLET, M.; OUISSE, M.; RUZZENE, M. and ICHCHOU, M. Floquet-Bloch decomposition for the computation of dispersion of two-dimensional periodic, damped mechanical systems, **International Journal of Solids and Structures**, v. 48 (20), p. 2837-2848, 2012.

[24] CHRISTEN, J.L.; ICHCHOU, M.; TROCLET, B.; BAREILLE, M. and OUISSE, M. Global sensitivity analysis of analytical vibroacoustic transmission models. **Journal of Sound and Vibration**, v. 368, p. 121-134, 2016.

[25] DAZEL, O.; GROBY, J.-P.; BROUARD, B. and POTEL, C. A stable method to model the acoustic response of multilayered structures. **Journal of Applied Physics**, v. 113, 2013.

[26] DELL'ISOLA, F.; MAURINI, C. and PORFIRI, M., Passive damping of beam vibrations through distributed electric networks and piezoelectric transducers: prototype design and experimental validation. **Smart materials and Structures**, v. 13, p. 299-308, 2004.

[27] DEN HARTOG, J.P., **Mechanical Vibrations**, McGraw-Hill Book Company, Inc., 1956, 366p.

[28] DOYLE, J.F. **Wave Propagation in Structures** 2ed. Mechanical Engineering series, Springer Science + Business Media, New York, 1997.

[29] FLOQUET, G. Sur les équations différentielles linéaires à coefficients périodiques. **Annales scientifiques de l'ENS**, v.129(1), p. 47-88, 1883.

[30] FRAHM, H. Device for damping vibrations of bodies, **US Patent 989**, 958, 1907.

[31] GRAFF, F. **Wave Motion in Elastic Solids**. Dover Publications Inc. New York, 1975.

[32] GRAVIC, L. Computation of propagative waves in free rail using a finite element technique. **Journal of Sound and Vibration**, v. 185 (3), p. 531–543, 1995.

[33] HAGOOD, N.W. and VON FLOTOW, A. Damping of Structural Vibrations with Piezoelectric Materials and Passive Electrical Networks, **Journal of Sound and Vibration**, v. 146(2), p. 243-268, 1991.

[34] HALDAR, A. and MAHADEVAN, S. **Probability, Reliability and Statistical Methods in Engineering Design**, New York: John Wiley & Sons, 2000.

[35] HASKELL, N. A. The dispersion of surface waves on multilayered media. **Seismological Society of America**, v. 43(1), p.17-34, 1953.

[36] HODGES, C.H. Confinement of vibration by structural irregularity. **Journal of Sound and Vibration**, v. 82(3), p. 411-424, 1982.

[37] HUSSEIN, M. I.; LEAMY, M. J. and RUZZENE, M. Dynamics of Phononic Materials and Structures: Historical Origins, Recent Progress, and Future Outlook, **ASME**, v. 66, 2014.

[38] HVATOV, A. and SOROKIN, S. Free Vibration of finite periodic structures in pass- and stop-bands of the counterpart infinite waveguides. **Journal of Sound and Vibration**, v. 347, p. 200-217, 2015.

[39] JENSEN, J.S. and PEDERSEN, N.L. On maximal eigenfrequency separation in two-material structures: the 1D and 2D scalar cases. **Journal of Sound and Vibration**, v. 289, p. 967-986, 2006.

[40] JENSEN, J.S. Phononic band gaps and vibrations in one- and two-dimensional mass-spring structures. **Journal of Sound and Vibration**, v. 266, p. 1053-1078, 2003.

[41] ICHCHOU, M.; BOUCHOUCHA, F.; BEN SOUF, M.A.; DESSOMBZ, O. and HADDAR, M. Stochastic wave finite element for random periodic media through first-order perturbation, **Comput. Methods Appl. Mech. Engrg**., v. 200, p. 2805-2813, 2011.

[42] JUNYI, L. and BALINT, D.S. An inverse method to determine the dispersion curves of periodic structures based on wave superposition. **Journal of Sound and Vibration**. v. 350, p. 41-72, 2015.

[43] JUNYI, L.; RUFFINI, V. and BALLINT, D.S. Measuring the band structures of periodic beams using the wave superposition method. **Journal of Sound and Vibration**, 2016.

[44] KISSEL G.J. **Localization in disordered periodic structures**. PhD Thesis. 1988.

[45] KISSEL, G.J. Localization factor for multichannel disordered systems. **Physical Review A**, v. 44 (2), p. 1008-1014, 1991.

[46] KORENEV, B.G. and REZNIKOV, L.M. **Dynamic Vibration Absorbers**, Theory and Technical Application John Wiley & Sons DVA, 1993.

[47] LANGLEY, R.S. On the forced response of one-dimensional periodic structures: vibration localization by damping**. Journal of Sound and Vibration**, v. 178(3), p.411-428, 1994.

[48] LEAMY, M.J. Exact wave-based Bloch analysis procedure for investigating wave propagation in two-dimensional periodic lattices, **Journal of Sound and Vibration**, v. 331, p. 1580-1596, 2012.

[49] LEMAIRE, M. **Structural Reliability**, ISTE, 2009.

[50] LEO, D.J. **Engineering Analysis of Smart Material Systems**, New Jersey: John Wiley & Sons, 2007.

[51] LI, D. and BENAROYA, H. Dynamics of periodic and near-periodic structures. **Appl. Mech. Rev.**, v. 45(11), p. 447-459, 1992.

[52] LI, D. and BENAROYA, H. Waves, normal modes and frequencies in periodic and near-periodic rods. Part I. **Wave Motion**, v. 20(4), p. 315-338, 1994.

[53] LI, D. and BENAROYA, H. Waves, normal modes and frequencies in periodic and near-periodic rods. Part II. **Wave Motion**, v. 20(4), p. 339-358, 1994.

[54] LIN, Y.K. and MCDANIEL, T.J. Dynamics of beam-type periodic structures. **Journal of Manufacturing Science and Engineering**, v. 91, p. 1133–1141, 1969.

[55] LIN, Y.K. and YANG, J.N. Free vibration of a disordered periodic beam. **Journal of Applied Mechanics, ASME**, p. 383-391, 1974.

[56] LIN, Y.K. Dynamics of disordered periodic structures**. Appl Mech Rev**, v. 49(2), p.57-64, 1996.

[57] LOSSOUARN, B.; AUCEJO, M. and DEÜ, J.F. Multimodal coupling of periodic lattices and application to rod vibration damping with a piezoelectric network. **Smart Materials and Structures**, v. 24, 13p, 2015a.

[58] LOSSOUARN, B.; DEÜ, J.F. and AUCEJO, M. Multimodal vibration damping of a beam with Periodic array of piezoelectric patches connected to a passive electrical network. **Smart Materials and Structures**, v. 24 (11), 14p, 2015b.

[59] LUONGO, A. Mode localization by structural imperfections in one-dimensional continuous systems. **Journal of Sound and Vibration**, v. 155, p. 249-271, 1992.

[60] LUST, S.D.; FRIEDMANN, P.P. and BENDIKSEN, O.O. Free and forced response of multi-span beams and multi-bay trusses with localized modes. **Journal of Sound and Vibration.** v. 180(2), p. 313-332, 1995.

[61] MACE, R.M. and MANCONI E. Modelling wave propagation in two-dimensional structures using finite element analysis. **Journal of Sound and Vibration.** v. 318, p. 884-902, 2008.

[62] MARNEFFE, B. and PREUMONT, A. Vibration damping with negative capacitance shunts: theory and experiment. **Smart materials and Structures**, v. 17, 9p, 2008.

[63] MEAD, D.J. Free wave propagation in periodically supported, infinite beams. **Journal of Sound and Vibration**, v. 11, p.181–197, 1970.

[64] MEAD, D.J. A general theory of harmonic wave propagation in linear periodic systems with multiple coupling. **Journal of Sound and Vibration**, v. 27, p. 235–260, 1973.

[65] MEAD, D.J. Wave propagation and natural modes in periodic systems: I. mono-coupled systems, **Journal of Sound and Vibration**, v. 40, p.1-18, (1975a).

[66] MEAD, D.J. Wave propagation and natural modes in periodic systems: II. Multi-coupled systems with and without damping, **Journal of Sound and Vibration**, v. 40, p.19-39, (1975b).

[67] MEAD, D.J. and BANSAL, A.S. Mono-coupled periodic systems with a single disorder: free wave propagation. **Journal of Sound and Vibration**, v. 61(4), p. 481-496, 1978a.

[68] MEAD, D.J. and BANSAL, A.S. Mono-coupled periodic systems with a single disorder: response to convected loadings. **Journal of Sound and Vibration**, v. 61(4), p. 497-515, 1978b.

[69] MEAD, D.J. Wave Propagation in continuous periodic structures: Research contributions from Southampton, 1964-1995. **Journal of Sound and Vibration**, v. 190(3), p. 243-268, 1996.

[70] MENCIK, J.M. New advances in forced response computation of periodic structures using the wave finite element (WFE) method. **Computational Mechanics**, v. 54(3), p. 789-801, 2014.

[71] MELCHERS, R.E. **Structural Reliability Analysis and Prediction,** Second edition, New York: John Wiley & Sons, 1999.

[72] MESTER, S.S. and BENAROYA, H. Periodic and Near-Periodic Structures. **Shock and Vibration**, Vol. 2(1), pp. 69-65 1995.

[73] MONTROL, E.W. and POTTS, R.B. Effect of defects on lattice vibrations**. Physical Review**, v. 100(2), p. 525-543, 1955.

[74] NEWTON, I. **Principia Book II**, Imprimatur S. Pepys, Reg. Soc. Praeses, London. 1686.

[75] NOOR, A.K.; ANDERSON, M.S.; GREENE, W.H. Continuum Models for Beam-and Platelike Lattice Structures, **American Institute of Aeronautics Astronautics Journal**, v. 16(12), p. 1219-1228, 1978.

[76] ORRIS, R. and PETYT, M. A finite element study of harmonic wave propagation in periodic structures. **Journal of Sound and Vibration**, v. 33(2), p. 223-236, 1974.

[77] OUISSE, M.; ICHCHOU, M.; CHEDLY, S. and COLLET, M. On the sensitivity analysis of porous material models. **Journal of Sound and Vibration**, v. 331. p. 5292-5308, 2012.

[78] PARK, C.H. and BAZ, A. Vibration Control of Beams with Negative Capacitive Shunting of Interdigital Electrode Piezoceramics, **Journal of Vibration and Control**, v. 11, p. 331-346, 2005.

[79] PIERRE, C. Weak and strong vibration localization in disordered structures: a statistical investigation. **Journal of Sound and Vibration**, v.139 (1), p. 111-132, 1990.

[80] PODDUBNY, A.N. and IVCHENKO, E.L. Photonic quasicrystalline and aperiodic structures. **Physica E**, v. 42, p. 1871-1895, 2010.

[81] PREUMONT, A. **Vibration Control of Active Structures**, Second edition, Kluwer Academic Publishers, 2004.

[82] RADE, D.A. and STEFFEN, V. Optimisation of dynamic vibration absorbers over a frequency band. **Mechanical Systems and Signal Processing**. v. 14 (5), p. 679-690, 2000.

[83] RAYLEIGH, L. On the maintenance of vibrations by forces of double frequency, and on the propagation of waves through a medium endowed with a periodic structure. **Philosophical Magazine Series 5**, v. 24, n. 147, p. 145-159, 1887.

[84] RUZZENE, M. and BAZ, A. Attenuation and localization of wave propagation in periodic rods using shape memory inserts. **Smart Material and Structures**, v. 9, p. 805-816, 2000.

[85] RUZZENE, M. and SCARPA, F. Control of Wave Propagation in Periodic Sandwich Beams. **Journal of Intelligent Materials and Structures**, v. 14, p. 443-453, 2003.

[86] RUZZENE, M. and SCARPA, F. Directional and band-gap behavior of periodic auxetic lattices, **Physica status solidi (b),** v. 242 (3), p.665-680, 2005.

[87] SALES, T.P.; RADE, D.A. and SOUZA, L.C.G, Passive vibration control of flexible spacecraft using shunted piezoelectric transducers. **Aerospace Science and Technology**, v. 29 (1), p.493-412, 2013.

[88] SALTELLI, A.; CHAN, K. And SCOTT, E.M. **Sensitivity Analysis**, Wiley: New York, 2000, 504 p.

[89] SEN-GUPTA, G. Natural frequencies of periodic skin-stringer structures using a wave approach. **Journal of Sound and Vibration**, v. 16, 567–580, 1971.

[90] SCHNEIDER, D.; GOMOPOULOS, N.; KOH, C.Y.; PAPADOPOULOS, P.; KREMER, F.; THOMAS, E.L. and FYTAS, G. Nolinear control of high-frequency phonons in spider ilk. **Nature Materials**, v.15, p. 1079-1083, 2016.

[91] SIGALAS, M.M. and SOUKOULIS, C.M. Elastic-wave propagation through disordered and/or absorptive layered systems. **Physical Review B**, v. 51(5), p. 2780-2789, 1995.

[92] SIGALAS, M.M.; SOUKOULIS, C.M.; CHAN, C.-T. and TUNER, D. Localization of electromagnetic waves in two-dimensional disordered systems. **Physical Review B**, v. 53(13), p. 8340-8348, 1996.

[93] SIGNORELLI, J. and VON FLOTOW, A.H. Wave Propagation, Power flow, and Resonance in a Truss Beam, **Journal of Sound and Vibration**, v. 126(1), p. 127-144, 1988.

[94] SIGNORELLI, J. and VON FLOTOW, A.H. Wave Propagation in Periodic Truss Structures, **American Institute of Aeronautics Astronautics Journal**, p. 900-909, 1987.

[95] SILVA, P.B. **Dynamic Analysis of periodic structures via wave-based numerical approaches and substructuring techniques**. 232 p. Tese (Doutorado). Faculdade de Engenharia Mecânica, Universidade Estadual de Campinas, Campinas, 2015.

[96] SILVA, P.B.; MENCIK, J.M. and ARRUDA, J.R.F. *On the use of the wave finite element method for passive vibration control of periodic structures*. **Advances in Aircraft and Spacecraft Sciences**, v. 3(3), p. 299-315, 2016.

[97] SOONG, T.T. and BOGDANOFF, J.L. On the natural frequencies of a disordered linear chain of N degree of freedom, **Int. J. Mech. Sci**., v. 5, p.237-265, 1963.

[98] SPADONI, A. and RUZZENE, M. Structural and acoustic behavior of chiral truss-core beams, **Journal of Vibration and Acoustics**. v. 128, p. 616-626, 2006.

[99] SPADONI, A.; RUZZENE, M. and CUNEFARE, K. Vibration and Wave Propagation Control of Plates with Periodic Arrays of Shunted Piezoelectric Patches, **Journal of Intelligent Material Systems and Structures**, v. 20, p. 979-990, 2009.

[100] TANIKER, S. and YILMAZ C. Phononic gaps induced by inertial amplification in BCC and FCC lattices, **Physics Letters A**, v. 377, p. 1930-1936, 2013.

[101] TATEO, F.; COLLET, M.; OUISSE M.; ICHCHOU, M.N.; CUNEFARE, K.A. and ABBE, P. Experimental characterization of a bi-dimensional array of negative capacitance piezo-patches for vibroacoustic control. **Journal of Intelligent material Systems and Structures**, v. 26, p. 952-964, 2014.

[102] TATEO, F.; COLLET, M.; OUISSE, M. and CUNEFARE, K.A. Design variables for optimizing adaptive metacomposites made of shunted piezoelectric patches distribution. **Journal of Vibration and Control**, v. 22, p. 1838-1854, 2014.

[103] THORP, O.; RUZZENE, M. and BAZ, A. Attenuation and localization of wave propagation in rods with periodic shunted piezoelectric patches. **Smart Materials and Structures**, v. 10, p. 979-989, 2001.

[104] THOMPSON, W. T. Transmission of Elastic Wave through a Stratified Solid Medium. **Journal of Applied Physics**, v. 21, 1950.

[105] TRAINITI, G.; RIMOLI, J.J. and RUZZENE, M. Wave propagation in periodically undulated beams and plates. **International Journal of Solids and Structures**, v. 75-76, p. 260-276, 2015.

[106] TRAINITI, G.; RIMOLI, J.J. and RUZZENE, M. Wave propagation undulated structural lattices. **International Journal of Solids and Structures**, v. 97-98, p. 431-444, 2016.

[107] WU, Z.-J; LI, F.-M and ZHANG, C. Vibration properties of piezoelectric square lattice structures, **Mechanics Research Communications**, v. 62., p. 123-131, 2014.

[108] XIE, W.-C. and ARIATANAM, S.T. Vibration mode localization in disordered cyclic structures, I: single substructure mode. **Journal of Sound and Vibration**, v. 189(5), p. 625-645, 1996a.

[109] XIE, W.-C. and ARIATANAM, S.T., Vibration mode localization in disordered cyclic structures, II: multiple substructure modes**. Journal of Sound and Vibration**, v. 189(5), p. 647-660, 1996b.

[110] XIE, W.-C. Vibration Mode Localization in Disordered Large Planar Lattice Trusses. **Chaos, Solitons & Fractals**, v. 8(3), p. 433-454, 1997.

[111] YONG, Y. and LIN, Y.K. Propagation of decaying waves in periodic and piecewise periodic structures of finite length, **Journal of Sound and Vibration**, v. 129(2), p. 99-118, 1989.

[112] YONG, Y. and LIN, Y.K. Dynamics of Complex Truss-Type Structures, **American Institute of Aeronautics Astronautics Journal**, v. 28(7), p.1250-1258, 1990.

This page intentionally left blank

PÓS-GRADUAÇÃO
ENGENHARIA MECÂNICA | UFU

Universidade Federal de Uberlândia - UFU
2121, avenida João Naves de Ávila
38400 Uberlândia, MG - Brésil

Titre : Bandgaps robustes pour contrôle de vibration dans les structures périodiques

Mots clés : Structures Périodiques, Contrôle de vibration, Analyse Probabiliste, Propagation d'incertitudes, Phénomène de Localization, Propagation des Ondes

Résumé : Dans cette thèse, une méthodologie simple pour trouver des bandes interdites robustes est présentée. Quatre structures différentes sont utilisées comme exemples numériques pour des modèles infinis et finis. Les deux premières possèdent des zones d'atténuation créées pour les ondes longitudinales en utilisant des cellules unitaires de masses/ressorts et de barres. La méthode des Matrices de Transfert est utilisée pour modéliser la cellule unitaire. Avec cette méthode, il est possible d'obtenir les réponses en fréquence, en utilisant une méthode spectrale, et les constantes de dispersion, en résolvant un problème aux valeurs propres. Les paramètres physiques et géométriques les plus influents sont déterminés en effectuant une analyse de sensibilité aux dérivées partielles et aux différences finies à travers un modèle infini. Dans ce cas, pour le deuxième exemple, la section de la demi-cellule est considérée comme une variable stochastique, représentée par une fonction densité de probabilité pour une analyse probabiliste. Le troisième exemple concerne les bandes interdites pour les ondes de flexion utilisant des cellules unitaires de poutres. Dans ce cas, la méthode classique des Matrices de Transfert ne peut pas être utilisée pour obtenir une réponse de structure finie en basses fréquences en raison de la présence de matrices mal conditionnées. Par conséquent, une méthode récursive est utilisée. Une analyse expérimentale est également réalisée pour ce cas, mais considérant la longueur de la moitié des cellules unitaire comme incertaine.

Le dernier exemple est un treillis périodique considéré avec et sans dispositifs intelligents. La cellule unitaire de cette structure en treillis peut présenter des éléments passifs et actifs. En raison de la complexité de ce type de cellule, la méthode des éléments finis est utilisée. Cependant, ce type de structure ne présente pas de ruptures d'impédance suffisamment fortes pour ouvrir des bandes interdites même en présence de sous-structures répétitives. En vertu de cela, huit scénarios sont étudiés en considérant l'introduction de masses concentrées dans les articulations, et les actionneurs piézoélectriques dans les circuits shunt résonants qui sont considérés comme stochastiques pour des cas spécifiques. Pour chaque modèle de structure, une simulation de Monte Carlo avec Latin Hypercube est effectuée, les distinctions entre les zones d'atténuation incertaines correspondantes pour les modèles finis et infinis sont exposées et la relation avec les modes localisés est clarifiée. Ces résultats suggèrent que les modèles finis ont une bande interdite plus large que les modèles infinis en considérant les incertitudes. En d'autres termes, les incertitudes entre les cellules voisines se compensent et les structures finies sont naturellement plus robustes. Enfin, l'effet de l'augmentation du niveau d'incertitude, en faisant varier un coefficient stochastique, est analysé et le concept de bande interdite robuste est présenté.

Title : Robust bandgaps for vibration control in periodic structures

Keywords : Periodic Structures, Vibration Control, Probabilistic Analysis, Uncertainty Propagation, Localization Phenomena, Wave Propagation

Abstract : In this thesis, a simple methodology to find robust bandgaps is presented. Four different periodic structures are used as numerical examples for infinite and finite models. The first two are related to attenuation zones created for longitudinal waves using spring-mass and stepped rod unit cells. The Transfer Matrix method is used to model the unit cell. With this method, it is possible to obtain the frequency responses, using a spectral method, and dispersion constants, solving an eigenvalue problem. The most influential physical and geometrical parameters are determined by performing partial derivative and finite difference sensitivity analysis through an infinite model. Therein, for the second example, the cross-section area of half-cell is considered as a stochastic variable represented by a probability density function with specific deviation properties for a probabilistic analysis. The third example concerns the bandgaps for flexural waves using stepped beams unit cells. For this case, the classical Transfer Matrix method cannot be used to obtain finite structures response in low frequency because of the presence of ill-conditioned matrices. Therefore, a recursive method termed Translation Matrix, which avoid matrix multiplication, is used and the corresponding probabilistic analysis is performed using the half-cell thickness as a random variable. An experimental analysis is also performed for this case, but considering half-cell length as uncertain.

The last example is a periodic truss that is considered with and without smart components. The unit cell of this lattice structure can present passive and active members. As long as the type of unit cell is more complex, the finite element method is used. However, this kind of structure does not have impedance mismatches strong enough to open bandgaps although the presence of repetitive substructures. In virtue of this, eight scenarios are investigated considering the introduction of concentrated mass on joints and piezoelectric actuators in resonant shunt circuit which are considered as stochastic for specific cases. For each structure model, a Monte Carlo Simulation with Latin Hypercube sampling is carried out, the distinctions between the corresponding uncertain attenuation zones for finite and infinite models are exposed and the relation with localized modes is clarified. These results lead to conclude that the finite models present a larger stop zone considering stochastic parameters than infinite models. In other words, the uncertainties between neighbors' cells compensate each other and the finite structures is naturally more robust. Finally, the effect of increasing the uncertainty level, by varying a stochastic coefficient, is analyzed and the concept of robust band gap is presented.

SPIM

Université Bourgogne Franche-Comté
32, avenue de l'Observatoire
25000 Besançon, France

UBFC
UNIVERSITÉ
BOURGOGNE FRANCHE-COMTÉ

SPIM

■ École doctorale SPIM 1 rue Claude Goudimel F - 25030 Besançon cedex

■ tél. +33 (0)3 81 66 66 02 ■ **ed-spim@univ-fcomte.fr** ■ www.ed-spim.univ-fcomte.fr

UFC
UNIVERSITÉ
DE FRANCHE-COMTÉ